UNIVERSITY OF CALIFORNIA, SAN DIEGO

Effects of Asynchrony and Anatomic Structure on Left Ventricular Mechanics

A dissertation submitted in partial satisfaction of the
requirements for the degree Doctor of Philosophy

in

Bioengineering

by

Benjamin Anthony Coppola

Committee in charge:

Jeffrey Omens, Chair
Andrew McCulloch, Co-Chair
James Covell
Larry Mulligan
Sanjiv Narayan
Geert Schmid-Schönbein

2008

The dissertation of Benjamin Anthony Coppola is approved, and it is acceptable in quality and form for publication on microfilm:

_____

_____

_____

_____

_____
Co-Chair

_____
Chair

University of California, San Diego

2008

To Mom and Dad

Table of Contents

LIST OF FIGURES

LIST OF TABLES

ACKNOWLEDGEMENTS

This dissertation is the result of five years of research in the Cardiac Mechanics Research Group in the Department of Bioengineering at the University of California, San Diego under supervision of Dr. Jeffrey H. Omens. I would like to first of all thank my advisors. Dr. Omens, for his realistic perspective, day-to-day help and his invaluable experience with many experimental methods. Dr. McCulloch, for all his insight from both biological and engineering perspectives, and for the unique ability to see things in ways I hadn't considered. Dr. Narayan, for his clinical perspective and for giving me the opportunity to get clinical exposure. Dr. Schmid-Schönbein, for giving me the opportunity to learn some laboratory skills before starting graduate school classes. Dr. Mulligan, for discussions about potential career opportunities in industry. And, last but not least, Dr. Covell, whose excitement in my work gave me the motivation to persevere whenever I encountered a dead end, and to put things in context of the bigger picture.

A special thanks to everyone who helped with the animal surgeries, and especially: Drs. Covell and Omens, Katrina Go, Aundrea Graves, Rachel Alexander, Jay Yee and Leonard Lee. Great thanks also to Dr. Andrew McCulloch, Dr. Roy Kerchoffs, and Fred Lionetti, without whom the computational section of my dissertation would not be possible.

I would also like to thank all of my friends, many of whom are current or previous graduate students at UCSD, and especially those in the Cardiac Mechanics Research Group. They have been my colleagues as well as my friends. They have been my support group, and have provided me with an outlet during the stressful times.

And most importantly of all, thanks goes out to my loved ones. To mom and dad, for giving me the opportunity to be here in the first place, and supporting me through all of my choices in life. And to Aundrea, for many things, but most of all for putting up with me through the completion of this dissertation.

Chapter 3, in full, is a reprint of the material as it appears in "Asynchrony of Ventricular Activation Affects Magnitude and Timing of Fiber Stretch in Late-Activated Regions of the Canine Heart" by Benjamin A. Coppola, Andrew D. McCulloch, James W. Covell, and Jeffrey H. Omens in the *American Journal of Physiology: Heart and Circulatory Physiology* 293: H754-H761, 2007. The dissertation author was the primary investigator and author of this paper.

Chapter 4, in part, has been accepted for publication as "Role of Myocardial Sheets in Ventricular Wall Mechanics" by Benjamin A. Coppola and Jeffrey H. Omens in *Molecular and Cellular Biomechanics*, 5.3: 183-196, 2008. The dissertation author was the primary investigator and author of this paper.

VITA

2003	Bachelor of Science, Lehigh University
2004-2006	Teaching Assistant, Department of Bioengineering, University of California, San Diego
2006	Master of Science, University of California, San Diego
2008	Doctor of Philosophy, University of California, San Diego

PUBLICATIONS

Manuscripts:

Ashikaga H, Coppola BA, Yamazaki KG, Villarreal FJ, Omens JH, Covell JW. Changes in myocardial tissue volume during the cardiac cycle: implications for transmural blood flow and cardiac structure. *Am J Physiol Heart Circ Physiol* 295.2: H610-8, 2008.

Coppola BA and Omens JH. Role of tissue structure on ventricular wall mechanics. *Molecular and Cellular Biomechanics* 5.3, 183-196, 2008.

Coppola BA, Covell JW, McCulloch AD, and Omens JH. Asynchrony of ventricular activation affects magnitude and timing of fiber stretch in late-activated regions of the canine heart. *Am J Physiol Heart Circ Physiol.* 293.1: H754-61, 2007.

Ashikaga H, Coppola BA, Hopenfeld B, Leifer ES, McVeigh ER, and Omens JH. Transmural Dispersion of Myofiber Mechanics: Implications for Electrical Heterogeneity In Vivo. *Journal of the American College of Cardiology* 49: 909-916, 2007.

Abstracts:

Coppola BA, McCulloch AD, Covell JW, Omens JH. Relationship between ventricular wall function and underlying structure, location, external loading and activation sequence. (Abstract). *FASEB Journal* 970.13, 2008.

Ashikaga H, Coppola BA, Yamazaki KG, Villarreal FJ, Omens JH, Covell JW. Transmural Changes in Myocardial Tissue Volume During the Cardiac Cycle: Implications for Microvascular Flow Patterns with Ventricular Pacing. (Abstract). *FASEB Journal* 970.38, 2008.

Ashikaga H, Coppola BA, Hopenfeld B, McVeigh ER, and Omens JH. YI1-2: Transmural dispersion of myofiber mechanics: Implications for electrical heterogeneity in vivo. (Abstract) *Heart Rhythm* 2006(3): S106, 2006.

Ashikaga H, Coppola BA, Hopenfeld B, R. McVeigh E, and Omens JH. Mechanical insights into transmural dispersion of electrical sequence. (Abstract) *Journal of Electrocardiology Research and Technology Transfer in Computerized Electrocardiology, Proceedings of the 31st Annual ISCE Conference* 39: S31, 2006.

Coppola BA, Covell JW, Omens JH: Magnitude of prestretch during ventricular activation is proportional to the amount of late activated tissue in the canine heart. (Abstract). *FASEB Journal* 746.15, 2006.

Coppola BA, Covell JW, Omens JH: Changes in cardiac action potential do not correlate with the onset of fiber relaxation. (Abstract). *FASEB Journal* 709.15, 2005.

ABSTRACT OF THE DISSERTATION

Effects of Asynchrony and Anatomic Structure on Left Ventricular Mechanics

by

Benjamin Anthony Coppola

Doctor of Philosophy in Bioengineering

University of California, San Diego, 2008

Professor Jeffrey Omens, Chair
Professor Andrew McCulloch, Co-Chair

It is now recognized that regional estimates of myocardial function are necessary to understand the underlying basis of global cardiac function. Moreover, these regional measures are more meaningful when expressed in terms of the muscle fiber architecture. In addition, myocardium has been shown to be a syncytium of myofibers organized into branching laminar “sheets”, and recent evidence suggests that the sheet structure is important to systolic wall thickening. Therefore, we studied the regional mechanics of

both the normal heart and a model of dyssynchronous activation, and related each to the local fiber and sheet structure.

Regional deformation was assessed by implanting beads into the canine heart and imaging them with biplane cineradiography. After the functional data was acquired, fiber and sheet orientations were determined by histological sectioning. In the model of the dyssynchronous heart, myofibers in the late-activated region continued to stretch 44 ms after local tissue activation, and was associated with little stretching perpendicular to the fibers or shearing. Despite occurring primarily during isovolumic systole, this deformation differed markedly from what has been observed during passive inflation, reflecting the state of partial activation. In addition, this dyskinetic contraction did not alter the motion of myocardial sheets relative to wall motion. The relative contributions of sheet lengthening and shearing represented most of the overall wall thickening, and no acute interventions changed this relationship. Therefore, the structural architecture of the ventricular wall appears to be the dominant factor for its regional mechanical function. Using detailed histological measurements of the myocardial sheets, we attempted to derive a mathematical model coupling myofiber tension to active stress transmission through the myocardium. When simulating ventricular mechanics with a finite element model, it appears that a stress component transverse to the myofibers is necessary to replicate experimental measurements. However, the direction of transverse stress transmission is not bounded by the sheet orientation (i.e. only within sheets), so the mechanistic role of the sheets on active contraction remains unclear.

1. General Introduction

The heart is the driving force which pumps blood throughout the body, perfusing all of the body's organs and sustaining life. Implicit in the ability of the heart to act as a circulatory pump is it's ability to contract and generate pressure. This is especially important in the left ventricle, which consists of 70-80% of the total mammalian heart mass and shoulders the largest load: perfusion of the systemic circulation. Therefore, the mechanics of the left ventricle are critical to a properly functioning heart.

The heart undergoes a complex deformation in order to eject blood with high mechanical efficiency, that is, near complete ejection in each cardiac cycle. Researchers have described many changes in the diseased heart, particularly the failing heart. These pathophysiologic mechanisms fall into the general categories of 1) cardiac abnormalities (structural and functional) and 2) biologically active agents in both the myocardial tissue and the circulation. For a complete list of currently known factors, see Jessup and Brozena (41). Those in the former group have a direct effect on myocardial deformation, such as dyssynchrony, hypertrophy, loss of viable muscle, and fibrosis. Those in the latter group act both directly on the heart (e.g. production of brain natriuretic peptide), and indirectly by affecting the peripheral resistance encountered by the heart (e.g. upregulation of the renin-angiotensin-aldosterone and sympathetic nervous systems). This dissertation focuses on the effects of cardiac abnormalities, and in particular, describes the roles of synchrony and anatomic structure in the functioning of the normal heart in comparison to the diseased heart.

A basic scientific and physiologic understanding of mechanical synchrony and the role of myocardial anatomy may prove vital for the proper treatment of, or prevention of, heart failure. The increasingly frequent use of cardiac resynchronization therapy for the treatment of heart failure and dyssynchrony, accompanied by an approximately 30% nonresponder rate (1, 8), underscores this need.

1.1. Statistics And Rationale

According to the American Heart Association, cardiovascular disease affects over 80 million people in the United States, at an estimated annual cost of $448.5 billion (2). Cardiovascular disease encompasses a number of different conditions, with coronary artery disease and hypertension being the largest contributors. A subset of this population has heart failure (5.3M Americans, annual cost $34.8B), a syndrome characterized primarily by inadequate pumping function. These patients typically have an increased end diastolic volume and reduced stroke volume, resulting in a reduction in ejection fraction (=stroke volume/end diastolic volume). In a normal patient, ejection fraction has been found to be approximately 65% (54). In a patient with heart failure, ejection fraction is typically reduced below 50% (97). However, patients with severe heart failure can have ejection fractions below 20% or can retain normal ejection fractions. Despite this, the common link between these patients is the inability of the heart's output to keep up with the body's demands. As a result, these patients suffer from decreased quality of life. For instance, they may have difficulty walking up a flight of stairs or may even be bedridden.

There are a number of therapies that have proven to be successful for treating heart failure, including administration of beta-blockers (18) to decrease sympathetic nervous activity; angiotensin-converting enzyme (ACE) inhibitors (30), angiotensin-receptor blockers (ARBs) (22), or spironolactone (68) to reduce the effects of the renin-angiotensin-aldosterone system; diuretics such as furosemide (25) to reduce congestion. All of these therapies have an indirect action on the heart, acting primarily by changing the loading conditions and peripheral resistance. Direct cardiac interventions have been attempted as well, such as ventricular reduction surgery (4), passive ventricular constraints (89), and ventricular reshaping devices (46, 79). Unfortunately, these approaches have led to mixed results and they are not ideal options because they require invasive surgeries in high-risk patients.

A large subset of heart failure patients suffer from dyssynchrony (47), including 1/3 of patients with a narrow QRS complex (12). For this subset of patients, a less invasive treatment with a direct mode of action is available, termed cardiac resynchronization therapy (CRT). This involves pacing both ventricles of the heart to restore electrical synchrony, and, in responder patients (~70%), results in increased contraction synchrony and improved ejection fraction. The 30% nonresponder rate associated with CRT suggests there may be room for improvement with better understanding of dyssynchrony. Moreover, there may be other direct cardiac targets to treat heart failure that have yet to be discovered. A more thorough understanding of the roles of dyssynchrony and anatomic structure on cardiac deformation should provide further insight on this topic.

1.2. Relationship Between Global Function and Regional Mechanics

The ventricles of the heart undergo contract to eject blood to the lungs and body. Ideally, this contraction is synchronous and powerful, the result of many muscle fibers shortening and generating force synergistically. Furthermore, the relaxation of the heart should be rapid, with muscle fibers returning to their original length quickly following the ejection period. This allows for maximum diastolic filling time.

The reality of myocardial contraction is quite a bit more complicated, even in the healthy heart (13). The left ventricle (LV) is asymmetric, with an approximately ellipsoidal, thick-walled shape (77). Its wall thickness varies, decreasing from the base to the apex of the heart (90). Two papillary muscles tether the mitral valve to the LV wall. Electrical activation is somewhat heterogeneous (26), and the LV has an outflow tract which channels flow toward the aorta as the ventricle undergoes a counter-clockwise twisting motion (viewed from the apex). The end result of all these complicating factors is that the deformation of the heart is complex and varies regionally and transmurally (i.e. across the wall). Nonetheless, this deformation field exists and it can be quantified and used to interpret how the normal heart functions.

Likewise, the diseased heart, which has reduced global output, can be analyzed in terms of its regional and transmural patterns of deformation. For example, a myocardial infarction causes tissue necrosis and scar formation, eliminating the shortening in that local region. However, the heart remains able to pump blood, despite three distinct regions of mechanical function: the infarcted region, the border zone, and the remote (healthy) region. This is elegantly described in the review by Holmes et al. (37). None

of these three regions behaves exactly like it did in the non-ischemic heart. This example highlights the link between regional and global function.

Besides ischemia, other important factors influencing the deformation pattern of the heart include: 1) the transmural sequence of electrical activation/repolarization, 2) regional heterogeneity of electrical activation, and 3) regional differences in anatomic structure. These factors will be discussed in the following sections.

Role of Depolarization/Repolarization Sequence

The ventricles of the normal heart are rapidly activated by the Purkinje fibers, a special cell type of the cardiac conduction system. These Purkinje fibers are spread throughout the ventricular endocardium (74), with additional morphological features varying across species (65, 93). As the Purkinje fibers activate the regular cardiac muscle cells, the depolarization (activation) wave continues and the cells are eventually all activated. This intramuscular propagation occurs at a slower rate than in the Purkinje fibers. Because the mechanical activity of a cell is linked to its electrical activation through a process known as excitation-contraction coupling (11), this order of cell depolarization and repolarization affects mechanical function.

Normal Transmural Gradients of Electrical activity

Because the Purkinje fibers are distributed throughout the endocardium, the depolarization wave normally spreads from the endocardium to the epicardium. This is the normal transmural gradient of electrical activation. Once activated, the cells undergo an action potential, whereby they remain depolarized for a period of time before repolarizing. The duration of this action potential is longer on the endocardium than on

the epicardium (3). As a result of this action potential heterogeneity, the sequence of repolarization is typically more synchronous than the sequence of depolarization. In other words, the epicardial cells are depolarized later, but have a shorter action potential.

Cordeiro et al. (23) showed that differences in cellular properties at different wall depths serve to convert the endocardial to epicardial activation sequence into a synchronous attraction. This appears to be achieved by a difference in electromechanical delay, i.e. delay from electrical activation to the onset of shortening. Although endocardial cells are electrically activated prior to epicardial cells, they have a longer electromechanical delay before shortening.

Pharmacological approaches to alter Repolarization Gradient

The action potential duration (APD) of a myocardial cell can be altered in many ways. The body has some natural mechanisms for this; for instance, an increase in heart rate will reduce the action potential duration. As a result, many pharmaceuticals also affect the action potential duration. This is typically an unwanted side effect of the drug that precludes further development, due to its arrhythmogenic potential. Interestingly, there are drugs which have been shown to have heterogeneous transmural effects on APD in isolated tissue, such as flecainide and propranolol (48). If these drugs have similar effects in the intact heart, they could be used to change the transmural repolarization sequence. This would likely have an important mechanical effect, by altering the sequence of myofiber relengthening. Such an intervention would improve understanding of the significance of the normal transmural gradient.

Ventricular Epicardial Pacing Alters Transmural Activation Gradient

While a pharmacological approach might be used to gain understanding of ventricular repolarization, a pacing approach might be used to gain understanding of the depolarization sequence. As stated above, the depolarization wavefront normally travels from endocardium to epicardium. By pacing from a point on the left ventricular epicardium, this sequence would be reversed in that local region. Due to the complexities of cardiac electrophysiology, however, this reversal of transmural activation would not be realized across the entire left ventricle (unless the entire epicardium were simultaneously paced). Therefore, only the area immediately surrounding the pacing site would be appropriate for analysis of the significance of normal transmural activation on myocardial mechanics.

Role of Dyssynchrony

Dyssynchrony, also known as asynchrony, refers to the inability of different segments of the heart to contract simultaneously. This may occur in multiple ways, the most common examples being structural abnormalities and myocardial infarction. Structural abnormalities often lead to electrical conduction defects, which indirectly create mechanical dyssynchrony by creating an electrically dyssynchronous activation pattern. Left bundle branch block is the most common of these abnormalities, affecting 30% to 50% of patients with advanced HF (50). Alternatively, myocardial infarction can cause cell death which results in the formation of a non-contractile scar (95). When the surrounding healthy myocardium contracts, the infarcted tissue stretches and energy is wasted. Currently, it remains unknown whether ventricular dyssynchrony is fundamental

to the pathogenesis of dysfunctional hearts. Experimental studies have demonstrated regional molecular changes in discoordinately contracting myocardium, a finding that is consistent with the idea that dyssynchrony contributes to disease pathophysiology(87)

To study dyssynchrony in an animal model, a choice must be made to focus on ischemic or non-ischemic etiologies, as the resulting pathophysiologies may differ. To reproduce the ischemic etiology, an infarct could be created or stunning induced (58). For the non-ischemic etiology, RF ablation of a bundle branch or ventricular pacing may be used (35, 72). For the purposes of this dissertation, only the type of dyssynchrony induced by altered electrical activation (non-ischemic) will be considered.

Ventricular Pacing as a Model of Dyssynchrony

Structural abnormalities can disrupt the normal sequence of activation and greatly increase ventricular activation times. For example, in patients with left bundle branch block, the right ventricle is activated by the fast-conducting Purkinje network but the left ventricle is not. A depolarization wavefront then progresses from the right ventricle to the left ventricle through slower, intramuscular conduction. The net result is high activation times (>120 ms) in the left ventricle, particularly in the posterior basal and lateral basal epicardial regions (107).

Dyssynchrony can be created in a healthy animal by radio-frequency (RF) ablation of the left bundle branch, recreating the human etiology (49). This can be technically challenging and has the disadvantage of being irreversible. Alternatively, atrio-ventricular sequential pacing can be used, in an approach which is reversible and simulates the type of dyssynchrony witnessed in non-ischemic heart failure associated

with structural abnormalities such as left bundle branch block. In this approach, bipolar electrodes are placed on the right atrium and the left ventricular epicardium. The atrium is paced first, then after a short delay, the ventricle is paced. This short delay ensures that the ventricular pre-excitation leads to complete depolarization of the ventricles that is independent of any native conduction through the atrio-ventricular (AV) node (28). The ventricular pacing approach, although not directly resembling the human condition, has it's advantages. Synchrony can be restored (by turning off the pacemaker) and the initial site of activation can be relocated to different regions of the heart.

Regional Mechanics of the Dyssynchronous Heart

The characteristic deformation pattern of the dyssynchronously contracting heart has been described in patients (62, 69) as well as animals (10, 49, 70). In the early-activated region, the tissue initially shortens rapidly, followed by a period of bulging, or relengthening, late in systole (10). In some cases, the relengthening is followed by another period of shortening (72, 105). In the late-activated region, there is a period of early stretch ("prestretch") followed by an augmented contraction that exhibits post-systolic shortening (shortening that extends beyond the ejection phase into diastole) (15).

The majority of these studies to date have relied on echocardiography, MRI, and ultrasonic crystals to observe the segmental deformation patterns. Therefore, little information is available about how the deformation varies transmurally or how it relates to the fiber anatomy. These limitations will be discussed in greater detail in Section 1.3.

Chronic Remodeling

Animal models have shown that concomitant with the dyskinetic contraction pattern is a related pattern of hypertrophy (71, 96). The early-activated sites undergo wall thinning while the late-activated sites hypertrophy. Furthermore, there is evidence that dyskinesis spatially polarizes ventricular protein expression, generating transmural and transventricular gradients in phosphorylated erk mitogen-activated protein kinase, sarcoplasmic reticulum Ca^{2+}-ATPase (SERCA2a), phospholamban, and connexin43 levels (87). This remodeling extends to electrophysiologic properties, mediated by a rearrangement of connexin43 at the subcellular level (86).

Cardiac Resynchronization Therapy

Cardiac Resynchronization Therapy (CRT) is used clinically for the treatment of cardiac dyssynchrony in heart failure patients. In brief, CRT is defined as the stimulation of the left ventricle or simultaneous stimulation of both the right and left ventricles after atrially sensed or paced events (27). Like a standard pacemaker, a CRT device typically consists of leads in the right atrium and right ventricle to control sensing and pacing of the heart. In addition, CRT devices have a third lead placed in the left ventricle. An epicardial coronary vein is used for this because it can be accessed by catheterization of the coronary sinus, and thus does not require an invasive thoracotomy. This LV lead serves to correct, in whole or in part, atrioventricular, interventricular, and intraventricular dyssynchronies, by pre-exciting a region of the heart which would otherwise be late-activated (27).

Large-scale, randomized clinical trials have shown improvement in symptoms and longevity in patients with advanced heart failure and QRS prolongation (1, 17, 19, 21, 36, 78, 108). In addition to improving electrical synchrony, CRT has been shown to promote reverse LV remodeling and reduce mitral regurgitation, in addition to improvement in systolic and diastolic function (88). Unfortunately, it still suffers from a 30% nonresponder rate (1, 8), most likely due to inadequate patient identification. Hopefully, animal research in combination with future clinical trials will reduce this nonresponder percentage without excluding those patients who would benefit from the therapy.

Role of Myocardial Anatomy

Excitation of the ventricular muscle results in force directed along the myofiber axis. Therefore, the arrangement of myofibers throughout the heart affects the regional mechanics. Beyond myofibers, there is a secondary layer of organization known as the myocardial laminae, or sheets. There is evidence to suggest that this sheet organization also plays a role in the regional mechanics of the heart. The following sections describe the fiber and sheet orientation in the canine heart and the resulting effects on tissue mechanics.

Myofibers

The myofibers of the heart are oriented roughly in the epicardial tangent plane (small imbrication angle). Within this circumferential-longitudinal plane, fiber angle is defined as the angle from the positive circumferential direction. It is well known that the fiber angle varies transmurally in a linear or slightly sigmoidal fashion, as has been shown in canine (91), as well as other mammalian species (64, 81). This transmural

variation is exhibited through the heart, but the absolute values on the endocardium and the epicardium vary regionally (91).

Cardiomyopathy and Genetic Disease

The myofibers of the healthy heart are highly aligned at any given wall depth. Disruption of this pattern is the hallmark of familial hypertrophic cardiomyopathy, a genetic disease often leading to focal myofiber disarray (57, 102). Karlon et al. (44) utilized a genetically-modified mouse model expressing the human oncogene *ras* as a model of familial hypertrophic cardiomyopathy. They found that the dispersion of myofiber angle about the mean was significantly increased compared to the normal mouse heart (standard deviations of ~25º vs. 12º).

Effect of Myofiber Distribution on Regional Mechanics

The transmural arrangement of myofibers has been shown to have functional implications. For example, Boovendeerd et al. determined through a modeling approach that the distribution of systolic fiber stress and strain through the thickness of the wall is sensitive to the fiber angle distribution (14, 76). Moreover, the physiological transmural distribution results in transmural fiber stress and strain which are approximately homogeneous; this result has been shown experimentally for fiber strain in several species (7, 20) although a small but significant gradient has been observed in human (55).

The heart also exhibits significant torsion during contraction (5), of a left-handed sense (counter-clockwise as viewed from the apex). Taber et al. suggested this to be a result of the epicardial fiber angle; given equal force generation, the epicardial fibers will produce more torque because they have a longer moment arm than the inner layers (92).

With the aid of a model, they also found that this result was sensitive to the transmural distribution. An increase in fiber angle span (= epicardial fiber angle – endocardial fiber angle) from 120º to 180º was associated with a doubling of twist angle.

Myocardial torsion may also be affected by local disruptions to the fiber distribution. In a mechanical study of the *ras*-expressing mouse, myofiber disarray was found to affect the pattern of surface deformation in a heterogeneous way (normal vs. disarrayed regions). Specifically, surface shearing was found to be reduced in the disarrayed regions (45). This loss of shear suggests that disarray interferes with the heart's ability to twist.

Myocardial Laminar Sheets

Cardiac myofibers are part of a secondary level of structural organization of the myocardium. These secondary structures are referred to as myocardial laminae, or sheets (32). They were described by Spotnitz et al. (85), as "sliding planes" in a long axis section of the rat heart. The authors suggested that these sliding planes could provide a mechanism for the paradoxically large changes in wall thickness observed in the left ventricle (discussed further in the following section).

Legrice et al. showed that these sliding planes represented gaps between myocardial sheets, defined as tightly coupled layers 4-8 cells thick (51). Through electron microscopy, they showed that adjacent sheets are loosely connected via collagen struts. These loose connections are observed as gaps in gross histological sections. Interestingly, the orientations of these sheets varies regionally and transmurally (51). Furthermore, there is considerable variation of these sheets at the microstructural level.

This can be seen in images of sheets in sheep (34) and pigs (38), and has been observed by the author in canine tissue sections.

Wall Thickening Mechanics

Ventricular wall thickening is an important mechanism for systolic ejection. Radial strain, a measure of local wall thickening, can be as large as 0.4 in the inner wall (approximately 40% thickening) (100, 101). A simple model of an incompressible cell suggest that the maximum fiber shortening (15%) only increases cellular thickness by about 8%. Therefore, some mechanism for cellular rearrangement must exist.

The ability of these gaps to promote sliding of adjacent sheets, as suggested by Spotnitz et al. (85), was further reinforced by measured shear strains in the canine left ventricle (52). Costa et al. later related ventricular wall thickening to deformation of the sheets by a simple equation (24), finding sheet extension and shearing to be the primary contributors to wall thickening.

Implications for Heart Failure

There are structural changes associated with the failing heart. However, there is little evidence to support any change in the transmural distribution of fiber angle with any heart failure model. The sheet orientation, on the other hand, has been shown to undergo up to a 15º change in a dyssynchronous failing heart model (35) and 10º in the infarct border zone (110). While such changes are relatively small, they may be important. In addition, it is well known that there are substantial changes to the collagen structure of the failing heart (16, 75, 103). It is therefore very likely that these changes affect the

structure and connectivity of the myocardial laminar sheets. For example, this might inhibit the cellular rearrangement along the sliding planes.

Summary

Both dyssynchrony and anatomic structure play important roles in the pathophysiology of heart failure. Using a ventricular pacing model, the characteristic deformation pattern can be reproduced in order to better understand the mechanics of dyssynchrony and to relate those findings to ventricular pressure generation. In addition, histological measurement of myocardial sheets facilitates the expression of cardiac deformation with respect to this relevant anatomic structure. This may help elucidate the mechanism of paradoxical systolic wall thickening.

1.3. Techniques for Studying Intact Heart Mechanics

Many techniques have been used to study the deformation of the ventricles of the heart, and each has advantages and disadvantages. Several of the most commonly used techniques will be described, in brief, in the following sections. In order to perform an in-depth, mathematically rigorous analysis of deformation, there is one factor that each technique must have in common: material markers. These are markers that are fixed to one particular point in space within the heart, and thus can be used to track its motion. Based on the relative motions of several markers, the deformation can be calculated and expressed in terms of a spatially-varying quantity such as Lagrangian strain. This strain tensor fully describes the deformation from one configuration to another at any point in space. Non-marker based methods have been used to describe myocardial strain (66), but these techniques are indirect estimations of strain and will not be discussed here.

Ultrasound

Ultrasound refers to any use of sound waves with frequency greater than 20 kHz, and has wide-ranging uses in medicine. Most commonly, ultrasound is used to visualize the motion of a boundary between area of different densities. For example, a fetus can be visualized inside of the womb(42), or a heart can be visualized inside the chest in a process known as echocardiography(43, 67). However, because traditional ultrasound does not make use of material markers, it is unable to provide information about the deformation of the heart. Applications have been developed for ultrasound that circumvent this problem; these will be described in the following sections.

Intramyocardial crystals

In an alternative use of ultrasound, "crystal" pairs can be implanted into the wall of the ventricle. The crystals are made from a piezo-electric ceramic material. One of the crystals emits sound in the 5-10 MHz range and the either receives it. This allows for a real-time measurement of the distance between them. In addition to the invasiveness of the open-chest preparation necessary for implantation, the crystals themselves are large (at least 2mm diameters) and have wires attached to them. This can create a significant amount of damage to the myocardium upon implantation, as well as limiting how closely the emitter/receiver pair can be placed. Therefore, intramyocardial crystals are best for measuring changes in segment length along a single dimension (82). However, by using 3 or more emitter/receiver pairs, it is possible to measure 2D or 3D deformation(98). Additionally, crystals have two major advantages: high temporal resolution and real-time

viewing. Finally, arrays of crystals placed about the left ventricle can be used to estimate changes in cavity volume (56).

Speckle Tracking

Echocardiography is traditionally used to visualize the motions of the heart wall to determine the synchrony of contraction and the ejection fraction. It has been observed that the myocardium contains an acoustic signature, a unique speckling pattern (61, 63). These speckles remain fixed within the myocardium over time, providing material markers. Therefore, post-processing of traditional echocardiographic images can be used to determine 2D or 3D cardiac deformation (83). This technique is new, and still being validated against other more established methods. Like intramyocardial crystals, speckle tracking also has excellent temporal resolution. In addition, it has much better spatial resolution, with the ability to measure local deformation in multiple regions and at different transmural depths. It also has the advantage of being non-invasive.

X-Ray

X-rays are typically used to image dense materials such as bone. Soft tissues, such as myocardium, provide limited resistance to x-ray penetration. These dense markers block the x-rays, creating a material marker in the x-ray images. These markers could then be imaged with biplane cineradiography, and their three-dimensional coordinates reconstructed. Records of this method date back to at least the 1960's, when lead beads were used to track changes in left ventricular dimensions (104). Though invasive, this technique has also been applied to (transplanted) human hearts (40), to

determine shortening and twisting of the left ventricle. The technique was modified by Fenton et al. to measure local three-dimensional strains (29), then improved by Waldman et al. (101), and is still in use today (7, 20).

The major advantage of the x-ray technique is its ability to track remodeling in a chronic preparation (6, 110), because the markers remain fixed within the tissue over time. However, like crystals, the x-ray technique also requires an open-chest preparation and implantation into the heart. However, these markers are usually smaller (<1mm) and do not have attached wires. The temporal resolution is typically better than magnetic resonance imaging (MRI) based techniques, but equal to or worse than echocardiographic techniques. This technique is still considered the gold standard for myocardial deformation, particularly for describing transmural deformation in a small volume of the heart (~25mm^2).

Magnetic Resonance Imaging (MRI)

Similar to echocardiographic images, MRI images do not contain material points. However, a technique known as myocardial tagging has become popular, in which "taglines" are created by saturation of radio frequency energy (9, 60, 109). These taglines persist for a brief period, typically less than one cardiac cycle, before disappearing. The intersections of taglines provide material points which can be tracked through time. More recently, a harmonic phase (HARP) approach has been used to simplify post-processing (31). HARP is analogous to echocardiographic speckle tracking, except that the material point is tracked by the phase of the MR signal.

MRI is one of the best methods for overall assessment of myocardial strain. It can be used to determine deformation simultaneously over the entire heart non-invasively. High spatial and temporal resolution can be achieved, as part of a tradeoff with longer imaging times (because averaging is used). Despite the obvious advantages, there are several limitations as well. Perhaps the most important is the inability to put ferrous metals in the scanner due to the magnetization effect. Other foreign objects, such as catheters, electrodes, etc. can introduce artifacts into the image. Another limitation is the inability to acquire data for the duration of the cardiac cycle simultaneous, but this can be avoided by triggering the taglines at different times in the cycle (84). Transmural resolution is limited, as there are typically only 3 tag intersections across the wall (72, 106). However, the HARP technique improves this by utilizing more of the data. Lastly, MRI can not be used measure chronic remodeling.

Optical Imaging

Optical imaging of the myocardium has also been used to study deformation (45, 59, 73). These techniques utilize markers affixed to the epicardial surface, which are then imaged by one or two cameras. The markers themselves can be of different compositions; adhesive paper (73), suture (59), and titanium dioxide (45) have all been used. The use of one camera prevents the tracking of fully three-dimensional material points; in this case the projection of these points onto the plane of the camera is used instead. This is equivalent to making the assumption that the radius of curvature at the point of measurement approaches infinity (and thus curvature is negligible). Using two

cameras, three-dimensional points can be reconstructed as described for the biplane x-ray technique.

The major limitation with this technique is that the observed deformation is limited to the epicardium. The temporal resolution is camera limited, while the spatial resolution is limited by the marker size and camera resolution.

Summary

Several techniques have been developed for the study of cardiac mechanics over the last thirty years. Despite it's limitations, X-ray imaging of implanted markers remains the gold standard in the field. However, MR tagging and echocardiographic speckle tracking will likely become increasingly popular in the coming years due to their suitability for use in patients. This is becoming apparent as we further our understanding of dyssynchrony and develop techniques for diagnosing and correcting it.

1.4. Computational Modeling of Myocardial Laminae

Continuum models of ventricular wall mechanics solve the partial differential equations governing the conservation of mass, momentum, and energy subject to prescribed ventricular geometry and wall structure, myocardial material properties and hemodynamic boundary conditions. With these inputs, the models can compute the distributions of wall displacement, strain and stress as a function of time. These outputs can then be compared with experimentally measured strains, to see how well the models predict the observed phenomena.

Current models of ventricular wall mechanics include: a realistic three-dimensional thick-walled geometry and muscle fiber and sheet orientation throughout

both ventricular walls (99); nonlinear, anisotropic material properties with respect to local fiber and sheet axes (94); contractile models incorporating the kinetics of sarcomere length-dependent myofilament activation and crossbridge cycling that are consistent with isometric and isotonic sarcomere mechanics in isolated trabeculae (39); and active systolic stresses that are three-dimensional with components directed transverse to the muscle fiber axis consistent with biaxial test measurements in tonically activated myocardium (53).

These models are comprehensive and reproduce many of the observed deformation patterns. However, they do not yet accurately reproduce the strain tensor at all depths through the wall. The shear components and the radial strain are least well approximated (101). The net result is an underestimation of systolic wall thickening, which may be related to the simplified representation of the fiber and sheet anatomy, which utilize only the mean orientations.

Biaxial Stress Development

There is evidence that suggests that myofibers develop force not only along their axis, but also perpendicular to it (53). The mechanism for this might be at the subcellular level, at the tissue level, or through a combination of the two.

Sub-Cellular Level

On the most basic level, electrical excitation of a cardiac muscle cell sets off a trigger of events that lead to shortening. Because the myofilaments of the cells are arranged longitudinally, force develops along the axis of the cell. Assuming a cell is nearly incompressible, axial shortening is accompanied by radial stretch. The reality is a

bit more complex. Myofiber force is created by the attachment of crossbridges, followed by a power stroke, which advances the actin and myosin filaments past each other. Schoenberg has shown that, if the subfragment-2 portion of the myosin cross-bridge to actin does not lie parallel to the myofilament axes then when a muscle fiber contracts, there will be a radial component to the cross-bridge force (80). This would provide a sub-cellular mechanism for observed cross-fiber stress.

Tissue Level

In addition to sub-cellular mechanisms, the observed cross-fiber stress could also be generated at the tissue level. For instance, a dispersion of myofiber angles about the mean would have the effect of reducing the total axial force while introducing a radial-directed component of force. Alternatively, the laminar structure of the myocardium may affect the force transmission at the tissue level. This might lead to a triaxial stress state, with different force magnitudes 1) along the myofibers, 2) perpendicular to myofiber axis but within the sheet, 3) perpendicular to the myofiber but across the sheet.

Modeling Passive Stress

Computational models have traditionally used a transversely isotropic, hyperelastic constitutive equation (33). Recognizing the anisotropic nature of the laminar structure, Usyk et al. (94) used an anisotropic constitutive equation. Interestingly, they found that simulations of systole were insensitive to changes to the within-sheet and across-sheet stiffness parameters.

Modeling Active Stress

In order to understand the effects of experimentally-measured biaxial force development (53), Usyk et al. also implemented a biaxial active stress law. In this model, there is assumed to be a sub-cellular mechanism for force generation, as well as an effect due to myofiber dispersion (94). By simulating the experimental conditions, they were able to choose matching model parameters. They then showed improved agreement between the finite element model and experimental deformation , as compared to the previous uniaxial model.

Summary

Finite element models of cardiac mechanics are a valuable tool for testing our understanding of myocardial function. Computational models also provide the unique opportunity to perform numerical experiments which are not possible in the laboratory. In an acute animal experiment, it is clearly not possible to remove the sheet architecture or alter the sheet coupling properties. However, these quantities can be included as parameters in a computational model and perturbed to better understand their influence, for example, on ventricular wall thickening. This finite element model might then be used to make predictions about changes in anatomic structure which accompany genetic abnormalities or heart failure.

1.5. Conclusion

Dyssynchrony and changes in sheet structure are both thought to play important roles in the pathophysiology of heart failure. Through a combination of experimental and

computational approaches, we can further our understanding of these conditions using rigorous engineering analysis and potentially direct future clinical diagnosis and treatment. Ultimately, this information might be used to reduce the nonresponder rate of cardiac resynchronization therapy without excluding good candidates, as well as understanding the importance of the change in sheet architecture during heart failure.

1.6. References

1. **Abraham WT, Fisher WG, Smith AL, Delurgio DB, Leon AR, Loh E, Kocovic DZ, Packer M, Clavell AL, Hayes DL, Ellestad M, Trupp RJ, Underwood J, Pickering F, Truex C, McAtee P, Messenger J, and the MIRACLE Study Group.** Cardiac Resynchronization in Chronic Heart Failure. *N Engl J Med* 346: 1845-1853, 2002.

2. **American Heart Association.** *Heart Disease and Stroke Statistics - 2008 Update*. Dallas, TX: American Heart Association, 2008.

3. **Antzelevitch C, Sicouri S, Litovsky S, Lukas A, Krishnan S, Di Diego J, Gintant G, and Liu D.** Heterogeneity within the ventricular wall. Electrophysiology and pharmacology of epicardial, endocardial, and M cells. *Circulation Research* 69: 1427-1449, 1991.

4. **Artrip JH, Oz MC, and Burkhoff D.** Left ventricular volume reduction surgery for heart failure: A physiologic perspective. *J Thorac Cardiovasc Surg* 122: 775-782, 2001.

5. **Arts T, Meerbaum S, Reneman RS, and Corday E.** Torsion of the left ventricle during the ejection phase in the intact dog. *Cardiovasc Res* 18: 183-193, 1984.

6. **Ashikaga H, Omens JH, and Covell JW.** Time-dependent remodeling of transmural architecture underlying abnormal ventricular geometry in chronic volume overload heart failure. *Am J Physiol Heart Circ Physiol* 287: H1994-2002, 2004.

7. **Ashikaga H, Omens JH, Ingels NB, Jr., and Covell JW.** Transmural mechanics at left ventricular epicardial pacing site. *Am J Physiol Heart Circ Physiol* 286: H2401-2407, 2004.

8. **Auricchio A, Stellbrink C, Sack S, Block M, Vogt Ju, Bakker P, Huth C, Schondube F, Wolfhard U, and Bocker D.** Long-term clinical effect of hemodynamically optimized cardiac resynchronization therapy in patients with heart failure and ventricular conduction delay. *Journal of the American College of Cardiology* 39: 2026-2033, 2002.

9. **Axel L and Dougherty L.** MR imaging of motion with spatial modulation of magnetization. *Radiology* 171: 841-845, 1989.

10. **Badke FR, Boinay P, and Covell JW.** Effects of ventricular pacing on regional left ventricular performance in the dog. *Am J Physiol Heart Circ Physiol* 238: H858-867, 1980.

11. **Bers D.** *Excitation-Contraction Coupling and Cardiac Contractile Force*: Springer, 2001.

12. **Bleeker GB, Schalij MJ, Molhoek SG, Holman ER, Verwey HF, Steendijk P, van der Wall EE, and Bax JJ.** Frequency of left ventricular dyssynchrony in patients with heart failure and a narrow QRS complex. *The American Journal of Cardiology* 95: 140-142, 2005.

13. **Bogaert J and Rademakers FE.** Regional nonuniformity of normal adult human left ventricle. *Am J Physiol Heart Circ Physiol* 280: H610-620, 2001.

14. **Bovendeerd PHM, Arts T, Huyghe JM, van Campen DH, and Reneman RS.** Dependence of local left ventricular wall mechanics on myocardial fiber orientation: A model study. *Journal of Biomechanics* 25: 1129-1140, 1992.

15. **Breithardt O-A, Stellbrink C, Herbots L, Claus P, Sinha AM, Bijnens B, Hanrath P, and Sutherland GR.** Cardiac resynchronization therapy can reverse abnormal myocardial strain distribution in patients with heart failure and left bundle branch block. *J Am Coll Cardiol* 42: 486-494, 2003.

16. **Brilla C, Rupp H, Funck R, and Maisch B.** The renin-angiotensin-aldosterone system and myocardial collagen matrix remodelling in congestive heart failure. *Eur Heart J* 16: 107-109, 1995.

17. **Bristow MR, Saxon LA, Boehmer J, Krueger S, Kass DA, De Marco T, Carson P, DiCarlo L, DeMets D, White BG, DeVries DW, Feldman AM, and the Comparison of Medical Therapy P, and Defibrillation in Heart Failure (COMPANION) Investigators,.** Cardiac-Resynchronization Therapy with or without an Implantable Defibrillator in Advanced Chronic Heart Failure. *N Engl J Med* 350: 2140-2150, 2004.

18. **Brophy JM, Joseph L, and Rouleau JL.** {beta}-Blockers in Congestive Heart Failure: A Bayesian Meta-Analysis. *Ann Intern Med* 134: 550-560, 2001.

19. **Cazeau S, Leclercq C, Lavergne T, Walker S, Varma C, Linde C, Garrigue S, Kappenberger L, Haywood GA, Santini M, Bailleul C, Daubert J-C, and The Multisite Stimulation in Cardiomyopathies (MUSTIC) Study Investigators.** Effects of Multisite Biventricular Pacing in Patients with Heart Failure and Intraventricular Conduction Delay. *N Engl J Med* 344: 873-880, 2001.

20. **Cheng A, Langer F, Rodriguez F, Criscione JC, Daughters GT, Miller DC, and Ingels NB, Jr.** Transmural sheet strains in the lateral wall of the ovine left ventricle. *Am J Physiol Heart Circ Physiol* 289: H1234-1241, 2005.

21. **Cleland JGF, Daubert J-C, Erdmann E, Freemantle N, Gras D, Kappenberger L, Tavazzi L, and the Cardiac Resynchronization -- Heart**

Failure (CARE-HF) Study Investigators. The Effect of Cardiac Resynchronization on Morbidity and Mortality in Heart Failure. *N Engl J Med* 352: 1539-1549, 2005.

22. **Cohn JN, Tognoni G, and the Valsartan Heart Failure Trial Investigators.** A Randomized Trial of the Angiotensin-Receptor Blocker Valsartan in Chronic Heart Failure. *N Engl J Med* 345: 1667-1675, 2001.

23. **Cordeiro JM, Greene L, Heilmann C, Antzelevitch D, and Antzelevitch C.** Transmural heterogeneity of calcium activity and mechanical function in the canine left ventricle. *Am J Physiol Heart Circ Physiol* 286: H1471-1479, 2004.

24. **Costa KD, Takayama Y, McCulloch AD, and Covell JW.** Laminar fiber architecture and three-dimensional systolic mechanics in canine ventricular myocardium. *Am J Physiol* 276: H595-607, 1999.

25. **Dormans TPJ, van Meyel JJM, Gerlag PGG, Tan Y, Russel FGM, and Smits P.** Diuretic efficacy of high dose furosemide in severe heart failure: Bolus injection versus continuous infusion. *Journal of the American College of Cardiology* 28: 376-382, 1996.

26. **Durrer D, van Dam RT, Freud GE, Janse MJ, Meijler FL, and Arzbaecher RC.** Total Excitation of the Isolated Human Heart. *Circulation* 41: 899-912, 1970.

27. **Ellenbogen K, Wilkoff B, Kay G, and Lau C.** *Clinical Cardiac Pacing, Defibrillation, and Resynchronization Therapy*: Saunders, 2007.

28. **Faris OP, Evans FJ, Dick AJ, Raman VK, Ennis DB, Kass DA, and McVeigh ER.** Endocardial versus epicardial electrical synchrony during LV free-wall pacing. *Am J Physiol Heart Circ Physiol* 285: H1864-1870, 2003.

29. **Fenton T, Cherry J, and Klassen G.** Transmural myocardial deformation in the canine left ventricular wall. *American Journal of Physiology- Heart and Circulatory Physiology* 235: 523-530, 1978.

30. **Garg R and Yusuf S.** Overview of randomized trials of angiotensin-converting enzyme inhibitors on mortality and morbidity in patients with heart failure. Collaborative Group on ACE Inhibitor Trials. *JAMA* 273: 1450-1456, 1995.

31. **Garot J, Bluemke DA, Osman NF, Rochitte CE, McVeigh ER, Zerhouni EA, Prince JL, and Lima JAC.** Fast Determination of Regional Myocardial Strain Fields From Tagged Cardiac Images Using Harmonic Phase MRI. *Circulation* 101: 981-988, 2000.

32. **Gilbert SH, Benson AP, Li P, and Holden AV.** Regional localisation of left ventricular sheet structure: integration with current models of cardiac fibre, sheet

and band structure. *European Journal of Cardio-Thoracic Surgery* 32: 231-249, 2007.

33. **Guccione JM, McCulloch AD, and Waldman LK.** Passive material properties of intact ventricular myocardium determined from a cylindrical model. *J Biomech Eng* 113: 42-55, 1991.

34. **Harrington KB, Rodriguez F, Cheng A, Langer F, Ashikaga H, Daughters GT, Criscione JC, Ingels NB, and Miller DC.** Direct measurement of transmural laminar architecture in the anterolateral wall of the ovine left ventricle: new implications for wall thickening mechanics. *Am J Physiol Heart Circ Physiol* 288: H1324-1330, 2005.

35. **Helm PA, Younes L, Beg MF, Ennis DB, Leclercq C, Faris OP, McVeigh E, Kass D, Miller MI, and Winslow RL.** Evidence of structural remodeling in the dyssynchronous failing heart. *Circ Res* 98: 125-132, 2006.

36. **Higgins S, Hummel J, Niazi I, Giudici M, Worley S, Saxon L, Boehmer J, Higginbotham M, De Marco T, and Foster E.** Cardiac resynchronization therapy for the treatment of heart failure in patients with intraventricular conduction delay and malignant ventricular tachyarrhythmias. In: *Journal of the American College of Cardiology*: Am Coll Cardio Found, 2003, p. 1454-1459.

37. **Holmes JW, Borg TK, and Covell JW.** Structure and Mechanics Of Healing Myocardial Infarcts. *Annual Review of Biomedical Engineering* 7: 223-253, 2005.

38. **Hooks DA, Trew ML, Caldwell BJ, Sands GB, LeGrice IJ, and Smaill BH.** Laminar Arrangement of Ventricular Myocytes Influences Electrical Behavior of the Heart. *Circ Res* 101: e103-112, 2007.

39. **Hunter PJ, McCulloch AD, and ter Keurs HE.** Modelling the mechanical properties of cardiac muscle. *Prog Biophys Mol Biol* 69: 289-331, 1998.

40. **Ingels N, Daughters G, Stinson E, and Alderman E.** Measurement of midwall myocardial dynamics in intact man by radiography of surgically implanted markers. *Circulation* 52: 859-867, 1975.

41. **Jessup M and Brozena S.** Heart Failure. *N Engl J Med* 348: 2007-2018, 2003.

42. **Ji E, Pretorius D, Newton R, Uyan K, Hull A, Hollenbach K, and Nelson T.** Effects of ultrasound on maternal-fetal bonding: a comparison of two- and three-dimensional imaging. *Ultrasound in Obstetrics and Gynecology* 25: 473-477, 2005.

43. **Kapetanakis S, Kearney MT, Siva A, Gall N, Cooklin M, and Monaghan MJ.** Real-Time Three-Dimensional Echocardiography: A Novel Technique to

Quantify Global Left Ventricular Mechanical Dyssynchrony. *Circulation* 112: 992-1000, 2005.

44. **Karlon W, Covell J, McCulloch A, Hunter J, and Omens J.** Automated Measurement of Myofiber Disarray in Transgenic Mice With Ventricular Expression of ras. *The Anatomical Record* 252: 612-625, 1998.

45. **Karlon WJ, McCulloch AD, Covell JW, Hunter JJ, and Omens JH.** Regional dysfunction correlates with myofiber disarray in transgenic mice with ventricular expression of ras. *Am J Physiol Heart Circ Physiol* 278: H898-906, 2000.

46. **Kashem A, Hassan S, Crabbe DL, Melvin DB, and Santamore WP.** Left ventricular reshaping: Effects on the pressure-volume relationship. *Journal of Thoracic and Cardiovascular Surgery* 125: 391-399, 2003.

47. **Kass DA.** An Epidemic of Dyssynchrony: But What Does It Mean? *Journal of the American College of Cardiology* 51: 12-17.

48. **Krishnan S and Antzelevitch C.** Sodium channel block produces opposite electrophysiological effects in canine ventricular epicardium and endocardium. *Circ Res* 69: 277-291, 1991.

49. **Leclercq C, Faris O, Tunin R, Johnson J, Kato R, Evans F, Spinelli J, Halperin H, McVeigh E, and Kass DA.** Systolic improvement and mechanical resynchronization does not require electrical synchrony in the dilated failing heart with left bundle-branch block. *Circulation* 106: 1760-1763, 2002.

50. **Leclercq C and Kass DA.** Retiming the failing heart: principles and current clinical status of cardiac resynchronization. *Journal of the American College of Cardiology* 39: 194-201, 2002.

51. **LeGrice IJ, Smaill BH, Chai LZ, Edgar SG, Gavin JB, and Hunter PJ.** Laminar structure of the heart: ventricular myocyte arrangement and connective tissue architecture in the dog. *Am J Physiol* 269: H571-582, 1995.

52. **LeGrice IJ, Takayama Y, and Covell JW.** Transverse shear along myocardial cleavage planes provides a mechanism for normal systolic wall thickening. *Circ Res* 77: 182-193, 1995.

53. **Lin DH and Yin FC.** A multiaxial constitutive law for mammalian left ventricular myocardium in steady-state barium contracture or tetanus. *J Biomech Eng* 120: 504-517, 1998.

54. **Lorenz CH, Walker ES, Morgan VL, Klein SS, and Graham TP, Jr.** Normal human right and left ventricular mass, systolic function, and gender differences by cine magnetic resonance imaging. *J Cardiovasc Magn Reson* 1: 7-21, 1999.

55. **MacGowan GA, Shapiro EP, Azhari H, Siu CO, Hees PS, Hutchins GM, Weiss JL, and Rademakers FE.** Noninvasive Measurement of Shortening in the Fiber and Cross-Fiber Directions in the Normal Human Left Ventricle and in Idiopathic Dilated Cardiomyopathy. *Circulation* 96: 535-541, 1997.

56. **Maniu CV, Patel JB, Reuter DG, Meyer DM, Edwards WD, Rihal CS, and Redfield MM.** Acute and chronic reduction of functional mitral regurgitation in experimental heart failure by percutaneous mitral annuloplasty. *J Am Coll Cardiol* 44: 1652-1661, 2004.

57. **Maron B, Bonow R, Cannon 3rd R, Leon M, and Epstein S.** Hypertrophic cardiomyopathy. Interrelations of clinical manifestations, pathophysiology, and therapy (1). *N Engl J Med* 316: 780-789, 1987.

58. **Mazhari R, Omens JH, Pavelec RS, Covell JW, and McCulloch AD.** Transmural distribution of three-dimensional systolic strains in stunned myocardium. *Circulation* 104: 336-341, 2001.

59. **McCulloch A, Smaill B, and Hunter P.** Regional left ventricular epicardial deformation in the passive dog heart. *Circ Res* 64: 721-733, 1989.

60. **McVeigh E and Zerhouni E.** Noninvasive measurement of transmural gradients in myocardial strain with MR imaging. *Radiology* 180: 677-683, 1991.

61. **Meunier J, Bertrand M, Mailloux GE, and Petitclerc R.** Local myocardial deformation computed from speckle motion. *Computers in Cardiology*, 1988, p. 133-136.

62. **Nelson GS, Curry CW, Wyman BT, Kramer A, Declerck J, Talbot M, Douglas MR, Berger RD, McVeigh ER, and Kass DA.** Predictors of Systolic Augmentation From Left Ventricular Preexcitation in Patients With Dilated Cardiomyopathy and Intraventricular Conduction Delay. *Circulation* 101: 2703-2709, 2000.

63. **O'Donnell M and Skovoroda R.** Internal Displacement and Strain Imaging Using Ultrasonic Speckle Tracking. *IEEE TRANSACTIONS ON ULTRASONICS, FERROELECTRICS, AND FREQUENCY CONTROL* 41, 1994.

64. **Omens JH, Usyk TP, Li Z, and McCulloch AD.** Muscle LIM protein deficiency leads to alterations in passive ventricular mechanics. *Am J Physiol Heart Circ Physiol* 282: H680-687, 2002.

65. **Oosthoek P, Viragh S, Lamers W, and Moorman A.** Immunohistochemical delineation of the conduction system. II: The atrioventricular node and Purkinje fibers. *Circulation Research* 73: 482-491, 1993.

66. **Pellerin D, Sharma R, Elliott P, and Veyrat C.** Tissue Doppler, strain, and strain rate echocardiography for the assessment of left and right systolic ventricular function. *Heart* 89: iii9-17, 2003.

67. **Penicka M, Bartunek J, De Bruyne B, Vanderheyden M, Goethals M, De Zutter M, Brugada P, and Geelen P.** Improvement of Left Ventricular Function After Cardiac Resynchronization Therapy Is Predicted by Tissue Doppler Imaging Echocardiography. *Circulation* 109: 978-983, 2004.

68. **Pitt B, Zannad F, Remme WJ, Cody R, Castaigne A, Perez A, Palensky J, Wittes J, and The Randomized Aldactone Evaluation Study Investigators.** The Effect of Spironolactone on Morbidity and Mortality in Patients with Severe Heart Failure. *N Engl J Med* 341: 709-717, 1999.

69. **Pitzalis MV, Iacoviello M, Romito R, Massari F, Rizzon B, Luzzi G, Guida P, Andriani A, Mastropasqua F, and Rizzon P.** Cardiac resynchronization therapy tailored by echocardiographic evaluation of ventricular asynchrony. *J Am Coll Cardiol* 40: 1615-1622, 2002.

70. **Prinzen FW, Augustijn CH, Allessie MA, Arts T, Delhaas T, and Reneman RS.** The time sequence of electrical and mechanical activation during spontaneous beating and ectopic stimulation. *Eur Heart J* 13: 535-543, 1992.

71. **Prinzen FW, Cheriex EC, Delhaas T, van Oosterhout MFM, Arts T, Wellens HJJ, and Reneman RS.** Asymmetric thickness of the left ventricular wall resulting from asynchronous electric activation: A study in dogs with ventricular pacing and in patients with left bundle branch block. *American Heart Journal* 130: 1045-1053, 1995.

72. **Prinzen FW, Hunter WC, Wyman BT, and McVeigh ER.** Mapping of regional myocardial strain and work during ventricular pacing: experimental study using magnetic resonance imaging tagging. *Journal of the American College of Cardiology* 33: 1735-1742, 1999.

73. **Prinzen T, Arts T, Prinzen F, and Reneman R.** Mapping of epicardial deformation using a video processing technique. *J Biomech* 19: 263-273, 1986.

74. **Purkinje J.** Mikroskopisch-neurologische Beobachtungen. *Arch Anat Physiol Wiss Med* 12: 281-295, 1845.

75. **Querejeta R, Lopez B, Gonzalez A, Sanchez E, Larman M, Martinez Ubago JL, and Diez J.** Increased Collagen Type I Synthesis in Patients With Heart Failure of Hypertensive Origin: Relation to Myocardial Fibrosis. *Circulation* 110: 1263-1268, 2004.

76. **Rijcken J, Bovendeerd P, Schoofs A, van Campen D, and Arts T.** Optimization of Cardiac Fiber Orientation for Homogeneous Fiber Strain During Ejection. *Annals of Biomedical Engineering* 27: 289-297, 1999.

77. **Rushmer R, Crystal D, and Wagner C.** The Functional Anatomy of Ventricular Contraction. *Circ Res* 1: 162-170, 1953.

78. **Saxon LA, De Marco T, Schafer J, Chatterjee K, Kumar UN, and Foster E.** Effects of Long-Term Biventricular Stimulation for Resynchronization on Echocardiographic Measures of Remodeling. *Circulation* 105: 1304-1310, 2002.

79. **Schenk S, Reichenspurner H, Boehm DH, Groetzner J, Schirmer J, Detter C, Koglin J, Schwaiblmair M, Meiser B, and Reichart B.** Myosplint implant and shape-change procedure: intra- and peri-operative safety and feasibility. *The Journal of Heart and Lung Transplantation* 21: 680-686, 2002.

80. **Schoenberg M.** Geometrical factors influencing muscle force development. II. Radial forces. *Biophys J* 30: 69-77, 1980.

81. **Scollan D, Holmes A, Zhang J, and Winslow R.** Reconstruction of Cardiac Ventricular Geometry and Fiber Orientation Using Magnetic Resonance Imaging. *Annals of Biomedical Engineering* 28: 934-944, 2000.

82. **Sengupta PP, Khandheria BK, Korinek J, Wang J, Jahangir A, Seward JB, and Belohlavek M.** Apex-to-Base Dispersion in Regional Timing of Left Ventricular Shortening and Lengthening. *J Am Coll Cardiol* 47: 163-172, 2006.

83. **Song X, Myronenko A, and Sahn D.** Speckle Tracking in 3D Echocardiography with Motion Coherence. *Computer Vision and Pattern Recognition, 2007 CVPR'07 IEEE Conference on*: 1-7, 2007.

84. **Sorger J, Wyman B, Faris O, Hunter W, and McVeigh E.** Torsion of the Left Ventricle During Pacing with MRI Tagging. *Journal of Cardiovascular Magnetic Resonance* 5: 521-530, 2003.

85. **Spotnitz HM, Spotnitz WD, Cottrell TS, Spiro D, and Sonnenblick EH.** Cellular basis for volume related wall thickness changes in the rat left ventricle. *J Mol Cell Cardiol* 6: 317-331, 1974.

86. **Spragg DD, Akar FG, Helm RH, Tunin RS, Tomaselli GF, and Kass DA.** Abnormal conduction and repolarization in late-activated myocardium of dyssynchronously contracting hearts. *Cardiovascular Research* 67: 77-86, 2005.

87. **Spragg DD, Leclercq C, Loghmani M, Faris OP, Tunin RS, DiSilvestre D, McVeigh ER, Tomaselli GF, and Kass DA.** Regional Alterations in Protein Expression in the Dyssynchronous Failing Heart. *Circulation* 108: 929-932, 2003.

88. **St John Sutton MG, Plappert T, Abraham WT, Smith AL, DeLurgio DB, Leon AR, Loh E, Kocovic DZ, Fisher WG, Ellestad M, Messenger J, Kruger K, Hilpisch KE, Hill MRS, and for the Multicenter InSync Randomized Clinical Evaluation (MIRACLE) Study Group.** Effect of Cardiac Resynchronization Therapy on Left Ventricular Size and Function in Chronic Heart Failure. *Circulation* 107: 1985-1990, 2003.

89. **Starling RC and Jessup M.** Worldwide clinical experience with the CorCap(TM) Cardiac Support Device. *Journal of Cardiac Failure Potential Impact of Cardiac Support Devices on Ventricular Remodeling in Heart Failure* 10: S225-S233, 2004.

90. **Streeter DD, Jr. and Hanna WT.** Engineering Mechanics for Successive States in Canine Left Ventricular Myocardium: I. Cavity and wall geometry. *Circ Res* 33: 639-655, 1973.

91. **Streeter DD, Jr., Spotnitz HM, Patel DP, Ross J, Jr., and Sonnenblick EH.** Fiber Orientation in the Canine Left Ventricle during Diastole and Systole. *Circ Res* 24: 339-347, 1969.

92. **Taber LA, Yang M, and Podszus WW.** Mechanics of ventricular torsion. *J Biomech* 29: 745-752, 1996.

93. **Thornell LE and Eriksson A.** Filament systems in the Purkinje fibers of the heart. *Am J Physiol Heart Circ Physiol* 241: H291-305, 1981.

94. **Usyk TP, Mazhari R, and McCulloch AD.** Effect of Laminar Orthotropic Myofiber Architecture on Regional Stress and Strain in the Canine Left Ventricle. *Journal of Elasticity* V61: 143-164, 2000.

95. **Uusimaa P, Risteli J, Niemela M, Lumme J, Ikaheimo M, Jounela A, and Peuhkurinen K.** Collagen Scar Formation After Acute Myocardial Infarction : Relationships to Infarct Size, Left Ventricular Function, and Coronary Artery Patency. *Circulation* 96: 2565-2572, 1997.

96. **van Oosterhout MFM, Prinzen FW, Arts T, Schreuder JJ, Vanagt WYR, Cleutjens JPM, and Reneman RS.** Asynchronous Electrical Activation Induces Asymmetrical Hypertrophy of the Left Ventricular Wall. *Circulation* 98: 588-595, 1998.

97. **Vasan RS, Larson MG, Benjamin EJ, Evans JC, Reiss CK, and Levy D.** Congestive heart failure in subjects with normal versus reduced left ventricular ejection fraction: Prevalence and mortality in a population-based cohort. *J Am Coll Cardiol* 33: 1948-1955, 1999.

98. **Vesely I, Fawzy H, Fukamachi K, and Drake Jr M.** Use of Three-Dimensional Sonomicrometry to Study the Motion of the Mitral Valve. *ASAIO Journal* 43: M470, 1997.

99. **Vetter FJ and McCulloch AD.** Three-dimensional analysis of regional cardiac function: a model of rabbit ventricular anatomy. *Prog Biophys Mol Biol* 69: 157-183, 1998.

100. **Villarreal FJ, Waldman LK, and Lew WY.** Technique for measuring regional two-dimensional finite strains in canine left ventricle. *Circ Res* 62: 711-721, 1988.

101. **Waldman LK, Fung YC, and Covell JW.** Transmural myocardial deformation in the canine left ventricle. Normal in vivo three-dimensional finite strains. *Circ Res* 57: 152-163, 1985.

102. **Watkins H.** Familial hypertrophic cardiomyopathy: a genetic model of cardiac hypertrophy. *Human Molecular Genetics* 4: 1721-1727, 1995.

103. **Weber K, Janicki J, Shroff S, Pick R, Chen R, and Bashey R.** Collagen remodeling of the pressure-overloaded, hypertrophied nonhuman primate myocardium. *Circ Res* 62: 757-765, 1988.

104. **Wildenthal K and Mitchell JH.** Dimensional analysis of the left ventricle in unanesthetized dogs. *J Appl Physiol* 27: 115-119, 1969.

105. **Wyman BT, Hunter WC, Prinzen FW, Faris OP, and McVeigh ER.** Effects of single- and biventricular pacing on temporal and spatial dynamics of ventricular contraction. *Am J Physiol Heart Circ Physiol* 282: H372-379, 2002.

106. **Wyman BT, Hunter WC, Prinzen FW, and McVeigh ER.** Mapping propagation of mechanical activation in the paced heart with MRI tagging. *Am J Physiol Heart Circ Physiol* 276: H881-891, 1999.

107. **Wyndham C, Smith T, Meeran M, Mammana R, Levitsky S, and Rosen K.** Epicardial activation in patients with left bundle branch block. *Circulation* 61: 696-703, 1980.

108. **Young J, Abraham W, Smith A, Leon A, Lieberman R, Wilkoff B, Canby R, Schroeder J, Liem L, and Hall S.** Combined Cardiac Resynchronization and Implantable Cardioversion Defibrillation in Advanced Chronic Heart Failure The MIRACLE ICD Trial. In: *JAMA*: Am Med Assoc, 2003, p. 2685-2694.

109. **Zerhouni E, Parish D, Rogers W, Yang A, and Shapiro E.** Human heart: tagging with MR imaging--a method for noninvasive assessment of myocardial motion. *Radiology* 169: 59-63, 1988.

110. **Zimmerman SD, Criscione J, and Covell JW.** Remodeling in myocardium adjacent to an infarction in the pig left ventricle. *Am J Physiol Heart Circ Physiol* 287: H2697-2704, 2004.

2. Methods

In order to develop an understanding of the three-dimensional electromechanics of the canine left ventricle, several methods were developed or adapted from previous use. In all of the experiments, analysis of deformation was a primary goal, regardless of experimental treatments (e.g. physiologic/hemodynamic changes, artificial pacing). All deformation analyses were performed using biplane X-ray imaging of implanted, radiopaque markers in open-chest, anaesthetized dogs.

2.1. Open-Chest Surgical Preparation

All animal studies were performed according to the National Institutes of Health *Guide for the Care and Use of Laboratory Animals*. All protocols were approved by the Animal Subjects Committee of the University of California, San Diego, which is accredited by the American Association for Accreditation of Laboratory Animal Care.

Adult mongrel dogs (20–28 kg) were anesthetized with intravenous propofol (6 mg/kg), intubated, and mechanically ventilated with isoflurane (0.5–2.5%), nitrous oxide (2 l/min), and medical oxygen (2 l/min) to maintain a surgical plane of anesthesia. Catheters were inserted into the right and left femoral veins for venous access. A 9-Fr arterial introducer was placed in the left femoral artery. The heart was exposed via a median sternotomy and a left thoracotomy at the fourth intercostal space. The pericardium was opened, and the heart suspended in a pericardial cradle. A pair of pacing wires were sutured to the right or left atrium and used for atrial pacing. An 8-Fr pigtail micromanometer catheter with a lumen (Millar Instruments, Houston, TX) was inserted through a 9-Fr arterial introducer placed in the left femoral artery, and the

catheter tip was advanced into the LV. LV pressure was recorded with the pigtail micromanometer catheter, and the calibration was adjusted such that the end-diastolic pressure and peak LV pressure matched those recorded from a fluid-filled transducer connected to the lumen of the catheter. LV end diastolic pressure (LVEDP) was calculated by finding dP/dt_{max} and working backwards in time until dP/dt reached 5% of the maximum value. In the case of atrial pacing, this coincided closely with the notch in the pressure trace as well as the peak of the R-wave on the electrocardiogram (ECG). A flow probe (Transonic Systems, Model #T208, Ithaca, NY) was placed on the ascending aorta to assess the onset and end of ejection. Stroke volume was obtained by integration of the aortic blood flow signal.

2.2. Bead Insertion

In order to track the deformation of the myocardium, material markers are necessary. For the purposes of these experiments the markers must be radio-opaque so that they appear clearly on the X-ray images (e.g. lead, gold). They may, however, be placed at any depth within the ventricular wall, because the X-rays easily penetrate through the tissue. Figure 2.1 shows the tools typically used to insert the beads. In short, the bead inserter consists of a sharp, hollow trocar and a plunger. The procedure is as follows: 1) The trocar is inserted into the myocardium to the desired depth; 2) A small (0.8-1.0mm diameter) bead is dropped into the trocar; 3) the plunger is inserted the full length of the trocar, forcing the bead to the extent of the trocar; and finally 4) the trocar/plunger combination is removed, leaving the bead in place. In the case of the adjustable depth trocar (figure 2.1), multiple beads are placed approximately 1-2 mm

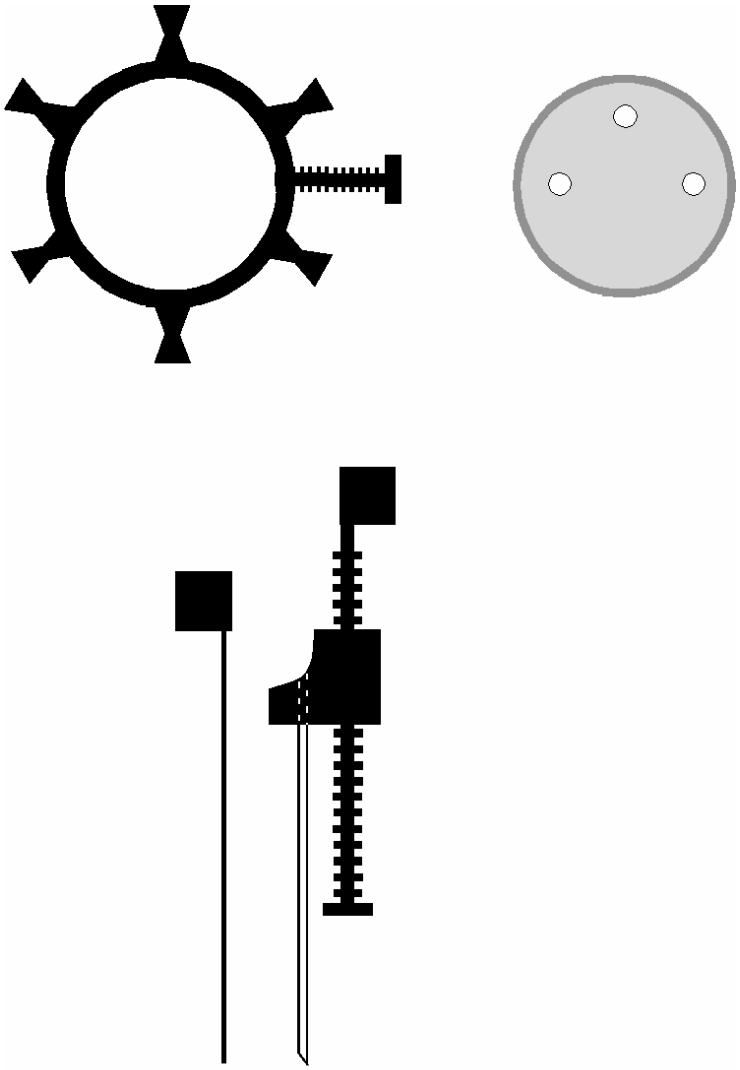

Figure 2.1: Bead Inserting Instruments
The platform (top, left) is sutured to the epicardial surface by 2-3 of the 6 flanges. The plexiglass guide (top, right) is then placed within the platform. The 3 guide holes can be rotated, and then fixed with a set screw. Rotating the guide holes makes it possible to avoid coronary arteries. The trocar (bottom) is then inserted through each of the guide holes. The trocar length can be varied by the screw mechanism.

apart through the thickness of the wall. Typically, three columns of transmural beads are inserted close together so that three-dimensional deformations can be determined.

In addition to this intramyocardial bead technique, beads (with drilled holes) can also be sewn to the epicardial surface with standard 4-0 suture. These are typically larger than the intramyocardial beads, ranging from 1.3 mm to 2.0 mm in diameter.

2.3. Cineradiography

The laboratory is equipped with a high speed (125 frames/s) bi-plane cineradiographic system with multiple degrees of freedom. This allows for non-orthogonal imaging planes. The anteroposterior (A/P) view is mounted on a C-arm and can be rotated about the animal's caudal-cranial axis or skewed along that axis. It can also be translated medially/laterally. The lateral view can be translated along the caudal-cranial axis or the dorsal-ventral axis, and also can be rotated about the caudal-cranial axis. In addition, the table can be translated in all directions and rotated in the plane parallel to the floor.

Digital cameras are mounted on the back of each x-ray image intensifier. In continuous capture mode, the cameras run at 125 frames/s with an exposure time of 7.8 ms. The cameras can also run in triggered mode, using slower acquisition rates and variable exposure times. The images are saved as 640 x 480 pixel bitmaps (uncompressed).

2.4. Correction of Spherical Distortion

The digital images are recorded from the X-ray image intensifiers. Due to the shape of the camera lens, all the light focused by the lens does not have a common focal point, a phenomenon known as spherical aberration. The result is a distorted two dimensional image. This can be visualized by placing a rectangular object that spans the camera's field of view; the resulting image will look like a pincushion (this is a special case – other image deformations are possible with different lens types). In order to minimize the effects of distortion on the precision of the two-dimensional coordinates, the images were corrected based on the known distortion profile of the camera lens. To determine this distortional profile, we imaged a grid of beads with known spacing, affixed as closely as possible to the image intensifier. This was done separately for each of the two cameras, prior to performing a three-dimensional reconstruction.

Cubic Hermite interpolation was used to determine the distortional effects on the rectangular grid of beads. This requires solution of the following least squares minimization problem:

$$\arg\min \sum_{i=1}^{40} (P_i^{actual} - H_i \cdot X_i)^2 \tag{2.1}$$

where $\mathbf{P}^{\text{actual}}$ represents the known coordinates of the beads, $\mathbf{H}_i$ represents the values of the Hermitian basis functions at point i, and $\mathbf{X}_i$ represents the parameters characterizing the distortion of the element (the values and derivatives at the corners of the element). Because $\mathbf{P}^{\text{actual}}$ is known and $\mathbf{H}$ can be determined from the measured coordinates of the bead grid, equation (2.1) can be rearranged as a least squares minimization to solve for $\mathbf{X}$:

$$\mathbf{X} = (\mathbf{H}^{\mathrm{T}}\mathbf{H})^{-1}\mathbf{H}^{\mathrm{T}}\mathbf{P}^{\text{actual}} \tag{2.2}$$

Once X is determined, it can be used to transform coordinates of any arbitrary point from image coordinates to "true" coordinates through the equation:

$$Q = X*H^{meas} \tag{2.3}$$

Where Q is the corrected coordinate, X is found from the solution of Equation (2.2), and H^{meas} contains the values of the Hermitian basis functions evaluated at an image coordinate.

2.5. Three-Dimensional Reconstruction

The non-orthogonal biplane X-ray images dive projections of the three-dimensional image space. In order to back-calculate the perspective transformations, a phantom is inserted into the X-ray field at the completion of the experimental study. The phantom consists of 1 mm beads drilled into a plexiglass cylinder in a helical fashion. The relative three-dimensional coordinates of the phantom's beads are known. Using a linear least-square fitting procedure, perspective transformations can be calculated for the A/P and lateral views:

$$\arg\min \sum (T_i - \mathbf{C}M_i)^2 \tag{2.4}$$

where T_i represents the true coordinates of the phantom in the form [x,y,z,1] with size, C is a camera matrix which represents the perspective transformation [4 x 3], and M_i is the measured image coordinates in the form [u,v,1]. Once again, this equation can be rearranged to solve for the 4 x 3 perspective transformation **C**.

$$C = TM^T(MM^T)^{-1} \tag{2.5}$$

A minimum of approximately nine phantom beads are required for stability of the fitting procedure.

2.6. Histology

In order to determine fiber and sheet orientations, the hearts were fixed in *situ* with 2.5% gluteraldehyde, at the end diastolic pressure of the study. To avoid the distortional effects of dehydration and shrinkage associated with embedding, histological measurements were obtained with freshly fixed heart tissue. A transmural rectangular block of tissue in the implanted bead set was carefully removed from the ventricular wall, with the edges of the block cut parallel to the local circumferential, longitudinal, and radial axes of the LV as determined from the same epicardial markers used for the strain analysis. The transmural thickness of the block was measured, and the block was sliced into 1-mm-thick sections parallel to the epicardial tangent plane, forming a series from the epicardium to the endocardium to measure the fiber angles across the LV wall. Fiber angle (α) was determined under a dissection microscope with reference to the positive circumferential axis (figure 2.2). Mean α was measured at each transmural depth as described previously. Each 1-mm slice of tissue was then embedded with Tissue-Tek OCT compound (Sakura Finetek USA, Torrance, CA) and quickly frozen in a 2-methylbutane bath cooled with dry ice. Multiple serial thin sections (5-10 μm) perpendicular to the mean fiber direction were made from each slice of tissue, transferred to a glass slide, and allowed to desiccate for 10 min. Digital images of the tissue section were acquired at low-power magnification (x20) with a digital camera (Coolpix 990; Nikon, Melville, NY) mounted on a light microscope (Optiphot-2; Nikon). The images were transferred to a Windows-based computer with image processing software (Image J version 1.36; NIH). Myocardial laminae, or sheets, were directly visible with no further enhancement. Sheet angle (β) was measured with reference to the positive radial axis

(figure 2.2). Approximately 10 sections were taken from each depth through the wall. This process was repeated from the epicardial slice to the endocardial slice to yield transmural distribution of sheets. The process is summarized in figure 2.2. In the analysis of chapter 4, the sections were used to determine the mean sheet angle, while in chapter 5, the distributions of sheet angle were used as is.

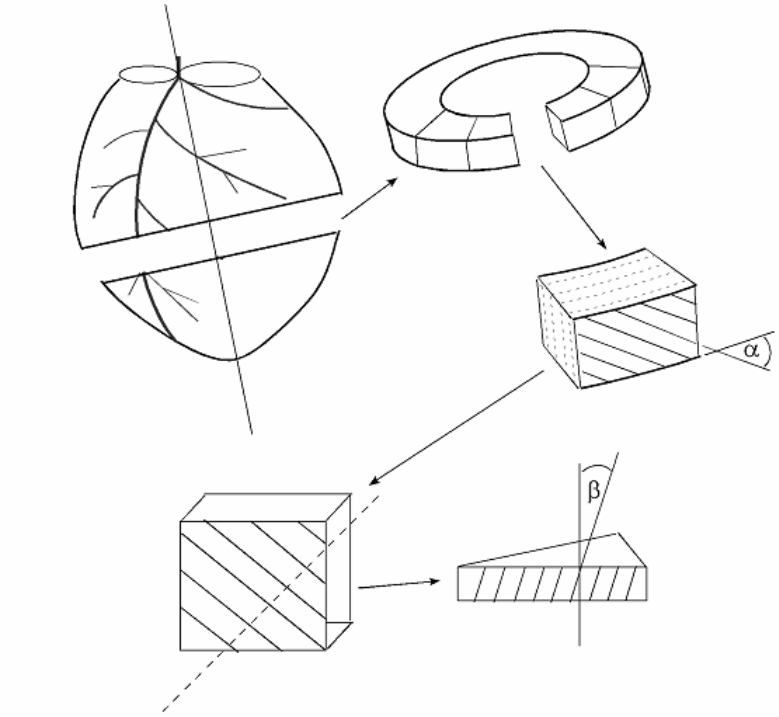

Figure 2.2: Sectioning Scheme
First, a short-axis slice is cut from the heart in the region of interest, such that it is parallel to the long axis of the heart. This is then further sectioned into a block in the region of interest. At each depth through this transmural block, the following iterative process is repeated: 1) measure the mean fiber angle, α; 2) make a cut perpendicular to the mean fiber direction; 3) section the remaining piece of the heart to determine either the mean sheet angle or its distribution.

3. Dyssynchronous Ventricular Activation: Mechanics of the Late-Activated Regions

3.1. Abstract

Abnormal electrical activation of the left ventricle results in mechanical dyssynchrony, which is in part characterized by early stretch of late-activated myofibers. To describe the pattern of deformation during 'prestretch' and gain insight into its causes and sequelae, we implanted midwall and transmural arrays of radiopaque markers into the left ventricular anterolateral wall of open-chest, isoflurane-anesthetized, adult mongrel dogs. Biplane cineradiography (125 Hz) was used to determine the time course of two- and three-dimensional strains while pacing from a remote, posterior wall site. Strain maps were generated as a function of time. Electrical activation was assessed with bipolar electrodes. Posterior wall pacing generated prestretch at the measurement site, which peaked 44 ms after local electrical activation. Overall magnitudes and transmural gradients of strain were reduced when compared to passive inflation. Fiber stretch was larger at aortic valve opening compared to end diastole ($p < 0.05$). Fiber stretch at aortic valve opening was weakly but significantly correlated with local activation time ($R^2 = 0.319$, $p < 0.001$). With a short atrio-ventricular delay, fiber lengths were not significantly different at the time of aortic valve opening during ventricular pacing compared to atrial pacing. However, ejection strain did significantly increase ($p < 0.05$). We conclude that the majority of fiber stretch occurs after local electrical activation and mitral valve closure, and is different from passive inflation. The increased shortening of these regions appears to be due to a reduced afterload rather than an effect of length-dependent activation in this preparation.

3.2. Introduction

Ventricular epicardial activation results in a heterogeneous pattern of contraction such that the timing of the onset of local shortening mirrors the spread of the electrical depolarization wave front. As the region near the pacing site shortens, remote late activated regions lengthen. Previous studies have observed this lengthening in late activated regions which has been termed 'prestretch' by several investigators (2, 6, 16). These studies have used a wide variety of techniques including ultrasonic crystals (2), surface markers (16), and magnetic resonance imaging (MRI) (17) to quantify the prestretch. Most of these studies have shown augmented ejection shortening at late activated sites relative to early activated sites, implying that prestretch may improve performance via muscle fiber length-dependent activation. However, they did not determine if prestretch is different from passive distension or assess its timing relative to ventricular pressure generation. Moreover, none have examined the transmural gradient in prestretch or muscle fiber length changes in the prestretched, late activated areas.

Thus the aim of the present study was to test the hypothesis that the late-activated regions of the left ventricle distend in the same manner as passive filling, and that the functional consequences of prestretch are the result of changes in length-dependent activation. To achieve this, midwall and transmural arrays of radiopaque markers and bipolar electrodes were implanted into the left ventricular (LV) free wall of open-chest dogs to describe myofiber deformation at high temporal and spatial resolution during atrial and ventricular activation.

In this study we show that, in contrast to passive distension, prestretch is uniform transmurally. The majority of prestretch occurs during isovolumic contraction, after the

prestretched tissue has been electrically activated and the mitral valve has closed. Both of these findings support the conclusion that prestretch occurs in tissue that is actively generating force. We confirm that at aortic valve opening late-activated tissue is at a longer muscle length than early-activated tissue. This dyskinesis is widely thought to produce the decrease in function observed in epicardial pacing. However, at least at short atrioventricular (A-V) delays, the muscle length in late-activated tissue is not significantly different from normal contraction, while early-activated fibers are shorter. This not only provides insight into the decrease in function occurring with epicardial activation but also emphasizes the importance of A-V delay for clinical approaches such as cardiac resynchronization therapy.

3.3. Materials and Methods

All animal studies were performed according to the National Institutes of Health *Guide for the Care and Use of Laboratory Animals*. All protocols were approved by the Animal Subjects Committee of the University of California, San Diego, which is accredited by the American Association for Accreditation of Laboratory Animal Care.

Surgical preparation

Ten adult mongrel dogs (21–24 kg) were anesthetized with intravenous propofol (6 mg/kg), intubated, and mechanically ventilated with isoflurane (0.5–2.5%), nitrous oxide (2 l/min), and medical oxygen (2 l/min) to maintain a surgical plane of anesthesia. Five dogs were implanted with midwall marker arrays, and five were implanted with transmural marker arrays. All underwent the same surgical procedure, as follows. The heart was exposed via a median sternotomy and a left thoracotomy at the fourth intercostal space, and then placed in a pericardial cradle. An 8-Fr pigtail micromanometer catheter with a lumen (Millar Instruments, Houston, TX) was inserted through a 9-Fr arterial introducer placed in the left femoral artery, and the catheter tip was advanced into the LV. LV pressure was recorded with the pigtail micromanometer catheter, and the calibration was adjusted such that the end-diastolic pressure and peak LV pressure matched those recorded from a fluid-filled transducer connected to the lumen of the catheter. LV end diastolic pressure (LVEDP) was calculated by finding dP/dt_{max} and working backwards in time until dP/dt reached 5% of the maximum value. In the case of atrial pacing, this coincided closely with the notch in the pressure trace as well as the peak of the R-wave on the electrocardiogram (ECG). A flow probe

(Transonic Systems, Model #T208, Ithaca, NY) was placed on the ascending aorta to assess the onset and end of ejection. Stroke volume was obtained by integration of the aortic blood flow signal.

In one group of five dogs, radiopaque markers were used as follows to measure 2D myocardial deformation in each heart. Lead beads (2 mm diameter) were sutured to the apical dimple (apex bead) and on the epicardium at the bifurcation of the left anterior descending (LAD) and left circumflex coronary arteries (base bead) to provide end points for a LV long axis. Gold (0.9 mm) or lead (1.2 mm) beads were plunged into the anterolateral wall in a rectangular pattern, forming a surface approximately parallel to the epicardium (see figure 3.1).

Bipolar plunge electrodes were constructed by passing two 36-gauge dual-insulated magnet wires (Belden CDT Inc., Richmond, IN) through the end of a 23-gauge needle and bending back the tips to form hooks. The wires were electrically isolated except at the tips, with inter-electrode spacing varying between 1 and 5 mm, depending on how the hooks (and non-insulated wire tip) engaged the myocardium. Eight electrodes were evenly spaced around the edges of the array and a ninth was placed in the center, all at the approximate depth of the beads (see figure 3.1). Bipolar electrodes were also used to pace the LV from the posterior wall epicardium, near the equator. Finally, a pair of pacing wires was sutured to the left atrium (LA).

Experimental Protocol

Atrial pacing was performed by stimulating LA electrodes, and LV pacing was performed by stimulating both LA and LV electrodes (A-V delay = 35 ms), using a

square-wave constant-voltage electronic stimulator (model SD9; Grass Instruments, Quincy, MA) at a frequency 20% above baseline heart rate to suppress native sinus rhythm. Stimulation parameters (voltage 10% above threshold, duration 8 ms, and frequency) were kept constant in each animal. Each animal was positioned in a biplane radiography system, and synchronous biplane cineradiographic images (125 frames/sec) of the bead markers were digitally acquired with mechanical ventilation suspended at end expiration. The LV pressure (LVP), arterial pressure, surface ECG and bipolar plunge electrograms were recorded simultaneously with the cineradiographic images. Recordings were obtained during atrial pacing and then following approximately 2 to 5 minutes of ventricular pacing (to achieve a steady hemodynamic state). Atrial pacing was continued between ventricular pacing runs.

Histology

After the functional data acquisition was complete, a 22- to 26-Fr cannula with side holes was inserted into the ascending aorta through a brachiocephalic artery, and the animals were euthanized with pentobarbital sodium and the heart was brought to arrest. The coronary arteries were perfused with normal saline and the LV pressure was adjusted to the end-diastolic pressure observed during the study before fixing the heart with 2.5% buffered gluteraldehyde, as described previously (1). The fixed, silastic-filled heart was skewered from the apical dimple to the mitral aspect of the aortic valve, to define the LV long axis (18). It was then sectioned as shown in figure 3.3, yielding a total of approximately 25 transmural samples from within the bead array. The transmural thickness of the block was measured, and the block was sliced into 1-mm-thick sections

parallel to the epicardial tangent plane, forming a series of sections from the epicardium to the endocardium used to measure the fiber angles across the LV wall. After measuring all of the angles in one transmural section, least squares linear regression was used to fit the transmural data. This process was repeated in each of the samples, for use in the strain analysis described below.

Data Analysis

Nine electrode pairs were used in each experiment, but an average of 1 per study were excluded because the time of activation could not be determined due to system noise or recording failure. Electrical activation time was defined as the time from the ventricular stimulus to the initial voltage deflection (see figure 3.4, dotted line). This definition was used rather than other common definitions in order to remain consistent in the analysis of all electrograms, since some waveforms looked monophasic while others were biphasic.

Three-dimensional coordinates of markers were reconstructed from the cineradiographic images (1). The basic data analysis uses a homogenous strain calculation based on a triad of markers (13). This technique assumes a homogeneous distribution of strain within a triangle formed by 3 material markers (8). Myocardial markers were grouped automatically to form triangles with minimum height of 2.5 mm and maximum area of 60 mm^2. Additional triangles of larger area were then added manually in areas of low bead density, to ensure coverage of the array. A single marker was often used in multiple adjacent triangles. These constraints resulted in approximately 50 triangles (functional data points) per array. The coordinate axes were defined

individually in each triangle, using the following method. First, the outward facing normal vector (local radial direction) of the triangle was determined. Next, the circumferential direction was determined by finding a vector perpendicular to both the radial direction and the LV long axis, pointing towards the septum. Finally, the longitudinal direction was determined by finding a vector perpendicular to the radial and circumferential directions, pointing towards the apex. This process ensures that the circumferential and longitudinal directions lie in the plane of the triangle (see figure 3.2).

Two-dimensional Lagrangian finite strains could then be calculated with respect to cardiac coordinates at the centroid of each triangle, as reported previously (13, 19). Strains were also transformed into fiber coordinates by rotating the strains by the fiber angle α at the location of that triangle's centroid. This angle was calculated as a weighted average of the 3 nearest measurements to the centroid (weighting inversely proportional to distance). Thus the fiber and cross-fiber strains within each triangle were found.

Three-dimensional triangle centroid locations were then projected onto a two-dimensional grid, such that the plane of the grid was perpendicular to the radial direction of an arbitrary triangle located near the center of the array. By representing all the strains from a single time point at their respective centroid locations on the grid, a spatial distribution of strain could then be fit using the MATLAB function griddata (The Mathworks, Inc., Natick, MA) and visualized as a color map. Cubic interpolation was used to ensure smooth gradients between adjacent strain measurements.

Areas were considered prestretched if the maximum fiber strain prior to aortic valve opening (relative to the pacing stimulus) exceeded 0.02, the approximate resolution

limit of the technique. Aortic valve opening strain was defined as the strain at the time of aortic valve opening during ventricular pacing with respect to that same hemodynamic reference during atrial pacing. This quantity was only defined in areas that were prestretched with ventricular pacing. Similarly, ejection strain was defined as the strain at the time when the aortic valve closes with respect to the time it opens, in the same areas used to define aortic valve opening strain.

Transmural Arrays

A second group of five dogs was used to measure 3-D myocardial deformation. The same surgical preparation was used, except that the midwall bead array was replaced with three transmural columns of four to five 0.8-mm-diameter gold beads and a 1.7-mm-diameter surface gold bead above each column. The beads were placed within the anterior wall between the first and the second diagonal branches of the LAD. The experimental protocol was also the same, with the addition of epicardial pacing at the site of the array. The data analysis was performed by determining a continuous polynomial position field that mapped the beads in the undeformed reference configuration to those in the deformed configuration. Differentiation of this field with respect to undeformed position yields a continuous, nonhomogeneous transmural distributions of 3D finite strains(1, 5).

Statistical Analysis

Values are means ± SD unless otherwise specified. A one-factor repeated measures ANOVA was used to assess the effect of time during the cardiac cycle on fiber

strain. Tukey's test was used for post hoc comparisons. For aortic valve opening strains, a one-sample t-test with two-tailed P value was used. For all other statistics, a paired t-test with two-tailed P value was used. Statistics were performed using SigmaStat version 3.0 (SPSS; Chicago, IL). Significance was accepted at $P < 0.05$.

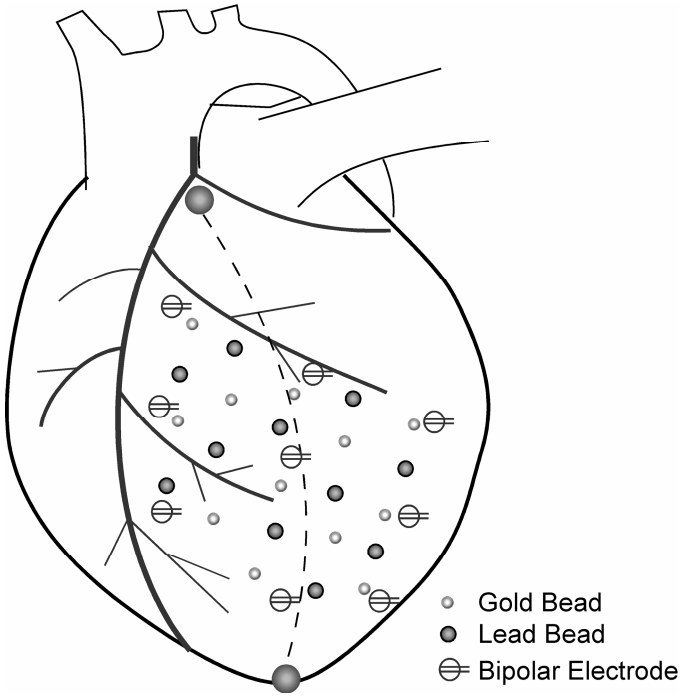

Figure 3.1: Regional Bead Array Schematic
The bead array consisted of alternating gold and lead beads, in order to simplify the matching of points in the anteroposterior (AP) and lateral (LAT) radiographic views. Beads were plunged into the midwall, approximately 60% through the transmural thickness. The array spanned longitudinally from the apex to the first diagonal of the LAD, and circumferentially from the LAD to the posterior descending artery (not shown). Circles with two straight lines protruding indicate location of bipolar electrodes for electrical activation recordings, which were at the same depth as the beads.

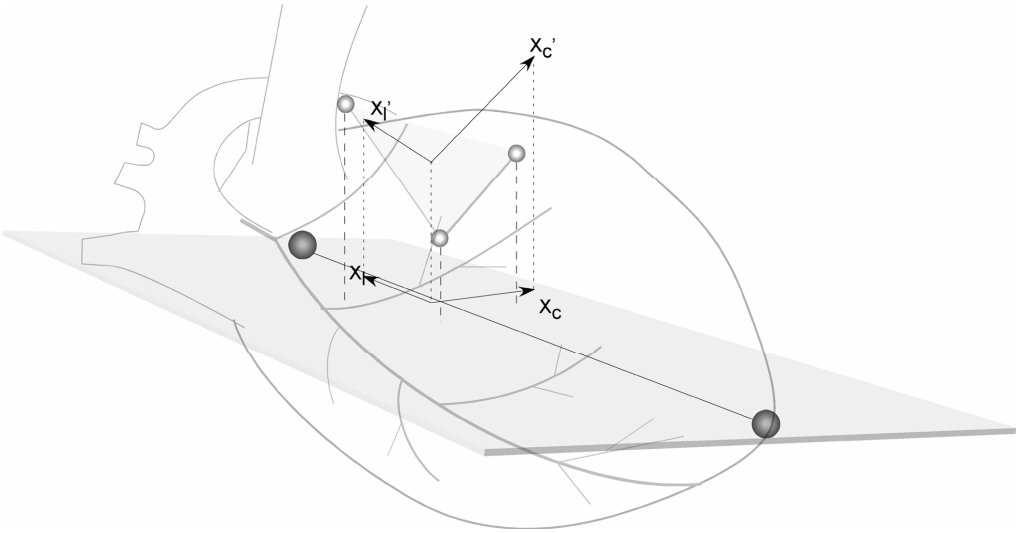

Figure 3.2: Cardiac Coordinate System
Schematic representation of one triangle, illustrating the coordinate directions. X_c and X_l represent the circumferential and longitudinal direction in terms of cardiac coordinates. X_c' and X_l' represent the equivalent coordinate directions in terms of a local triangle coordinate system, used in strain calculations. Projections of X_c' and X_l' align with X_c and X_l.

3.4. Results

Midwall Arrays

The results of this study are from five open chest, isoflurane anesthetized dogs with bead arrays implanted into the left ventricular free wall. Table 1 summarizes the hemodynamic results. LVEDP was not significantly different following left ventricular pacing. Peak LV pressure, average systolic pressure, stroke volume, dP/dt_{max} and dP/dt_{min} were all significantly reduced following ventricular pacing.

Bead depths & Fiber Orientation

25 ± 2 (range 23 to 28) beads (gold, 0.9mm or lead, 1.2mm) were plunged to an average depth of 7.0±1.6 mm (64.3±14.6 % wall depth) spanning from 31.4 ± 5.0 % to 81.9 ± 3.5 % of the apex-base distance with a width of 5.0 ± 0.7 cm at the widest point. Myocardial markers were grouped to form triangles of area 41.6 ± 16.9 mm^2 (range 10.6 to 115.9 mm^2). In all five animals the number of triangles ranged from 37 to 59, with an average of 48 ± 10 triangles.

In order to understand the deformation data in the context of the fiber anatomy, fiber angles throughout the array were measured histologically. At the depth of the array, myofibers were found to be oriented at an average of +27.5 ± 22.1º from circumferential, consistent with previous findings of fiber angle at this depth when compared at apical (1, 5) and basal sites (5). The average range of fiber angle within the array was 72.0 ± 5.0º.

Table 3.1: Hemodynamic Results
LVP, Left Ventricular Pressure, HR, heart rate, EDP, end-diastolic pressure. * $P < 0.05$ vs. Atrial Pacing.

	HR (bpm)	LVEDP (mmHg)	LVP_{peak} (mmHg)	$+dP/dt_{max}$ (mmHg/sec)	$-dP/dt_{max}$ (mmHg/sec)	Average Systolic Pressure (mmHg)	Stroke Volume (mL)
Atrial Pacing	104.2±4.1	6.8±1.7	97.3±11.4	1776±505	-1387±343	87.7±10.1	16.5±3.1
LV Pacing	104.1±4.1	6.2±4.5	84.2±9.0*	1451±350*	-1050±277*	74.3±9.3*	13.6±2.2*
% Change	-0.1%	-8.8%	-13.4%	-18.3%	-24.3%	-15.4%	-18.0%

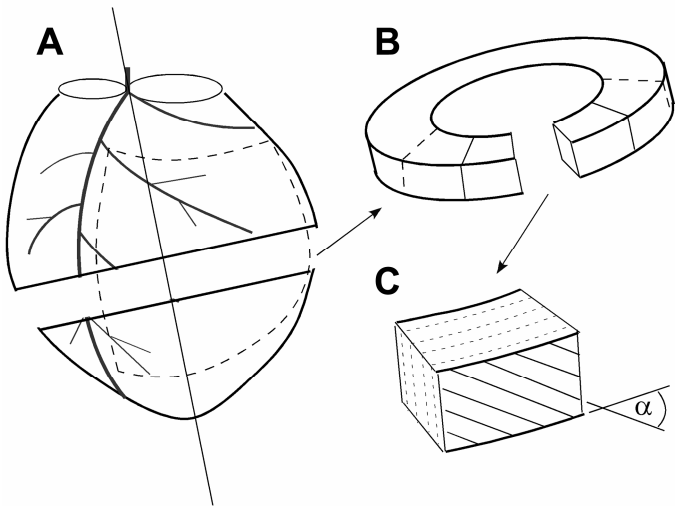

Figure 3.3: Histological Procedure for Measuring Fiber Angles
A: The heart was skewered along the long axis and cut into 5 or 6 rings perpendicular to this axis. B: Each ring was then further sectioned into blocks in the area of the beads. C: Each block was sliced into 1 mm thick sections cut perpendicular to the epicardial tangent plane. Fiber angle (α) was determined under a dissection microscope with reference to the positive circumferential axis.

Timing of Prestretch

Figure 3.4 shows a typical time course of fiber strain (E_{ff}) in one triangle and the bipolar electrogram of the nearest electrode. Fiber strain data from the whole array for this animal are shown in figure 3.5, where the location of the triangle shown in figure 3.4 is outlined. The strain maps shown in figure 3.5 were obtained at the times marked by vertical lines in figure 3.4. Referring to figure 3.4, 85% of the prestretch occurs between end diastole (dashed line) and aortic valve opening (solid line); it peaks 59 ms after the time of local activation.

Figure 3.6 shows the average values of strain components in areas that were prestretched. Fiber strain (E_{ff}) was significantly increased, with an average of 68% of total prestretch occurring during isovolumic contraction. Crossfiber strain (E_{cc}) and fiber-crossfiber shear strain (E_{fc}) were not significantly different. In each animal peak prestretch occurred an average of 44 ± 23 ms after activation of the nearest bipolar electrode. The spatial distribution of prestretch varied from animal to animal; figure 3.5 shows a typical result. The majority of prestretch occurred along the septal border and was somewhat patchy in distribution.

Activation Time vs. Prestretch

Previous studies such as those performed with MRI (21) have shown that there appears to be a relationship between distance from the pacing site and midwall circumferential strain. We sought to quantify this regional pattern of stretch in terms of fiber function. As shown in figure 3.7, there was a general relationship between time of

electrical activation and magnitude of maximum prestretch. Linear regression yielded a correlation coefficient $R^2 = 0.319$, with a slope of 1.2935/sec which was significantly different from zero ($P < 0.001$). The intercept, -0.0041, was not significantly different than zero.

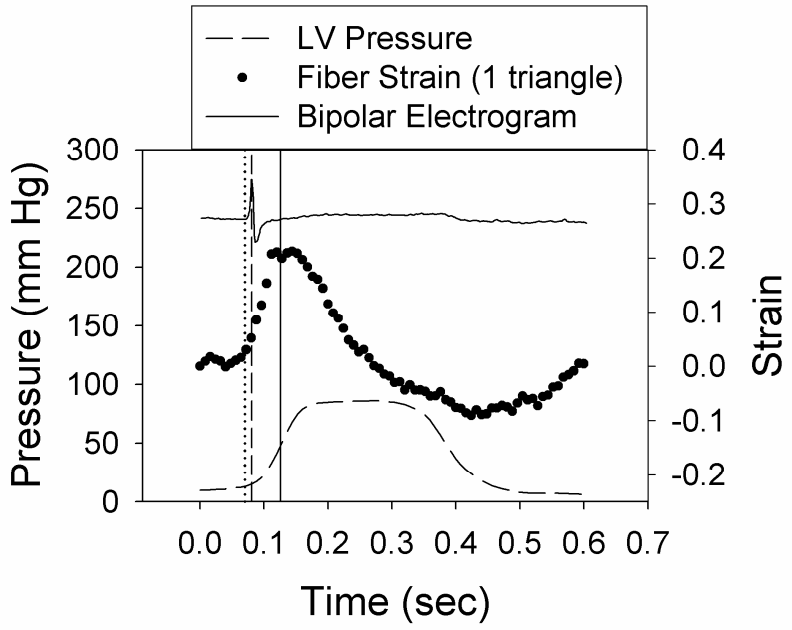

Figure 3.4: Prestretch as a Function of Pressure and Activation
LV pressure, fiber strain in one triangle, and nearest bipolar electrogram plotted as a function of time during ventricular pacing for dog 1. Time = 0 represents the ventricular pacing stimulus, and the data depicts a full cardiac cycle. Vertical lines indicate time of local activation (dotted), end diastole (dashed), and opening of the aortic valve (solid).

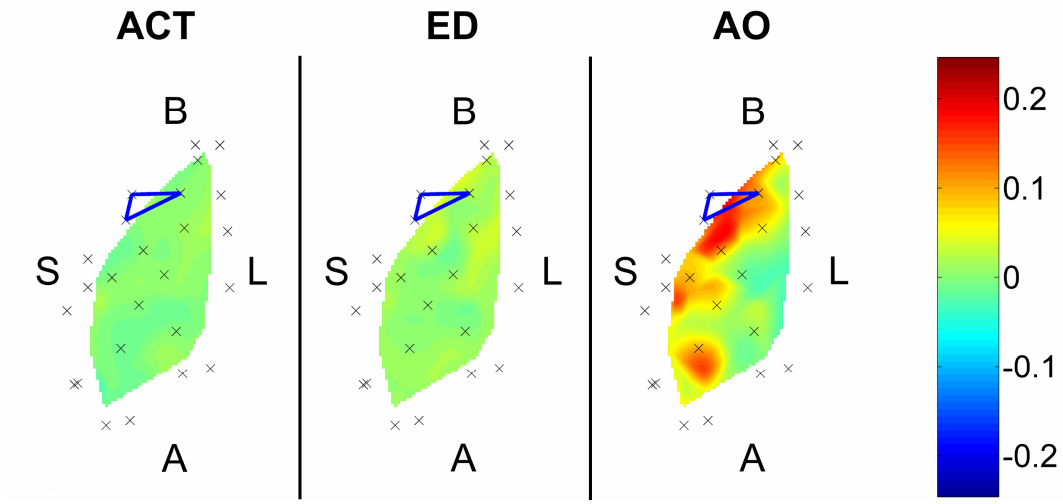

Figure 3.5: Strain Maps at Three Stages of the Cardiac Cycle
Spatial distribution of fiber strain in dog 1 at 3 time points: (ACT) average time of activation, (ED) end diastole, and (AO) aortic valve opening. Red (positive) strains indicate stretching, while blue (negative) strains indicate shortening. X's represent locations of beads. The outlined triangle has the time course shown in figure 3.3. B: base, A: apex, S: septum, L: lateral.

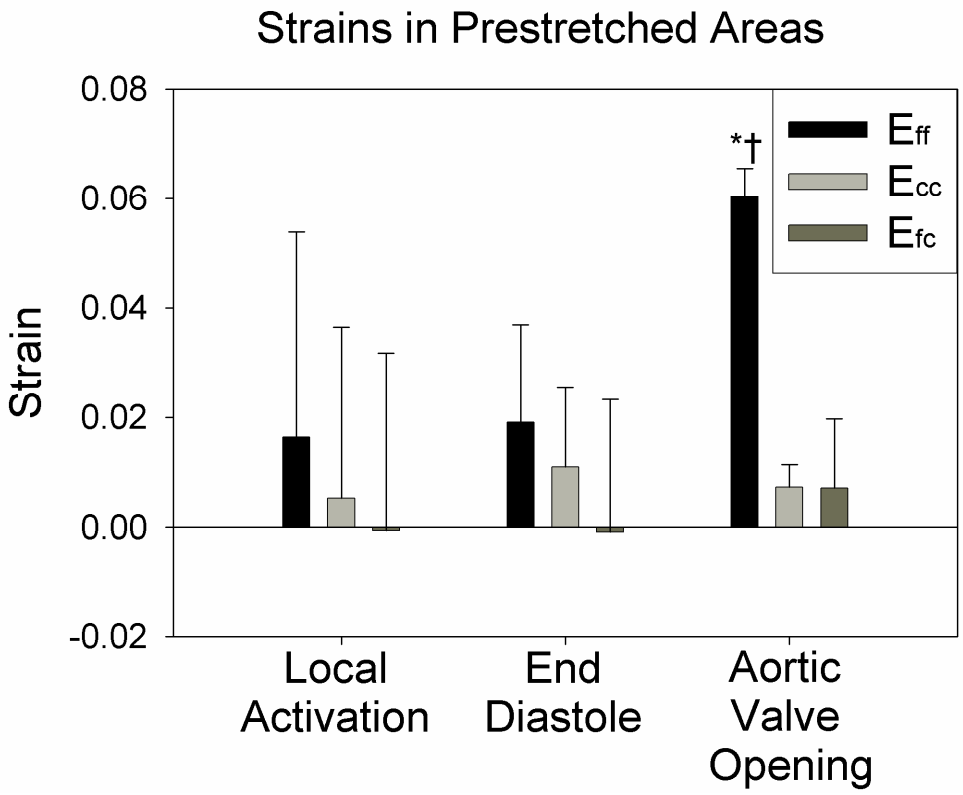

Figure 3.6: Average Values of Strain Components in Prestretched Areas
Fiber strain (E_{ff}) at aortic valve opening was significantly larger than at the time of local activation or end diastole; crossfiber strain (E_{cc}) and fiber-crossfiber shear strain (E_{fc}) were not significantly different * $P < 0.05$ vs. Local Activation, † $P < 0.05$ vs. End Diastole.

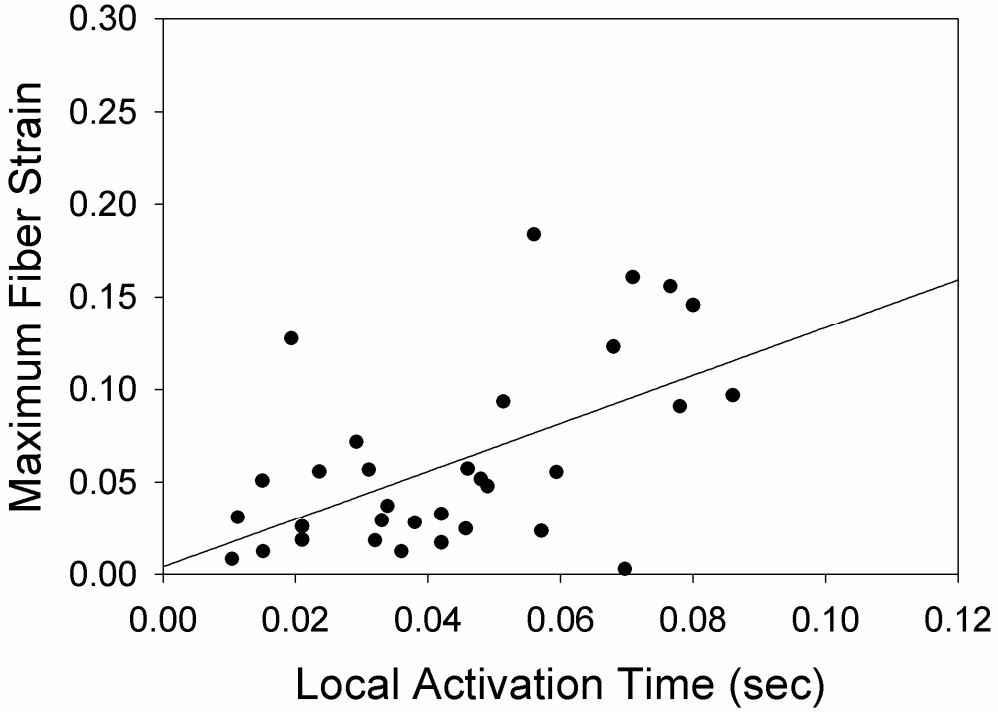

Figure 3.7: Magnitude of Fiber Strain vs. Activation Time
Maximum regional fiber strain versus the local activation time of that region. All regions with a quantifiable electrogram were used, for a total of 33 points.

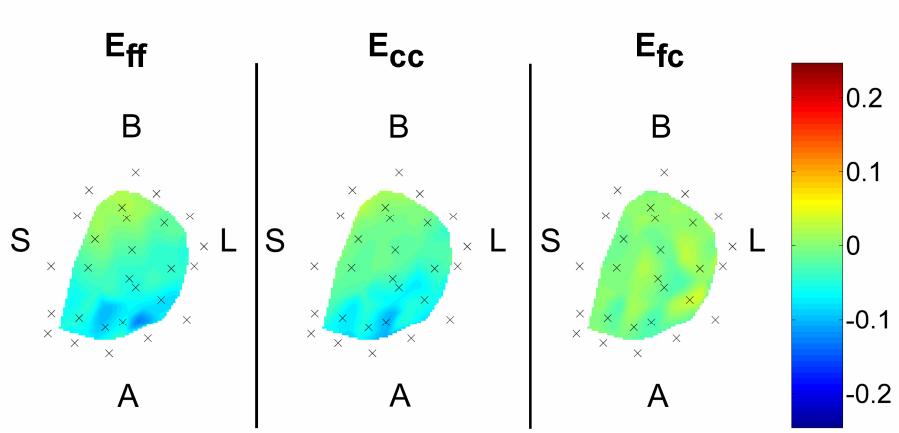

Figure 3.8: Changes in Fiber Length with Activation Sequence
Example of aortic valve opening strains in fiber coordinates. (E_{ff}) Fiber component, (E_{cc}) Cross-fiber component, (E_{fc}) Fiber/Cross-fiber shear component. All strain components are homogeneous and small.

To determine if prestretch provides a functional advantage, we next addressed the question of whether fiber length at the time of aortic valve opening in prestretched areas was longer than at aortic valve opening during atrial activation. The bead configuration at the time of aortic valve opening during atrial activation is taken as the reference configuration, and the bead configuration at the time of aortic valve opening in ventricular pacing as the deformed configuration. From the example in figure 8 there are negative aortic valve opening strains near the apex and slightly positive strains towards the base. As shown in figure 3.9A, on average there were no significant aortic valve opening strains with a short A-V delay. This is likely due to a shorter initial fiber length at the time of ventricular stimulation compared to atrial-paced end diastole (mean fiber strain = -0.058 ± 0.034, $p < 0.05$). This suggests that in this preparation prestretched tissue provided no functional advantage relative to atrial pacing; however, fiber ejection strain was significantly increased as shown in figure 3.9B. Overall, stroke volume was reduced by ventricular pacing, suggesting a net decrease in ejection strain over the entire left ventricle. In addition, there was a relationship between magnitude of peak prestretch (PP) and ejection strain (EJS): $EJS = -0.6654 * PP - 0.0541$ ($R^2 = 0.499$, $p < 0.001$). In light of the insignificant aortic valve opening strains, this functional improvement of prestretched tissue may instead be related to the 15.4% decrease in average systolic pressure observed in this preparation.

Transmural Arrays

A second set of animals with transmural arrays was used to compare the pattern of three-dimensional deformation during prestretch to that of passive inflation. Strains were calculated at 2% ('epi'), 41% ('mid'), and 79% ('endo') of the wall depth from epicardium in order to compare with literature values. The magnitudes of the cardiac strain components at peak prestretch are listed in Table 2. Note the limited transmural variation. Peak prestretch occurred at 35.8 ± 37.5 mmHg, at a greater pressure (on average) than would occur as a result of a physiological passive inflation.

In order to assess the degree of asynchrony, we calculated aortic valve opening strains between early-activated and late-activated tissue. Because simultaneous measurements at early- and late-activated areas were not possible, the pacing stimulus was moved to vary the activation time of the measurement site. Pacing at the epicardium over the bead array resulted in early activation, while the normal posterior wall pacing location resulted in late activation. At the same depth as the midwall array, the fiber component of aortic valve opening strain was 0.080 ± 0.023 (wall depth = 64%, $p < 0.05$), suggesting that the fibers in the late activated region are indeed longer than their early activated counterparts.

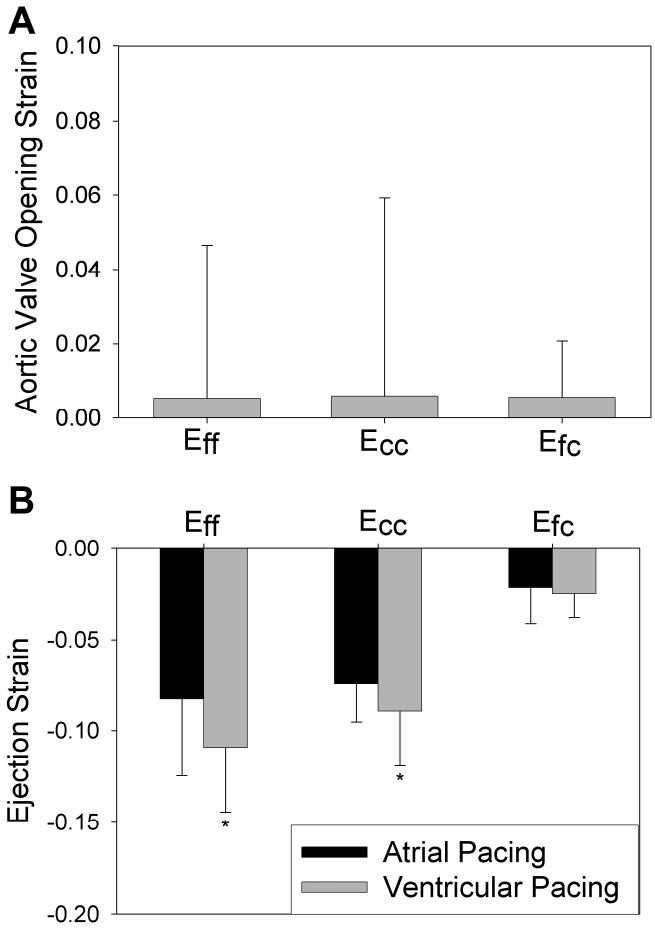

Figure 3.9: Changes in Ejection Strain with Activation Sequence
A: Aortic valve opening strains in prestretched regions, average of 5 animals. A value of zero indicates no change between atrial and ventricular pacing. None of the strain components were significantly different at the time of aortic valve opening during ventricular pacing, as compared to atrial pacing. Statistical comparisons were made with a one-sample t-test against a hypothesized mean of zero. B: Ejection strains, average of 5 animals. Fiber strain (E_{ff}) and crossfiber strain (E_{cc}) are enhanced by ventricular pacing. Fiber-crossfiber shear strain (E_{fc}) was not significantly different. * $P < 0.05$.

Table 3.2: Cardiac Strains at Peak Prestretch
Strains during prestretch are of lesser magnitude and exhibit less transmural variation than during passive inflation. E11: circumferential strain; E22: longitudinal strain; E33: radial strain; E12: circumferential-longitudinal shear strain; E23: longitudinal-radial shear strain; E13: circumferential-radial shear strain

	Epi	Mid	Endo
E11	0.051± 0.019	0.077±0.024	0.079±0.037
E22	0.029±0.002	0.040±0.013	0.058±0.040
E33	-0.071±0.034	-0.069±0.026	-0.065±0.028
E12	-0.007±0.022	0.016±0.016	0.015±0.008
E23	-0.012±0.028	-0.010±0.011	-0.007±0.014
E13	-0.035±0.011	-0.016±0.009	-0.002±0.031

3.5. Discussion

In this study, the mechanics of late activated myocardium during ventricular pacing were investigated in an *in situ* canine heart preparation. Electrical activation and mechanics were measured in the late-activated region by use of midwall material markers that covered approximately 20 - 25% of the LV (N = 5) and transmural arrays (N = 5). The results show that prestretch mostly occurs after time of end diastolic pressure and differs from passive inflation. At short A-V delays, fiber length in prestretched regions was longer than early-activated regions, but not compared to atrial pacing, suggesting an overall decrease in preload which is consistent with decrease in stroke volume. Ejection strain was increased, however, potentially as a secondary result of diminished pressure generation caused by the dyskinetic contraction.

Badke et al. were among the first to recognize prestretch, which we and others have defined as tissue lengthening occurring prior to aortic valve opening (2). Since then it has been studied by several investigators using various techniques such as epicardial video markers (6, 16), MRI (17, 20), radionuclide angiography(3, 4), tissue Doppler imaging (11), and finite element modeling (9). The hemodynamic effects of ventricular activation are well known and the results in this study are similar to many early publications. LV systolic pressure was reduced, within the range of 12 – 25% found in most previous studies (2, 6, 14). A few studies showed no change in systolic pressure, but this was probably due to unmatched heart rate (15) or differences in anesthesia (16). LVEDP was reduced in at least one study (14), but LVEDP was unchanged in most studies of AV sequential pacing, when there is a component of atrial filling (2, 6, 15).

These studies also found a decrease in stroke volume of between 13% and 23%, consistent with the 18% decrease seen here. In the current study, dP/dt_{max} was reduced by 18%, also similar to these other studies (8 – 27%).

The time course of prestretch has been reported, but with lower temporal resolution (15, 16, 21), has not been expressed in terms of fiber direction (20, 21), and has not been described relative to phases in the cardiac cycle. Because activation is asynchronous, the pattern of regional contraction relative to LV pressure generation is altered. During normal activation, the majority of the ventricle is activated within 20-30 ms of end diastole. With ventricular pacing, however, some areas are activated much earlier than this (during late diastole) and some areas are activated much later (during isovolumic contraction). Compared to other studies of ventricular activation, the delay to reach the latest activated region in the present study was comparable, on the order of 100 ms (15, 16). In this study we compared the magnitude of stretch at the time of activation, the end of diastole, and the time of aortic valve opening. An MRI study by Wyman et al. (20) showed that the prestretch begins in late diastole and continues through the isovolumic contraction phase, reaching magnitudes of as much as 20%. However, the time of end diastole was not available. Also, midwall circumferential strains were used, which may have a different time course than fiber strain, with significant regional variation. In studies with epicardial markers (15, 16), approximately 10% fiber stretch was seen during isovolumic contraction, the lower number most likely reflecting that late diastole was not included in those results. Our results clearly show that very little prestretch occurs before the time of ventricular end diastole, and perhaps more

importantly when the tissue is lengthening it is also electrically depolarized and presumably capable of generating force.

From the current data it is not possible to define the nature of the forces lengthening the prestretched tissue. However, it seems likely that the high intracavitary pressures during isovolumic systole play a major role in lengthening activated tissue. To determine if the three-dimensional deformation of prestretched tissues differs from passive inflation, we compared our transmural results to those of Omens et al (12). In those experiments, isolated, arrested canine hearts were passively inflated to a normalized volume change of 0.20 ml/g, corresponding to a pressure change from 0-10 mmHg. In the current experiments, the pressure changed from 3.9 mmHg (at stimulus) to 35.8 mmHg (at peak prestretch). Despite this larger pressure change, 6 of 9 normal cardiac strain components were significantly smaller in magnitude, as shown in Figure 3.10. The transmural gradients were also reduced in prestretch. For example, the gradient of radial strain (E33) was not significantly different from zero. Moreover, the transmural gradient during passive inflation (-0.088 % depth^{-1}) is greater than two standard deviations more than during prestretch (-0.010 ± 0.033 % depth^{-1}), further emphasizing the difference in the mode of deformation. The reduced transmural gradients suggest that the activation sequence in these late-activated regions may progress transmurally from endocardium to epicardium, beginning the stiffening of these endocardial cells earlier and preventing them from stretching as much. In summary, the results of this study do not support the

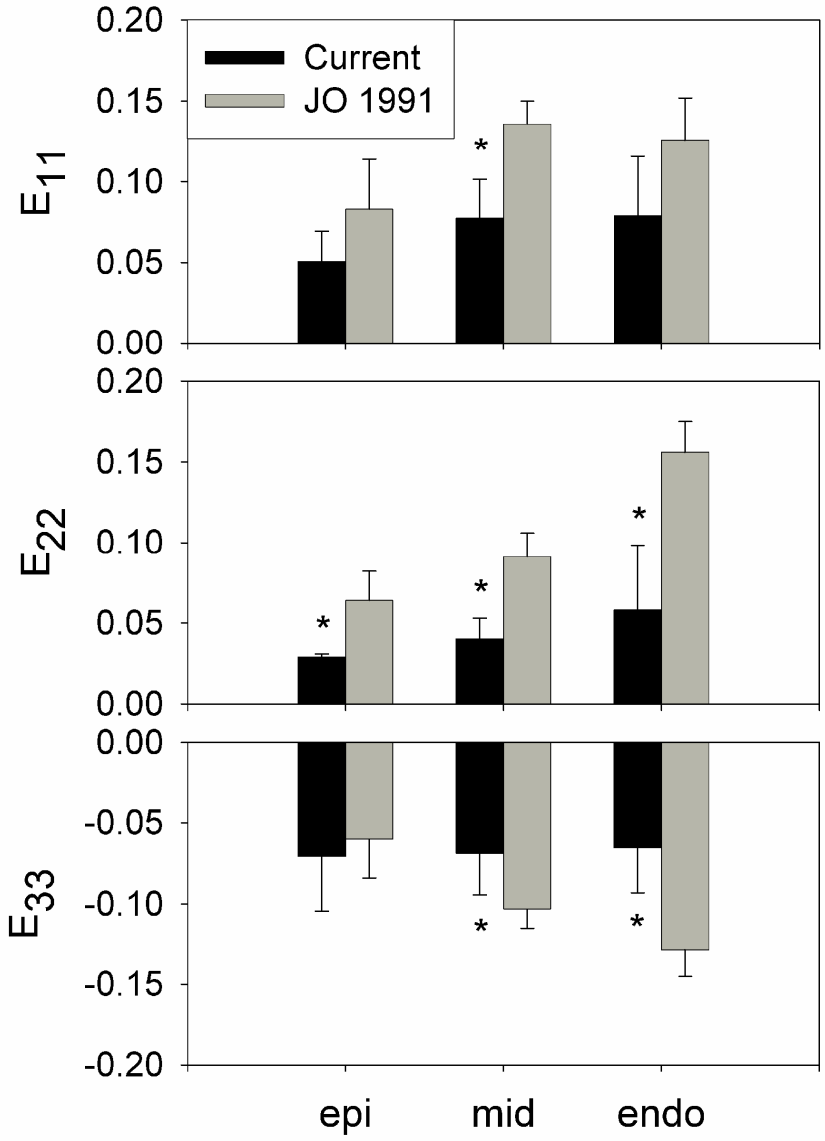

Figure 3.10: Comparison Between Prestretch and Passive Inflation
Cardiac strains during prestretch ("Current") and passive inflation ("JO 1991"). Average pressure changes were from 3.9 to 35.8 mmHg and 0 to 10 mmHg, respectively. Strain magnitudes were reduced relative to passive inflation, and transmural gradients were reduced or eliminated. E11: circumferential strain, E22: longitudinal strain, E33: radial strain. * $P < 0.05$ vs. Passive Inflation at same depth (with Bonferroni correction).

concept that prestretched tissue is passively lengthened in the same manner as diastolic filling of the ventricle.

Another possible mechanism of prestretch is that contracting early-activated areas could directly stretch late activated tissue. First, the stretch is predominately in the fiber direction (figure 3.6), whereas passive filling at this wall depth has a larger crossfiber component (12). Second, as time from the stimulus increases, the force developed by the early activated fibers increases, as well as the total number of force generating fibers. Thus, the overall deformation is likely the result of a combination of intracavitary pressure and fiber connectivity.

In the present study peak lengthening in prestretched areas occurred 44 ms following local depolarization. There was an increased magnitude of prestretch that was roughly proportional to the delay in local activation time. It has been previously shown that the activation time correlates with the local ejection strain (9) and mechanical activation time (20), but to our knowledge no one has shown the relationship with magnitude of stretch.

The question of whether ejection strain is augmented in late activated areas has received substantial attention. Badke et al.(2) showed that late-activated segments had unchanged or depressed ejection strain, but larger “actual” shortening (total shortening regardless of phase in the cardiac cycle) when there was no contribution of atrial contraction to filling. Prinzen et al.(16), using AV sequential pacing with a 30 ms delay, showed that ejection strain was larger in the late-activated region than the same areas during atrial pacing. However, the 150% increase over atrial pacing is larger than the 32% increase seen in the present study, likely due to the hemodynamic differences

between the two studies discussed above. Despite these differences in magnitude, an increase was seen in both studies. The mechanism of this increase is unknown. However, several authors have suggested there is a length-dependent activation effect due to increased fiber/sarcomere length in the prestretched areas (9, 15, 17).

To investigate this possibility we compared the change in fiber length at aortic valve opening in prestretched areas to the same areas during atrial activation. At an A-V delay of 35 ms, there was no statistically significant change in fiber length (mean fiber aortic valve opening strain = 0.005). It therefore seems unlikely that length-dependent activation is responsible for the enhanced ejection strain in this preparation. In fact, of the four well known regulators of ventricular performance (heart rate, preload, inotropic state, and afterload) only afterload changed significantly. Although average systolic pressure is not a true measurement of local tissue afterload, this may be the best explanation for the observed increase in ejection strain.

Although fiber length at aortic valve opening was not different from atrial pacing, there was still a difference in fiber length between early and late activated regions. This reflects the heterogeneous distribution of stretch in the ventricle. Coupled with the aortic valve opening strain results this shows a net reduction in overall LV preload, which is at least partially responsible for diminished hemodynamic function.

Aortic valve opening strain, the change in muscle fiber length from atrial to ventricular pacing in prestretched regions, was not significantly different from zero. This can be explained by the pre-excitation that occurs at short A-V delays. As a result, at the time of ventricular stimulation the fibers were shorter than at atrial-paced end diastole. We have anecdotal evidence in one dog with complete AV block that shows that aortic

valve opening strain increases with A-V delay, to a maximum of 100 ms. Despite this, the ejection strain was unchanged over this range of A-V delays. This likely reflects the balance between preload and afterload, both of which increase with A-V delay.

Study Limitations

The present study was designed to investigate the magnitude and timing of stretch in the late-activated region of the ventricular paced canine LV. The approach has several limitations. First, beads were plunged into the myocardium with the use of a trocar, which likely causes some local injury. However, the overall deformation of the array region is unlikely to be affected by small areas of injury. No evidence of ischemia was seen in the ECG in any of the animals. Second, the interpretation of these data was made with the assumption that all the beads formed a surface at a fixed transmural depth, while in reality there was a small variation in bead depth. Third, though the equations to calculate strain are exact, there are errors involved in bead digitization (the resolution of the radiographic system is ~0.02 mm), as well as the three-dimensional reconstruction from the two-dimensional images. Fourth, the measured fiber orientations were registered with the strain data based on bead locations, which may have produced some inaccuracies. Averaging of the 3 closest fiber angle measurements presumably reduced these errors. Additionally, changes in segment length along the fiber direction were used for all fiber length comparisons rather than any direct measure of fiber or sarcomere length. Lastly, with the current technique simultaneous strain measurements of the entire ventricle are not possible. Therefore it is possible that the location of maximum prestretch is not encompassed by the array.

In this study we used a fixed A-V delay of 35 ms. Because the experiments were performed in the presence of a functioning AV node, a relatively low A-V delay was chosen to insure that the activation wave front spread from the pacing site and activated the ventricles exclusive of native conduction. In a similar model, Faris et al. showed that such fusion of activation sources did not occur at A-V delays below 60 ms (7). However, this choice of delay likely results in sub-optimal filling and a reduction of end diastolic volume compared to atrial pacing (10).

3.6. Conclusions

In conclusion, during left ventricular pacing the mechanics of the late-activated tissue was studied using midwall and transmural marker arrays in the canine left ventricle. In late activated tissue the majority of prestretch was found to occur during isovolumic systole, probably due to a combination of intracavitary pressure as well as series and parallel force generation by early activated fibers. The deformation was different from passive inflation, reflecting the lengthening of already electrically activated tissue that resulted in reduced transmural gradients of strain. At short A-V delays muscle fiber length in prestretched areas was unchanged compared to atrial activation while fiber length in early activated areas was reduced. Although ejection shortening in late activated areas was increased compared to atrial activation likely due to a decrease in afterload, overall ejection shortening (as reflected by stroke volume) was reduced due presumably to dyskensis and to an overall reduction in muscle length.

3.7. Acknowledgments

We thank Aundrea Graves, Katrina Go, and Leonard Lee for surgical assistance. This research was supported by National Heart, Lung, and Blood Institute Grant HL-32583 (Omens) and HL-43617 (Covell). Chapter 3, in full, is a reprint of the material as it appears in "Asynchrony of Ventricular Activation Affects Magnitude and Timing of Fiber Stretch in Late-Activated Regions of the Canine Heart" by Benjamin A. Coppola, Andrew D. McCulloch, James W. Covell, and Jeffrey H. Omens in the *American Journal of Physiology: Heart and Circulatory Physiology* 293: H754-H761, 2007. The dissertation author was the primary investigator and author of this paper.

3.8. References

1. **Ashikaga H, Criscione JC, Omens JH, Covell JW, and Ingels NB, Jr.** Transmural left ventricular mechanics underlying torsional recoil during relaxation. *Am J Physiol Heart Circ Physiol* 286: H640-647, 2004.

2. **Badke FR, Boinay P, and Covell JW.** Effects of ventricular pacing on regional left ventricular performance in the dog. *Am J Physiol Heart Circ Physiol* 238: H858-867, 1980.

3. **Botvinick E, Dunn R, Frais M, O'Connell W, Shosa D, Herfkens R, and Scheinman M.** The phase image: its relationship to patterns of contraction and conduction. *Circulation* 65: 551-560, 1982.

4. **Boucher CA, Pohost GM, Okada RD, Levine FH, Strauss HW, and Harthorne JW.** Effect of ventricular pacing on left ventricular function assessed by radionuclide angiography. *Am Heart J* 106: 1105-1111, 1983.

5. **Costa KD, Takayama Y, McCulloch AD, and Covell JW.** Laminar fiber architecture and three-dimensional systolic mechanics in canine ventricular myocardium. *Am J Physiol* 276: H595-607, 1999.

6. **Delhaas T, Arts T, Prinzen FW, and Reneman RS.** Relation between regional electrical activation time and subepicardial fiber strain in the canine left ventricle. *Pflugers Arch* 423: 78-87, 1993.

7. **Faris OP, Evans FJ, Dick AJ, Raman VK, Ennis DB, Kass DA, and McVeigh ER.** Endocardial versus epicardial electrical synchrony during LV free-wall pacing. *Am J Physiol Heart Circ Physiol* 285: H1864-1870, 2003.

8. **Fung YC.** *A First Course In Continuum Mechanics*: Prentice Hall, 1993.

9. **Kerckhoffs RCP, Faris OP, Bovendeerd PHM, Prinzen FW, Smits K, McVeigh ER, and Arts T.** Electromechanics of paced left ventricle simulated by straightforward mathematical model: comparison with experiments. *Am J Physiol Heart Circ Physiol* 289: H1889-1897, 2005.

10. **Meisner JS, McQueen DM, Ishida Y, Vetter HO, Bortolotti U, Strom JA, Frater RW, Peskin CS, and Yellin EL.** Effects of timing of atrial systole on LV filling and mitral valve closure: computer and dog studies. *Am J Physiol Heart Circ Physiol* 249: H604-619, 1985.

11. **Nagai H, Takata S, Sakagami S, Furusho H, Takamura M, Yuasa T, and Kobayashi K.** Two-dimensional guided M-mode color tissue Doppler

echocardiography in artificial preexcitation models. *J Am Soc Echocardiogr* 12: 582-589, 1999.

12. **Omens JH and Covell JW.** Transmural distribution of myocardial tissue growth induced by volume-overload hypertrophy in the dog. *Circulation* 84: 1235-1245, 1991.

13. **Omens JH, MacKenna DA, and McCulloch AD.** Measurement of strain and analysis of stress in resting rat left ventricular myocardium. *J Biomech* 26: 665-676, 1993.

14. **Park R, Little W, and O'Rourke R.** Effect of alteration of left ventricular activation sequence on the left ventricular end-systolic pressure-volume relation in closed-chest dogs. *Circ Res* 57: 706-717, 1985.

15. **Prinzen FW, Augustijn CH, Allessie MA, Arts T, Delhaas T, and Reneman RS.** The time sequence of electrical and mechanical activation during spontaneous beating and ectopic stimulation. *Eur Heart J* 13: 535-543, 1992.

16. **Prinzen FW, Augustijn CH, Arts T, Allessie MA, and Reneman RS.** Redistribution of myocardial fiber strain and blood flow by asynchronous activation. *Am J Physiol Heart Circ Physiol* 259: H300-308, 1990.

17. **Prinzen FW, Hunter WC, Wyman BT, and McVeigh ER.** Mapping of regional myocardial strain and work during ventricular pacing: experimental study using magnetic resonance imaging tagging. *Journal of the American College of Cardiology* 33: 1735-1742, 1999.

18. **Streeter DD, Jr., Spotnitz HM, Patel DP, Ross J, Jr., and Sonnenblick EH.** Fiber Orientation in the Canine Left Ventricle during Diastole and Systole. *Circ Res* 24: 339-347, 1969.

19. **Villarreal FJ, Waldman LK, and Lew WY.** Technique for measuring regional two-dimensional finite strains in canine left ventricle. *Circ Res* 62: 711-721, 1988.

20. **Wyman BT, Hunter WC, Prinzen FW, Faris OP, and McVeigh ER.** Effects of single- and biventricular pacing on temporal and spatial dynamics of ventricular contraction. *Am J Physiol Heart Circ Physiol* 282: H372-379, 2002.

21. **Wyman BT, Hunter WC, Prinzen FW, and McVeigh ER.** Mapping propagation of mechanical activation in the paced heart with MRI tagging. *Am J Physiol Heart Circ Physiol* 276: H881-891, 1999.

4. Role of Myocardial Sheets in Ventricular Wall Thickening

4.1. Abstract

It is well known that systolic wall thickening in the inner half of the left ventricular (LV) wall is of greater magnitude than predicted by myofiber contraction alone. Previous studies have related the deformation of the LV wall to the orientation of the laminar architecture. Using this method, wall thickening (assessed as radial strain) can be interpreted as the sum of contributions due to extension, thickening, and shearing of the laminar sheets. We hypothesized that the thickening mechanics of the ventricular wall are determined by the structural organization of the underlying tissue, and may not be influenced by factors such as loading and activation sequence. To test this hypothesis, we calculated finite strains from biplane cineradiography of transmural markers implanted in apical (n = 22) and basal (n = 12) regions of the canine anterior LV free wall. Strains were referred to three-dimensional laminar microstructural axes measured by histology. The results indicate that sheet angle is of opposite sign in the apical and basal regions, but absolute value differs only in the subepicardium. During systole, shearing and extension of the laminae contribute the most to wall thickening, accounting for >90% (transmural average) at both apex and base. These two types of deformation are also most prominent during diastolic inflation. Increasing afterload has no effect on the pattern of systolic wall thickening, nor does reversing transmural activation sequence. The pattern of wall thickening appears to be a function of the orientation of the laminar sheets, which vary regionally and transmurally. Thus, acute interventions do not appear to alter the contributions of the laminae to wall thickening, providing further evidence

that the structural architecture of the ventricular wall is the dominant factor for its regional mechanical function.

4.2. Introduction

Systolic wall thickening in the left ventricle has long been considered an important functional measure because of its significant contribution to stroke volume (9, 12) and its sensitivity to local changes in perfusion (10) and metabolism (21). The observed amount and pattern of wall thickening cannot be explained by cell thickening alone; fiber shortening is similar across the wall in dog (3, 29), sheep (6), and human (19, 22), yet the radial strain increases significantly from epicardium to endocardium in these and other studies (11, 23). In addition, the magnetic resonance imaging (MRI) studies of Rademakers et al. showed that radial strain is correlated with crossfiber rather than fiber shortening, and attributed this to tissue tethering between the endocardium and epicardium (22). This suggests either a change in individual fibers during contraction, toward a more oval cross-section, or a rearrangement of a bundle of fibers as the wall thickens. There are a larger number of fibers across the wall during diastole than during systole (25), providing some evidence for the existence and function of fiber bundles. Additionally, there is transverse shear in the endocardium of sufficient magnitude and correct sign to account for radial strain in the endocardium, and these shearing planes are closely aligned with the myocardial laminae (18).

Examination of the macrostructure of the heart reveals cleavage planes in the circumferential-radial and longitudinal-radial planes (25). Electron microscopy further reveals that these cleavage planes arise from the organization of myofibers into laminar

sheets, approximately 4 to 8 cells thick (18). These laminae exhibit variation in transmural and regional orientation (18). Slippage between laminae may result in transverse shearing and thus provide a mechanism for additional wall thickening. Costa and co-workers (7) explored this hypothesis by expressing radial strain as the sum of the thickening due to each of three types of sheet motion: extension, thickening, and shearing. Using this same approach, Takayama et al. looked at the effect of changes in load during systole and diastole, and found the contributions to be qualitatively unchanged (27). There are changes in the deformation of the sheets during ventricular epicardial pacing relative to normal activation (3), but the relative contributions to wall thickening are unchanged.

In this study, we test the hypothesis that the thickening pattern of the ventricular wall occurs in a specific fashion based on the structural organization of the underlying tissue. To test this hypothesis, we implanted transmural bead arrays into the left ventricle of open-chest dogs and imaged them with biplane cineradiography. Finite strains were computed and referred to a histologically measured fiber-sheet coordinate system. We studied the contributions of sheet deformation to radial strain during systole and diastole, with different loading conditions, and during ventricular pacing. We conclude that the contributions of the myocardial sheet deformations to ventricular wall thickening are a fixed property of the tissue that does not appear to fluctuate acutely. It appears as though the structural architecture of the ventricular wall is the dominant factor for its regional mechanical function.

4.3. Materials and Methods

All animal studies were performed according to the National Institutes of Health *Guide for the Care and Use of Laboratory Animals*. All protocols were approved by the Animal Subjects Committee of the University of California, San Diego, which is accredited by the American Association for Accreditation of Laboratory Animal Care.

The data described herein comes from four different sets of animal experiments performed in this laboratory (Table 1) assembled here to examine different experimental conditions. Three of these sets (groups A,B,C) have been previously published in some form (2, 3, 27); the raw data has been re-analyzed to fit the scope of this paper. The fourth set (group D) is original data with ventricular pacing. Several aspects of the experiments are identical, and will be discussed first.

Common Preparation

Adult mongrel dogs (19–27 kg, n = 22) were anesthetized with intravenous propofol (6 mg/kg), intubated, and mechanically ventilated with isoflurane (0.5–2.5%), nitrous oxide (2 l/min), and medical oxygen (2 l/min) to maintain a surgical plane of anesthesia. The heart was exposed via a median sternotomy and a left thoracotomy at the fourth intercostal space, and then placed in a pericardial cradle. An 8-Fr pigtail micromanometer catheter (Millar Instruments, Houston, TX) was inserted through a 9-Fr arterial introducer placed in the left femoral artery, and the catheter tip was advanced into the LV. LV pressure was monitored with the pigtail micromanometer catheter, and the pressure was matched with that recorded from the side holes of the same catheter that was connected to a fluid-filled transducer. Columns of four to six gold beads (0.8 mm

diameter) were placed from the epicardial surface with the use of a trocar (7). The apical marker implantation site for the set of three columns was selected approximately one-third of the distance from apex to base along the LV long axis in the anterior wall. After marker implantation, larger (2.0 mm diameter) lead beads were sewn to the epicardial surface above each column, as well as at the apex of the LV (apex bead), and at the bifurcation of the left main coronary artery (base bead). These epicardial markers were used to define a local set of circumferential, longitudinal, and radial cardiac coordinate axes $\{X_1, X_2, X_3\}$ at each site, as previously described (28).

Each animal was positioned in a biplane radiography system, and synchronous biplane cineradiographic images (125 frames/s) of the bead markers were digitally acquired with mechanical ventilation suspended at end expiration. After the functional data acquisition was complete, the animals were euthanized with pentobarbital sodium and the heart arrested and perfusion fixed with 2.5% buffered gluteraldehyde at the end-diastolic pressure measured during the atrial paced run in the study, as described previously (1). The fixed, silastic-filled heart was skewered from the apical dimple to the mitral aspect of the aortic valve, to define the LV long axis (26). To avoid the distortional effects of dehydration and embedding, histological measurements were obtained using freshly fixed heart tissue (1, 7). In the transmural block of tissue within the implanted bead set, the mean fiber (α) and sheet angles (β) were determined from epicardium to endocardium using the methods of Costa(7) or Ashikaga (1).

Differences between Preparations

In two sets of animals (groups A & C) a second set of three columns was implanted at the basal site, approximately two-thirds of the distance from the apex to the base. Fig. 4.1A depicts this arrangement. In addition, an implantable micromanometer (Konigsberg Instruments; Pasadena, CA) replaced the Millar catheter in these groups. In group C, a snare was placed around the inferior vena cava (IVC) for the preload studies. Group A differed the most - the chest was closed and the animal recovered for 7-10 days. Functional data was acquired with the animal lightly sedated and hanging in a sling as described by Ashikaga and co-workers (2). We compared the mean sheet angles of Group A with Groups B-D and concluded that they were not significantly different. The relative contributions to radial strain were also unchanged. As a result, we chose to combine the data sets.

Experimental Protocol

All animals (groups A-D) were included as control data for the analysis of end-systolic function. In total, there were 22 animals with apical bead arrays and 12 with basal bead arrays. All other experimental procedures involved only subsets of animals.

Table 4.1: Description of Data Sources
The four sources (A-D) of the data in this paper. Groups A & B utilized only the control data from these experiments. The largest complete sets of data are end-systolic control data at the apex (n=22) and base (n=12).

Group	Source	Intervention	Site	Sample Size
A	Ashikaga et al. 2004 #1	Control only	Apex/Base	6
B	Ashikaga et al. 2004 #2	Control only	Apex	5
C	Takayama et al. 2002	Preload & Afterload	Apex/Base	6
D	Original data	Endo- and Epicardial Pacing	Apex	5

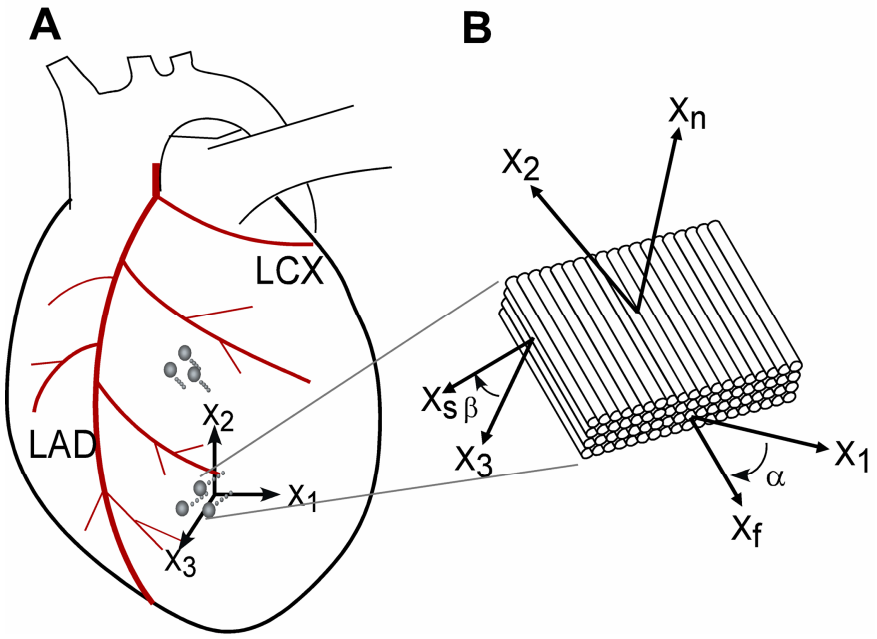

Figure 4.1: Locations of Deformation Measurements
A: schematic representation of the left ventricle with bead arrays at the apex and base (1/3 and 2/3 of the distance from apex and base, respectively). X_1, circumferential axis; X_2, longitudinal axis; X_3, radial axis; LAD, left anterior descending; LCX, left circumflex. B: schematic representation of local fiber-sheet axes. Fiber angle (α) was measured in the X_1-X_2 plane at each wall depth with reference to positive X_1. Sheet angle (β) was measured in the plane perpendicular to the fiber angle at each wall depth with reference to positive X_3. X_f, fiber axis, X_s, sheet axis, X_n, axis oriented normal to the sheet plane.

Preload (group C)

Apical (n=6) and basal (n=6) bead arrays. The preload studies are described in Takayama et al (27). In brief, dextran was rapidly infused into the heart to raise end-diastolic pressure (EDP) to ~20 mmHg. The IVC was then abruptly occluded. Cineradiographic and hemodynamic data were acquired at levels of high EDP (17-22 mmHg), medium EDP (12-14 mmHg), low EDP (7-9 mmHg), and a reference state (3-4 mmHg).

Afterload (group C)

Apical (n=6) and basal (n=6) bead arrays. The afterload studies are also described in Takamaya et al (27). Briefly, methoxamine (5 to 10 $\mu g \cdot kg^{-1} \cdot min^{-1}$) was infused to elevate LV end-systolic pressure (ESP) by at least 35 mmHg. During methoxamine infusion, dextran was transfused as needed to elevate EDP or IVC occlusion as needed to reduce EDP was used to ensure that the EDP was matched with the initial value in each animal (within 1 mmHg). Biplane cineradiography and hemodynamic data were then recorded.

Pacing (group D)

Apical bead array only (n = 5). Atrial pacing was performed by stimulating LA electrodes, and LV pacing was performed by stimulating both LA and LV electrodes (LA-LV delay = 35 ms), via a square-wave constant-voltage electronic stimulator (model SD9; Grass Instruments, Quincy, MA) at a frequency 20% above baseline heart rate to suppress native sinus rhythm. Stimulation parameters (voltage 10% above threshold,

duration 8 ms, and frequency) were kept constant in each animal. Each animal was positioned in a biplane radiography system, and synchronous biplane cineradiographic images (125 frames/sec) of the bead markers were digitally acquired with mechanical ventilation suspended at end expiration. Recordings were obtained during atrial pacing and then following approximately 2 to 5 minutes of endo- or epicardial pacing (to achieve a steady hemodynamic state). Atrial pacing was continued between ventricular pacing runs.

Finite strain analysis

The following methods were common to all animals. Biplane cineradiographic images (125 frames/s) from the X-ray image intensifiers were spherically corrected, and the 3-D coordinates of the bead markers were reconstructed in each frame as described by Ashikaga et al (1). A continuous polynomial position field that mapped the beads in the undeformed reference configuration to those in the deformed configuration was determined (1, 17). The order of the polynomial is at most linear in the circumferential and longitudinal directions, and the maximum order in the radial direction is typically quadratic. With this continuous polynomial mapping from reference position to current position, differentiation with respect to reference position gives the deformation gradient tensor, **F**, which depends on position. The Lagrangian Green's strain tensor was then calculated as $0.5(\mathbf{F}^T\mathbf{F} - \mathbf{I})$ at various values of reference wall depth, where $\mathbf{F}^T$ is the transpose of **F** and **I** is the identity matrix.

Six independent finite strains [circumferential (E_{11}), longitudinal (E_{22}), and radial (E_{33}) strains, circumferential-longitudinal shear (E_{12}), longitudinal-radial shear (E_{23}), and

circumferential-radial sheer (E_{13})] were computed in the local cardiac coordinate system of circumferential, longitudinal, and radial axes (X_1, X_2, X_3), which were subsequently used to compute another set of six finite strains [fiber strain (E_{ff}), sheet strain (E_{ss}), strain normal to the sheet plane (E_{nn}), fiber-sheet shear (E_{fs}), sheet shear (E_{sn}), and fiber-normal shear (E_{fn})] in the local fiber-sheet coordinate system (X_f, X_s, X_n) through an orthogonal transformation to convert the strain tensor using the values of α and β at each depth (7). The local fiber-sheet coordinate system defines the myofiber axis (X_f), the sheet axis (X_s) that lies within the sheet plane and is perpendicular to X_f, and the orthogonal X_n axis oriented normal to the sheet plane, as shown in Fig. 4.1B.

Finite strains were calculated in fiber-sheet coordinates with local activation as the reference state. During atrial pacing, this coincided with the peak of the ECG R wave. In the case of ventricular pacing, the time of local stimulus was used as the reference state. If an aortic flow probe was present, it was used to determine the time of end systole. Otherwise, the pressure at the nadir of the dicrotic notch of the central aortic pressure was used to estimate the time of end systole from the micromanometer tracing. Strains were determined at three wall depths: 20% (sub-epicardium), 50% (midwall), and 80% (sub-endocardium).

Contributions of fiber-sheet strains to Radial Strain

Deformations expressed in the cardiac coordinate system can be related to the laminar architecture as described by Costa and co-workers (7). Because the sheet structure is believed to provide a mechanism for increased wall thickening, we can

rewrite the radial strain in terms of contributions due to sheet motion, as in Equation (4.1).

$$E_{33} = Ess \cdot \cos^2 \beta + Enn \cdot \sin^2 \beta + 2 \cdot Esn \cdot \sin \beta \cdot \cos \beta \qquad (4.1)$$

The terms on the right-hand side of Eq. 1 can be interpreted as contributions due to sheet extension (=E_{ss} $\cos^2\beta$), sheet thickening (=E_{nn} $\sin^2\beta$), and sheet shearing (=$2E_{sn}\cos\beta\sin\beta$) during systolic wall thickening. Illustrations are provided in Fig. 4.2. Conversely, during wall thinning they represent sheet shortening, thinning, and shearing of the opposite sense.

Statistical analysis

Values are means ± SD. Repeated measures analysis of variance (RMANOVA) was used whenever applicable (see RESULTS for details). Tukey's method was used for ANOVA post hoc analysis. Statistical tests were performed with SigmaStat 3.0 (SPSS, Chicago, IL). Statistical significance was accepted at $P < 0.05$.

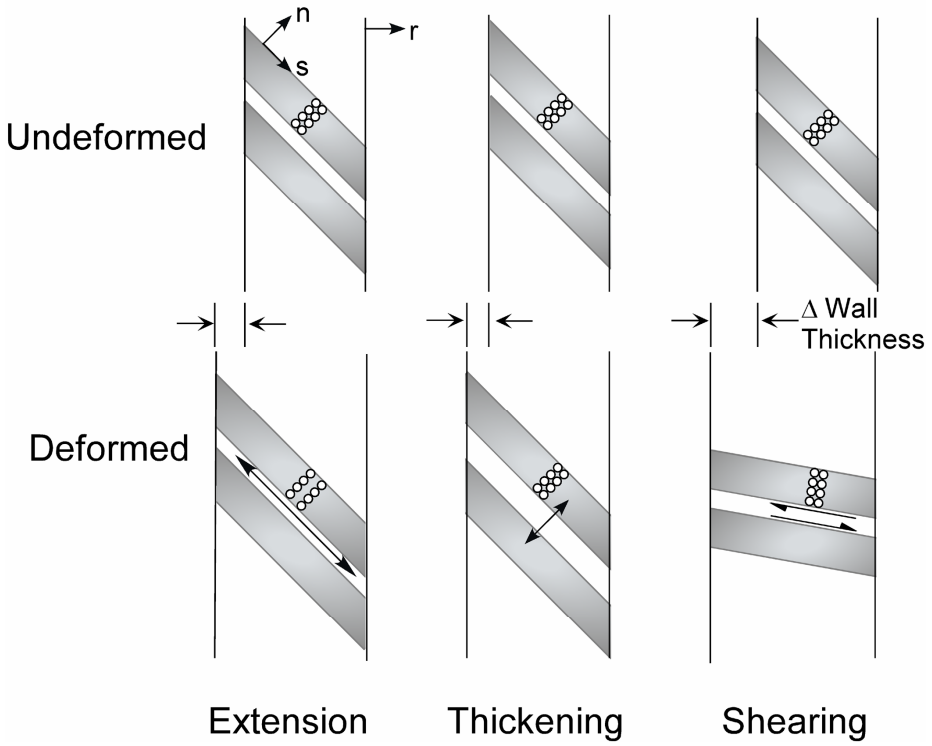

Figure 4.2: Contributions of Different Types of Sheet Deformation to Radial Strain
Schematics show how a portion of the wall can thicken from an undeformed (top) to deformed (bottom) state, based on sheet movement. A: extension of the sheets, B: thickening, or separation of the sheets, C: shearing between sheets. Positive radial strain is indicated by the widening of the vertical bars. Open circles represent myofibers, gray bars represent sheets. r, radial direction; s, sheet direction; n, sheet normal direction.

4.4. Results

Sheet Angles

Fig. 4.3 shows sheet angle (β) as a function of transmural depth for the apical and basal measurement sites (n = 22 and n = 12, respectively). As opposed to the linear transmural distribution of fiber angle, β was a nonlinear function of depth, with the largest absolute value occurring at the midwall (-32.2±17.7º and +25.9º±18.3 at apex and base, respectively). The sign of the sheet angle was negative at all depths at the apex, but only in the sub-epicardium at the base. There was a significant transmural gradient at both sites by one-way RMANOVA. Pairwise comparisons revealed a significant difference between midwall and sub-endocardial sheet angles at the apex, and between sub-epicardial and midwall sheet angles at the base. The interaction between depth and site could not be tested for significance due to unequal sample size. Instead, unpaired t-tests were used to compare the two sites at each depth. By this analysis, the sheet angle at the apex was significantly different from the base at each depth. In the subset of animals that included both apical and basal data (groups A and C), a two-way RMANOVA was performed with depth and region as repeated variables. With this smaller sample size (n = 12), the apex was significantly different from the base but the transmural gradient became insignificant. There was also an effect of region on transmural gradient.

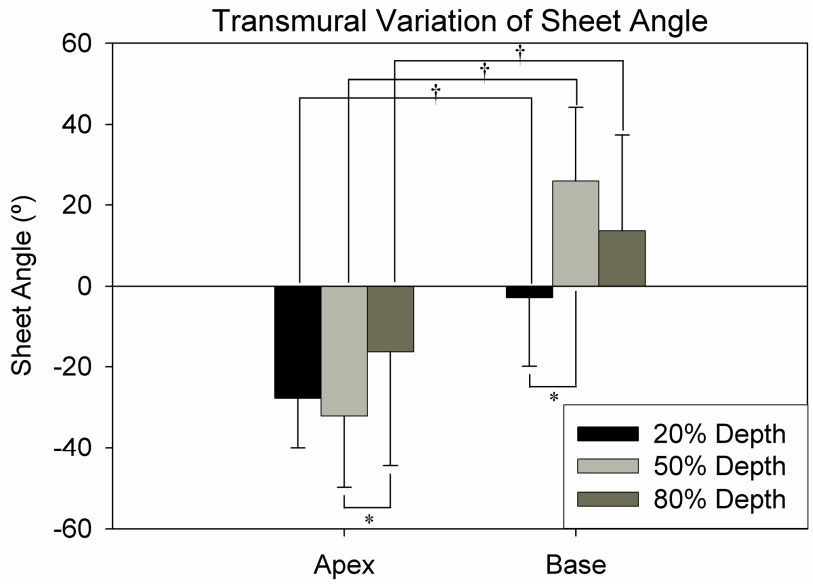

Figure 4.3: Measured Sheet Angles.
Angle = 0º indicates a radial orientation. Sheet angle has opposite sign at apical and basal sites, but similar absolute values. The largest angle occurred at the midwall of each site. There was a significant transmural gradient at each site (RMANOVA, $p<0.05$). * $p < 0.05$ vs. other depths. At each depth, the base was significantly different from the apex. † $p < 0.05$ vs. same depth, by unpaired t-test.

End-Systolic Contributions to Radial Strain

Transmural deformation of the ventricular wall can be expressed in terms of the laminar architecture as described by Equation (4.1). Fig. 4.4 shows how these three terms contribute (as a percentage) to the overall radial strain at end systole. At the apex (n=22), sheet extension and shearing were the dominating components, contributing 47.2 and 46.6% as a transmural average. There was no significant transmural gradient. At the base (n=12), sheet extension and shearing were also dominant, but in addition there was a significant transmural gradient. Pairwise comparisons showed a decrease in sheet shearing and an increase in sheet extension in the sub-epicardium. This shift from shear to extension in part reflects the more radial orientation of sheets in the basal sub-epicardium. Unpaired t-tests showed differences in each component of radial strain between apex and base in the sub-epicardium only. Additionally, in the subset of animals that included both apical and basal data (groups A and C), a two-way RMANOVA was performed with depth and region as repeated variables. This also showed a significant effect of both depth and region, with no significant interaction between the two. These results were not qualitatively different from those presented in Fig. 4.4.

Interventions

The magnitude of radial strain can be altered by external factors. Therefore, it is possible that such interventions would also affect the relative contributions to radial strain. For example, a decrease in afterload increases the magnitude of radial strain. This increase might be accompanied by an increase in shearing of sheets that is greater than the increase of the other components of radial strain, thus changing the relative

proportions. To test this, we examined the effects of diastolic and systolic load, as well as activation sequence.

Diastolic Wall Thinning

In a subset of animals (group C) we examined the relative contributions of sheet motion to radial strain during diastolic inflation as a function of load. Fig. 4.5 illustrates each component of radial strain when inflating hearts from a reference configuration of 3 mmHg to a deformed configuration of 8 mmHg ("Low"), 13 mmHg ("Medium"), or 18 mmHg ("High"). Error bars tend to be bigger at lower loads due to smaller deformation and therefore greater relative noise levels. A three-way RMANOVA (depth, pressure, site) showed only significant differences with depth. None of the contributors of radial strain were significantly altered by diastolic load, at either the apex or base. Similarly, the transmural gradients were not significantly altered by load. There were significant transmural gradients in sheet extension and shearing at medium and high loads (by one-way RMANOVA).

We also compared the contributions during wall thickening vs. wall thinning (i.e. systolic versus diastolic contributions). The contributions of sheet extension and shearing were significantly different between systole and diastole at the apical site, but not at the basal site. The type of deformation did not affect the transmural gradient at either site (two-way RMANOVA).

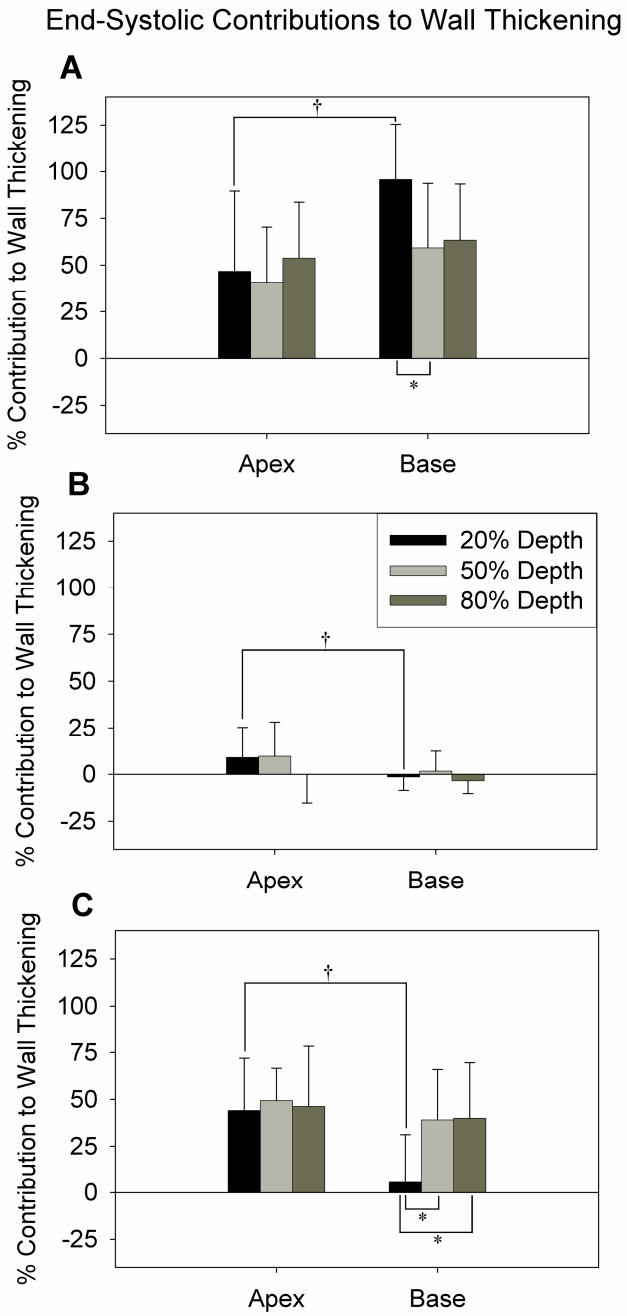

Figure 4.4: End-Systolic Contributions to Wall Thickening
Contributions to wall thickening (=radial strain) due to sheet extension (A), sheet thickening (B), and sheet shearing (C). Relative contributions of sheet deformation modes were similar at both sites. There were significant transmural gradients due to sheet extension and sheet shearing at the basal site (RMANOVA, $p<0.05$). * $p < 0.05$ vs. other depths. At the sub-epicardium only, the relative contributions to radial strain were significantly different between the apical and basal sites († $p < 0.05$ vs. same depth, by unpaired t-test).

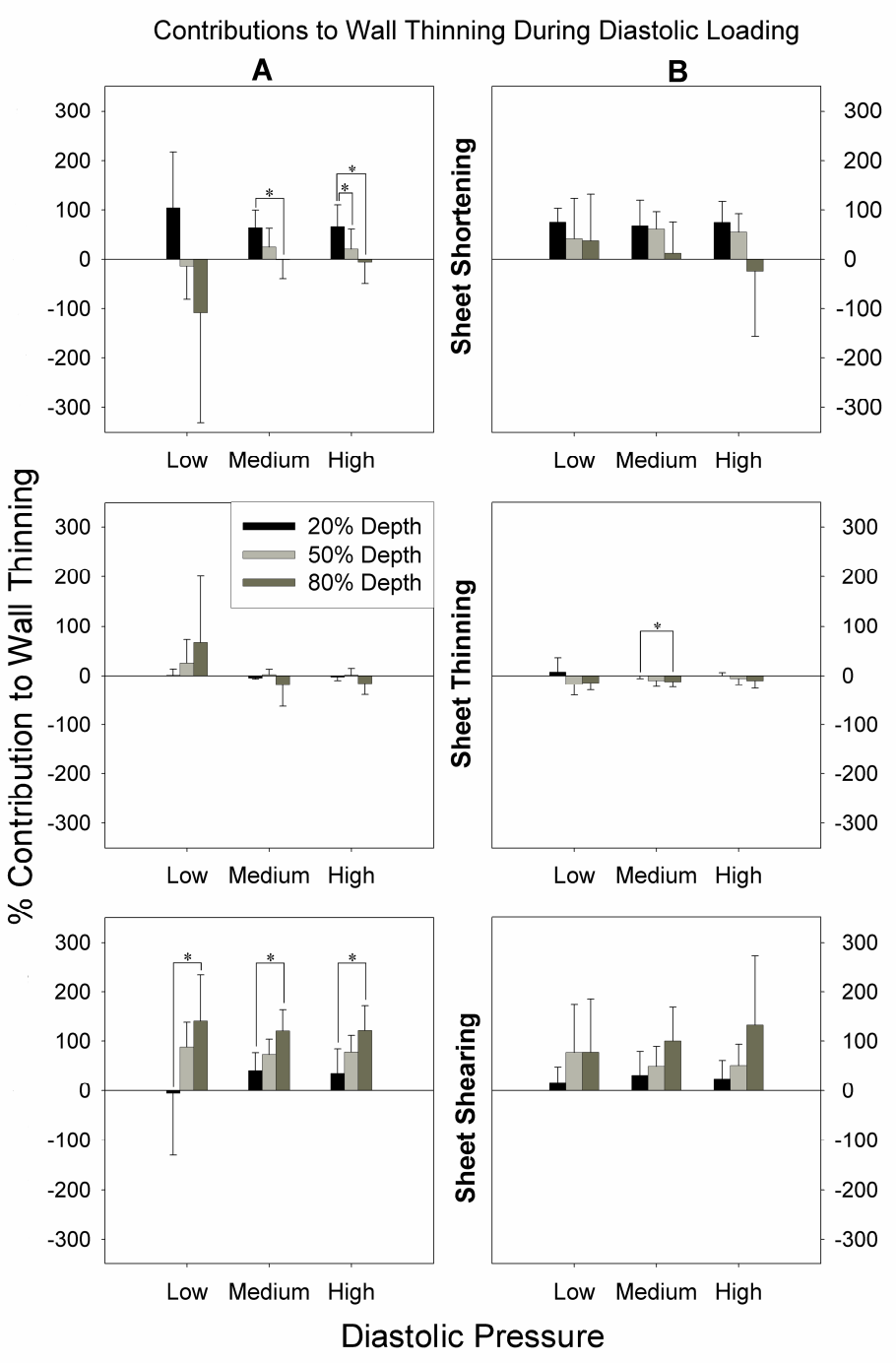

Figure 4.5: Contributions of Sheet Deformation to Wall Thinning During Diastolic Loading

Bars show relative contributions during diastolic inflation from a reference configuration of 3 mmHg to a deformed configuration of 8 mmHg ("Low"), 13 mmHg ("Medium"), or 18 mmHg ("High"). Contributions due to sheet shortening, thinning, and shearing were similar at apex (A) and base (B), and their transmural gradients were not significantly affected by diastolic load (* $p < 0.05$ vs. other depths).

Effect of Afterload on Contributions to Radial Strain

In the same subset of animals (group C), we examined the effect of load on the contributions during systolic wall thickening. Fig. 4.6 shows the changes in each component when peak systolic pressure was raised from 119 ± 22 to 169 ± 23 mmHg without significant change in end-diastolic pressure. Sub-epicardial values were excluded because the increased afterload reduced the magnitude of the strains; in some animals this magnitude became less than the uncertainty of the measurement. There were no significant differences in any of the components at the midwall or sub-endocardial levels at either the apex or base (two-way RMANOVA).

Effect of Activation Sequence on Contributions to Radial Strain

In a different subset of animals (Group D), we investigated the effect of activation sequence on the relative contributions to radial strain. Fig. 4.7 shows the time course of radial strain over a single cardiac cycle in a representative animal (depth = 50%), beginning at local depolarization. Stacked bars indicate contributions of sheet motion to overall radial strain (bar height = E_{33}). Fig. 4.7A shows an atrial paced beat with normal ventricular activation. Sheet thinning occurs during the isovolumic contraction, which acts to inhibit the normal, positive radial strain. During the ejection phase, all three components act together to increase radial strain (extension = 12%; thickening = 22%; shearing = 66% at peak wall thickening). Their relative contributions were fairly constant, with sheet thickening becoming somewhat more important approaching peak radial strain. The isovolumic relaxation phase varied much from animal to animal. In this example, it primarily consisted of sheet shearing. Fig. 4.7B and 4.7C depict the time

course of radial strain during local endocardial and epicardial pacing, respectively. Despite the differences in timing of peak radial strain, the contributions to radial strain was similar across pacing modes.

Fig. 4.8 shows the average value of each component during each of the three pacing modes. Only the time of peak radial strain is shown. There was a significant transmural gradient in all components, but not a significant effect of pacing or an interaction between pacing and depth according to a two-way RMANOVA.

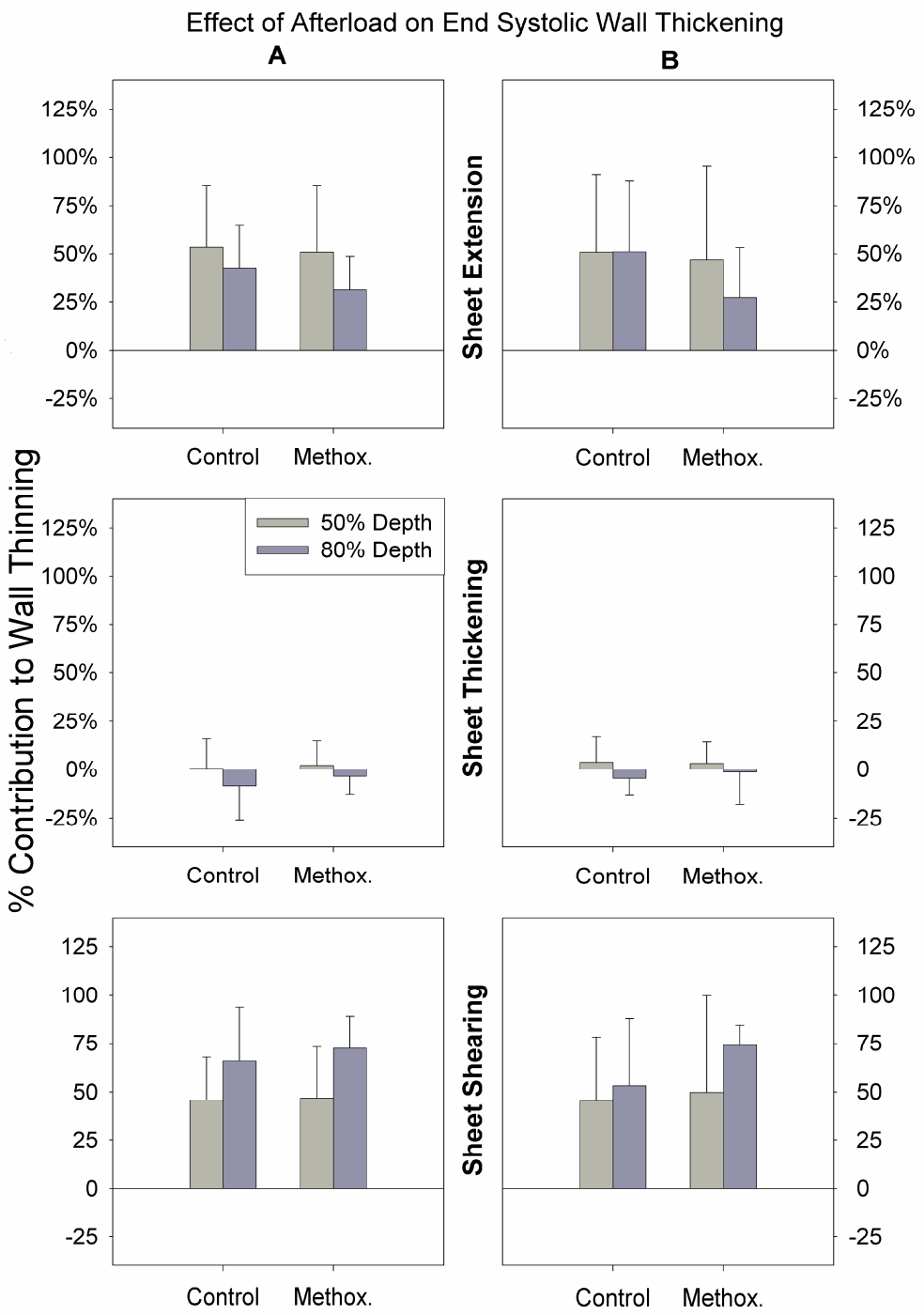

Figure 4.6: Effect of Afterload on Wall Thickening
Bars indicate relative contributions to wall thickening (=radial strain) at midwall and sub-endocardial depths. Increased afterload was achieved by administering methoxamine ("Methox."). There were no significant differences at the apex (A) or base (B) in any of the contributors. Sub-epicardial values were excluded due to insufficient strain magnitude to perform calculation.

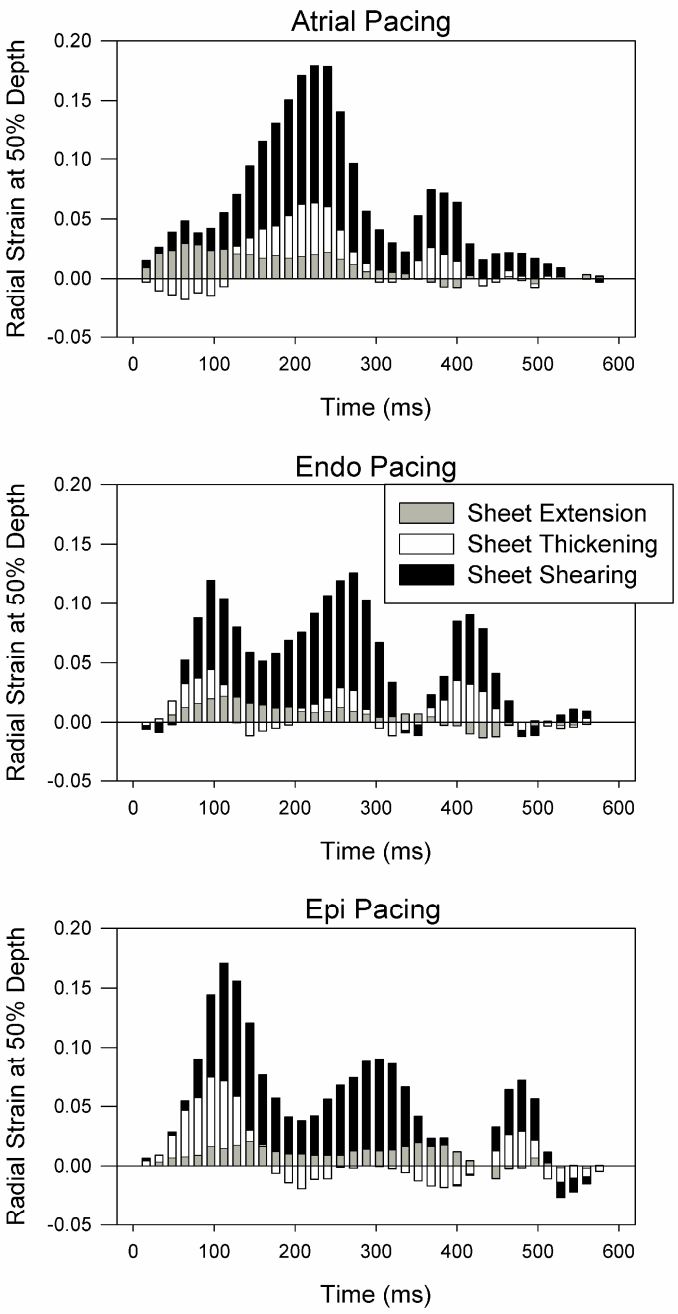

Figure 4.7: Time Course of Radial Strain
Time course of radial strain during atrial pacing (A), local endocardial pacing (B), or local epicardial pacing (C). Bar height indicates magnitude of radial strain at 50% depth as a function of time for one cardiac cycle, in a representative animal. Stacked bars distinguish the relative contributions of the different sheet motions. Though the time courses are different, the contributions of sheet deformation to radial strain are relatively constant throughout the cycle as well as with different pacing modes. Differences tended to be greatest during the isovolumic phases.

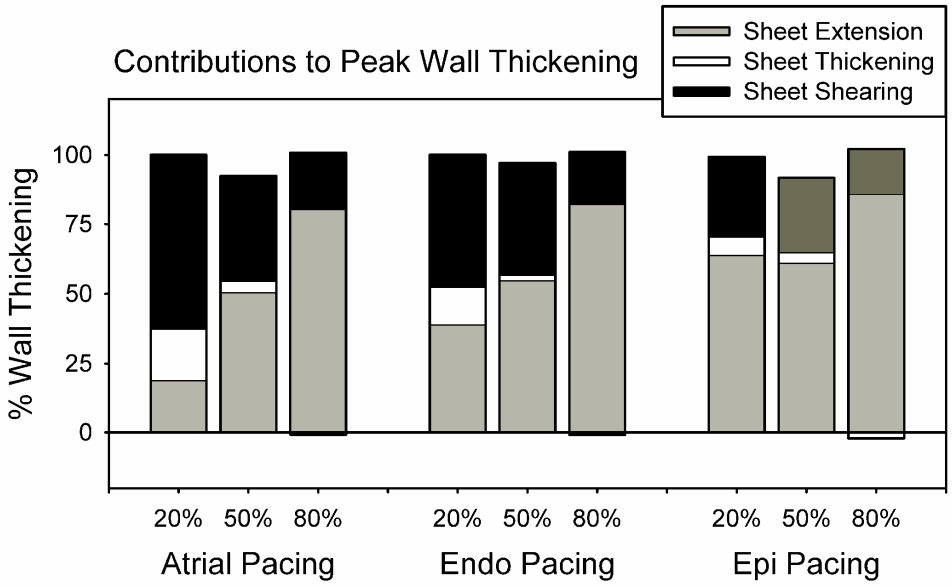

Figure 4.8: Average Contributions to Radial Strain During Pacing.
Stacked bars represent the average of each of the components of radial strain at three transmural depths. For all components, there was a significant transmural gradient; however, ventricular pacing (endocardial or epicardial) was not significantly different from atrial pacing, nor was there a significant interaction with depth (2-way RMANOVA).

4.5. Discussion

In this paper, we analyze the motion of myocardial sheets under a variety of circumstances, including passive inflation and active contraction with varying loads, as well as different ventricular activation sequences. The deformation measurements spanned the wall transmurally at apical and basal sites. The major findings of this study are that the mechanisms of wall thickening/thinning may be different in diastole than in systole at the apex, but are independent of load at either site. Additionally, despite significant differences in the sign of sheet angle at the apex and base, there were minimal differences in the relative contributions of the three sheet deformation modes to radial strain. Lastly, the sequence of activation did not alter the thickening mechanics when assessed at peak radial strain.

Definition of Wall Thickening

The term "wall thickening" is widely used but not clearly defined. Wall thickening is simply the change in measured wall thickness from diastole to systole, but such a measurement is not based on material points. Radial strain, on the other hand, is calculated based on the deformation of implanted markers that reflect material locations within the tissue. The measured deformation gradient at any point in the tissue can be expressed as $\mathbf{F} = \mathbf{RU}$, where R represents the rotation and U the right stretch tensor. This equation shows that total deformation is made up of both strain (contained in **U**) *and* rotation. Furthermore, our choice to use Lagrangian strain also means that we track deformation along the *initial* radial direction in the reference configuration, rather than

the current radial direction (deformed configuration). Therefore, radial strain may differ from what one thinks of as wall thickening.

To test the magnitude of the difference between wall thickening and radial strain, we devised a method to estimate wall thickening from the material markers. At each time t in the cardiac cycle, the current radial direction was calculated from the three epicardial beads in the transmural bead array. The vector from the epicardial centroid to the deepest bead was projected onto the radial vector, as shown in Figure 4.9. The length of this projection then represented the wall thickness at time t. Thickening over time was represented as a percentage. Next, a similar calculation was derived from the radial strain measurements. At increments of 1% depth through the wall, radial stretch was calculated and then summed across the wall according to Equation (4.2).

$$\Delta WT = \left(\frac{1}{101}\sum_{i=0\%}^{100\%}\lambda_i\right) - 1 \qquad \lambda_i = \sqrt{2 \cdot E_{33}^{i\%} + 1} \tag{4.2}$$

This summation gives the change in wall thickness as a percentage, based on the radial strain. We then compared the results obtained from each of the two methods, as shown in Figure 4.10. The analysis shows that the radial strain overestimates the wall thickening, but only by a small amount (~5%). Therefore, we feel that radial strain is a valid representation of wall thickening, despite the theoretical differences between the two measures.

Diastolic vs. Systolic Deformation of the Wall

For the first time we compared, quantitatively, the relative contributions of different sheet deformations to radial strain during diastole and systole. There were significant differences in sheet extension and shearing between diastole and systole at the

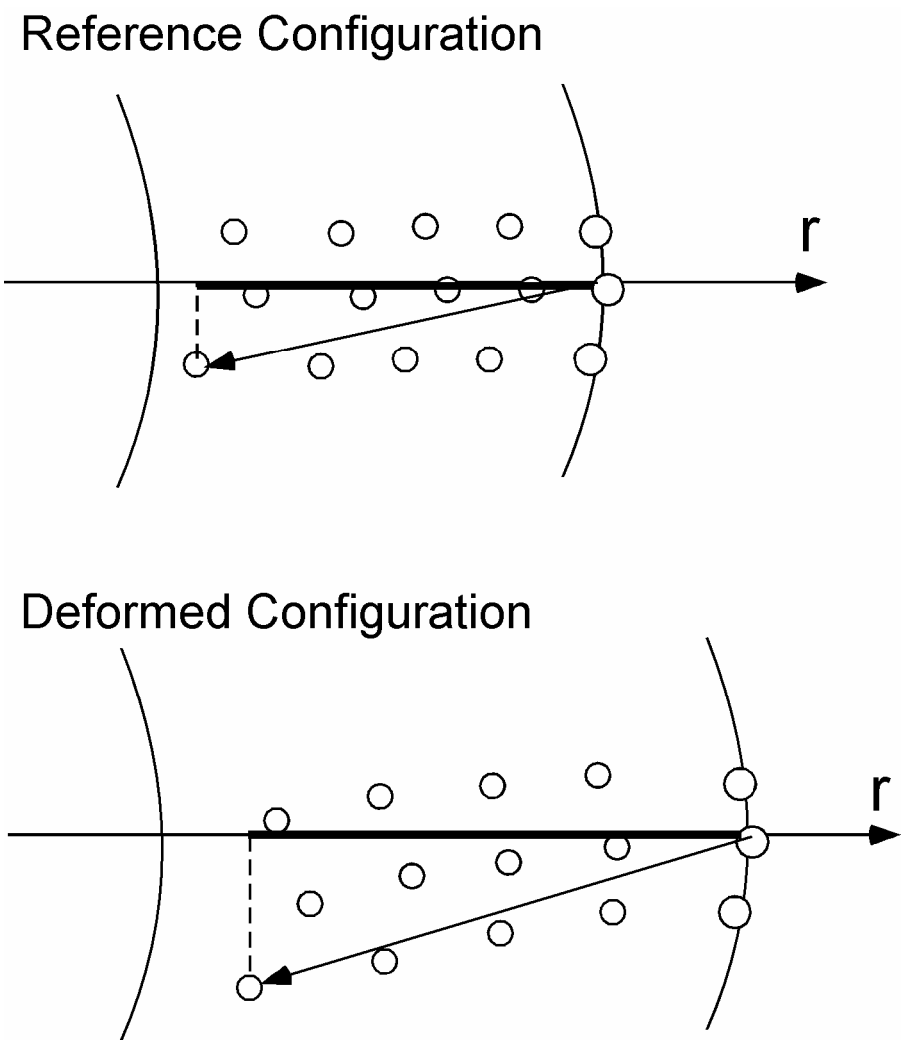

Figure 4.9: Estimation of Ventricular Wall Thickness
Schematic representation showing the configuration of a transmural bead array at two times during the cardiac cycle. To estimate the wall thickness, a vector was constructed from the epicardial centroid to the deepest marker and then projected onto the current radial vector (denoted by 'r'). Projections represent the estimate of wall thickness, and are indicated by a bold line in the illustration.

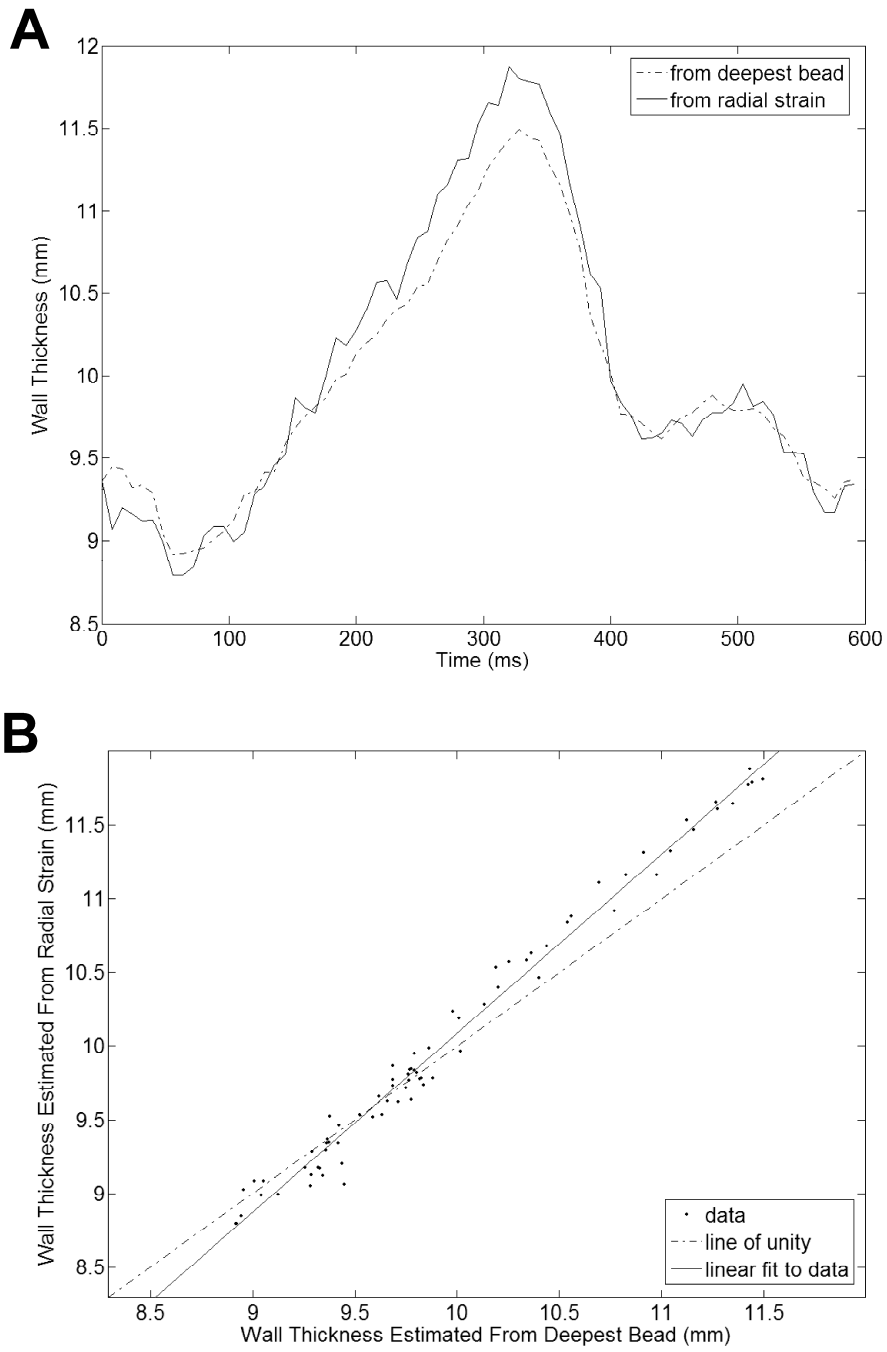

Figure 4.10: Comparison of Wall Thickening Estimated by Different Methods
A: Comparison of two estimates of wall thickening as a function of time throughout one cardiac cycle, in a representative animal. Time = 0 represents end diastole. The largest absolute difference occurs around end systole and is less than ½ of a millimeter.
B: Plot showing the correlation between the two techniques in the same animal. Dotted line represents a perfect correlation. Dashed line represents a linear fit to the data, which has slope greater than unity.

apical site, but not the basal site, when compared with a two-way RMANOVA. Takayama and co-workers (27) concluded that the contributions were qualitatively similar during diastole and systole. Our own quantitative analysis of the available raw data disagrees somewhat. We show a significant change at the apex, manifested as a shift from sheet shearing to extension. Nevertheless, sheet shearing remains the predominant mode of radial strain, consistent with the fundamental conclusions of Takayama (27) and Costa (7). In addition, a comparison of Figs. 4.4 and 4.5 seems to show larger transmural gradients during diastole than systole. However, a two-way RMANOVA with strain type (diastolic inflation to 18 mmHg vs. end-systolic) and depth found that there was no significant interaction of strain type on transmural gradient in any component. Therefore, this appears to be an artifact due to the difference in sample size between the two sets.

Choice of mean sheet angles

In this analysis, we chose to use the mean sheet angle for our calculations. This has previously been used when making histological measurements (1, 7, 13, 15) or using diffusion tensor MRI (DTMRI) (4, 5, 14). This is also the typical approach to quantifying the fiber angle, which varies linearly from epicardium to endocardium (26) and has a narrow dispersion (angular SD $< 20^{\circ}$) (16). However, the structural arrangement of the laminae is somewhat more complex. Our own unpublished observations indicate that there can be larger dispersions in the sheet angle, particularly nearing the endocardium. In addition, the sheet angle can have a bimodal distribution, again near the endocardium. This has been described in Hooks et al. (15), in which the authors observed a “dominant lamina population with interspersed small ‘pockets’ of

laminae approximately perpendicular to the principal alignment." The effects of both dispersion and bimodal populations on myocardial material properties is unknown, and may very well play an important role in the function of the myocardium, especially wall thickening. Thus, use of the average value of sheet angle may be inaccurate and therefore the results misleading. Further examination of the functional effects of the detailed laminar structure is ongoing in this laboratory.

Differences among species

In addition to dog, sheet angles have been measured in mice (20), rat (5), sheep (13), pig (30), and human (8). Mice have the most similar pattern of sheet angle to the dog, remaining approximately constant near –40º from epicardium to endocardium (20). Rat sheets are orientated more radially than dogs in the outer half; in the inner half, the orientation differed in sign, i.e. they are negative at the base and positive at the apex (5). Sheep sheets follow a notched pattern when examined in a lateral wall site; sheets are oriented positive at the epicardium, negative in the midwall, and positive again at the endocardium (13). Studies in pig and human do not provide data in a form suitable for direct comparison. Interestingly, however, Dou et al. show with DTMRI that the contributions to radial strain vary greatly based on circumferential location (8). Their anterior wall measurements are consistent with the data given here. It is not clear from their data whether or not these differences in contributions to radial strain are correlated with differences in sheet orientation.

Activation sequence

The transmural sequence of activation could also play a role in wall thickening. Myofibers are physically coupled between the endocardium and the epicardium, such that the deformation of one depends on the deformation of the other. This is a concept known as tissue tethering (3, 24). Because the epicardial and endocardial fiber angles are roughly perpendicular, endocardial fiber shortening will result in epicardial crossfiber shortening and vice-versa. In the normal sequence of activation (endo -> epi), the earlier activation of the endocardium causes epicardial deformation of the sheets that results in a unique profile of contributions to radial strain. When the activation sequence is reversed, the epicardium now deforms as a result of its own fiber shortening, and causes an endocardial deformation. This theory may have merit due to the early differences between endocardial and epicardial pacing (Fig. 4.7). However, the effect appears to be small, as the relative contributions at peak radial strain are not significantly different.

Limitations

There is a possibility that the insertion of beads into the myocardium causes significant damage, particularly in the short term. Due to surgical trauma and loss of the normal intra-thoracic pressure gradient, wall thickening is reduced in open-chest preparations. If the chest is closed and the animal is allowed to recover, the magnitude of radial strain increases while leaving the relative contributions to radial strain unchanged (6). This suggests that neither bead insertion injury nor the open-chest nature of the experiments has any qualitative effect on the results. DTMRI of a beating heart (8) is an

alternative method that can provide non-invasive measurements throughout the whole heart, but with limited resolution.

There are also limitations related to the histological assessment of sheet angle. The methods were somewhat different for the estimation of mean angle in groups A and B compared to groups C and D. In groups A and B, cleavage plane angles were measured in circumferential-radial and longitudinal-radial sections. The sheet angles were then reconstructed from the two views using a least squares fitting routine to provide a transmural distribution. For groups C and D, sheet angle was measured directly in a plane perpendicular to the local fiber direction. These measurements were performed from epicardium to endocardium at approximately 1mm intervals. The sheet angles used in the analysis were then interpolated at 20, 50, and 80% depth (linear interpolation using two nearest neighbors).

In conclusion, the myocardial wall deforms radially in a similar pattern with respect to the underlying sheet architecture regardless of whether it is thickening or thinning, at the apex or base, at different depths, different loads, or with different activation patterns. Myocardial sheets have a fixed behavior relative to wall motion that we were not able to change acutely. We do not rule out the possibility of chronic changes, which may provide a mechanism for wall thickening changes during disease states such as heart failure.

4.6. Acknowledgments

This work was supported by Medtronic Inc. and UC Discovery Grant ITL06-10159 and NIH-HL32583. The authors would like to thank Dr. James W. Covell for

valuable discussions and ideas concerning this manuscript. We would also like to thank Aundrea Graves, Katrina Go, Henry Tse, Leonard Lee, and Harn Chiu for technical and surgical assistance. Chapter 4, in part, has been accepted for publication as "Role of Myocardial Sheets in Ventricular Wall Mechanics" by Benjamin A. Coppola and Jeffrey H. Omens in *Molecular and Cellular Biomechanics*, 5.3: 183-196, 2008. The dissertation author was the primary investigator and author of this paper.

4.7. References

1. **Ashikaga H, Criscione JC, Omens JH, Covell JW, and Ingels NB, Jr.** Transmural left ventricular mechanics underlying torsional recoil during relaxation. *Am J Physiol Heart Circ Physiol* 286: H640-647, 2004.

2. **Ashikaga H, Omens JH, and Covell JW.** Time-dependent remodeling of transmural architecture underlying abnormal ventricular geometry in chronic volume overload heart failure. *Am J Physiol Heart Circ Physiol* 287: H1994-2002, 2004.

3. **Ashikaga H, Omens JH, Ingels NB, Jr., and Covell JW.** Transmural mechanics at left ventricular epicardial pacing site. *Am J Physiol Heart Circ Physiol* 286: H2401-2407, 2004.

4. **Chen J, Liu W, Zhang H, Lacy L, Yang X, Song S-K, Wickline SA, and Yu X.** Regional ventricular wall thickening reflects changes in cardiac fiber and sheet structure during contraction: quantification with diffusion tensor MRI. *Am J Physiol Heart Circ Physiol* 289: H1898-1907, 2005.

5. **Chen J, Song S-K, Liu W, McLean M, Allen JS, Tan J, Wickline SA, and Yu X.** Remodeling of cardiac fiber structure after infarction in rats quantified with diffusion tensor MRI. *Am J Physiol Heart Circ Physiol* 285: H946-954, 2003.

6. **Cheng A, Langer F, Rodriguez F, Criscione JC, Daughters GT, Miller DC, and Ingels NB, Jr.** Transmural sheet strains in the lateral wall of the ovine left ventricle. *Am J Physiol Heart Circ Physiol* 289: H1234-1241, 2005.

7. **Costa KD, Takayama Y, McCulloch AD, and Covell JW.** Laminar fiber architecture and three-dimensional systolic mechanics in canine ventricular myocardium. *Am J Physiol* 276: H595-607, 1999.

8. **Dou J, Reese TG, Tseng WI, and Wedeen VJ.** Cardiac diffusion MRI without motion effects. *Magnetic Resonance in Medicine* 48: 105-114, 2002.

9. **Dumesnil JG and Shoucri RM.** Quantitative relationships between left ventricular ejection and wall thickening and geometry. *J Appl Physiol* 70: 48-54, 1991.

10. **Gallagher K, Gerren R, Stirling M, Choy M, Dysko R, McManimon S, and Dunham W.** The distribution of functional impairment across the lateral border of acutely ischemic myocardium. *Circ Res* 58: 570-583, 1986.

11. **Gallagher KP, Osakada G, Matsuzaki M, Miller M, Kemper WS, and Ross J, Jr.** Nonuniformity of inner and outer systolic wall thickening in conscious dogs. *Am J Physiol Heart Circ Physiol* 249: H241-248, 1985.

12. **Gould KL, Kennedy JW, Frimer M, Pollack GH, and Dodge HT.** Analysis of wall dynamics and directional components of left ventricular contraction in man. *The American Journal of Cardiology* 38: 322-331, 1976.

13. **Harrington KB, Rodriguez F, Cheng A, Langer F, Ashikaga H, Daughters GT, Criscione JC, Ingels NB, and Miller DC.** Direct measurement of transmural laminar architecture in the anterolateral wall of the ovine left ventricle: new implications for wall thickening mechanics. *Am J Physiol Heart Circ Physiol* 288: H1324-1330, 2005.

14. **Helm PA, Younes L, Beg MF, Ennis DB, Leclercq C, Faris OP, McVeigh E, Kass D, Miller MI, and Winslow RL.** Evidence of structural remodeling in the dyssynchronous failing heart. *Circ Res* 98: 125-132, 2006.

15. **Hooks DA, Trew ML, Caldwell BJ, Sands GB, LeGrice IJ, and Smaill BH.** Laminar Arrangement of Ventricular Myocytes Influences Electrical Behavior of the Heart. *Circ Res* 101: e103-112, 2007.

16. **Karlon W, Covell J, McCulloch A, Hunter J, and Omens J.** Automated measurement of myofiber disarray in transgenic mice with ventricular expression of *ras*. *The Anatomical Record* 252: 612-625, 1998.

17. **Kindberg K, Karlsson M, Ingels J, N. B., and Criscione JC.** Nonhomogeneous Strain From Sparse Marker Arrays for Analysis of Transmural Myocardial Mechanics. *J Biomech Eng* 129: 603-610, 2007.

18. **LeGrice IJ, Takayama Y, and Covell JW.** Transverse shear along myocardial cleavage planes provides a mechanism for normal systolic wall thickening. *Circ Res* 77: 182-193, 1995.

19. **MacGowan GA, Shapiro EP, Azhari H, Siu CO, Hees PS, Hutchins GM, Weiss JL, and Rademakers FE.** Noninvasive Measurement of Shortening in the Fiber and Cross-Fiber Directions in the Normal Human Left Ventricle and in Idiopathic Dilated Cardiomyopathy. *Circulation* 96: 535-541, 1997.

20. **Omens JH, Usyk TP, Li Z, and McCulloch AD.** Muscle LIM protein deficiency leads to alterations in passive ventricular mechanics. *Am J Physiol Heart Circ Physiol* 282: H680-687, 2002.

21. **Perrone-Filardi P, Bacharach S, Dilsizian V, Maurea S, Frank J, and Bonow R.** Regional left ventricular wall thickening. Relation to regional uptake of

18fluorodeoxyglucose and 201Tl in patients with chronic coronary artery disease and left ventricular dysfunction. *Circulation* 86: 1125-1137, 1992.

22. **Rademakers F, Rogers W, Guier W, Hutchins G, Siu C, Weisfeldt M, Weiss J, and Shapiro E.** Relation of regional cross-fiber shortening to wall thickening in the intact heart. Three-dimensional strain analysis by NMR tagging. *Circulation* 89: 1174-1182, 1994.

23. **Sabbah HN, Marzilli M, and Stein PD.** The relative role of subendocardium and subepicardium in left ventricular mechanics. *Am J Physiol Heart Circ Physiol* 240: H920-926, 1981.

24. **Sengupta PP, Khandheria BK, Korinek J, Wang J, and Belohlavek M.** Biphasic tissue Doppler waveforms during isovolumic phases are associated with asynchronous deformation of subendocardial and subepicardial layers. *J Appl Physiol* 99: 1104-1111, 2005.

25. **Spotnitz HM, Spotnitz WD, Cottrell TS, Spiro D, and Sonnenblick EH.** Cellular basis for volume related wall thickness changes in the rat left ventricle. *J Mol Cell Cardiol* 6: 317-331, 1974.

26. **Streeter DD, Jr., Spotnitz HM, Patel DP, Ross J, Jr., and Sonnenblick EH.** Fiber Orientation in the Canine Left Ventricle during Diastole and Systole. *Circ Res* 24: 339-347, 1969.

27. **Takayama Y, Costa KD, and Covell JW.** Contribution of laminar myofiber architecture to load-dependent changes in mechanics of LV myocardium. *Am J Physiol Heart Circ Physiol* 282: H1510-1520, 2002.

28. **Waldman LK, Fung YC, and Covell JW.** Transmural myocardial deformation in the canine left ventricle. Normal in vivo three-dimensional finite strains. *Circ Res* 57: 152-163, 1985.

29. **Waldman LK, Nosan D, Villarreal F, and Covell JW.** Relation between transmural deformation and local myofiber direction in canine left ventricle. *Circ Res* 63: 550-562, 1988.

30. **Zimmerman SD, Criscione J, and Covell JW.** Remodeling in myocardium adjacent to an infarction in the pig left ventricle. *Am J Physiol Heart Circ Physiol* 287: H2697-2704, 2004.

5. A Microstructurally-Based Model of Active Myofiber Mechanics

5.1. Abstract

Contraction of cardiac myocytes provides the basis for ventricular pressure generation. The primary component of this contractile force acts along the axis of the myofilament; however, there may be a component directed radially as well. Biaxial testing of cardiac tissue has shown that cardiac muscle can generate as much as 50% of its fiber tension in the transverse direction. The structural basis for this is not clear. We hypothesized that transverse active stress is developed at the myofilament level, and transmitted through the myocardial laminar sheets (approximated as plane stress objects). To test this hypothesis, in one open-chest, anesthetized dog we implanted radiopaque markers into the left ventricle and imaged them with biplane cineradiography. After the functional data acquisition, the heart was fixed *in situ* at the end diastolic pressure of the study. Histological sectioning was used to determine the average fiber angle and distribution of sheet angles at every 1 mm depth through the wall in the region of the functional measurements. These measurements were incorporated into a finite element model which included a mathematical relationship representing active stress transmission through the myocardial sheets. Simulations were performed to determine strains in the measurement region at end systole, which were compared with the experimental results. The results indicate that the addition of a transverse active stress component improves the agreement between simulation and experiment, relative to a purely uniaxial simulation. Interestingly, the transmission of this transverse stress appears to be independent of the local sheet microstructure. We conclude that the myocardial sheets most likely do not

behave as plane stress objects. Despite the anisotropic structure of myocardium in the plane perpendicular to the myofibers, the ventricular wall appears to uniformly transmit stress within this transverse plane.

5.2. Introduction

It is well known that myofiber contraction creates force along the axis of a cardiac myocyte. Both the actin and myosin filaments are oriented along the myocyte axis, and it is their relative motion that leads to muscle shortening. The connections between the actin and myosin filaments (crossbridges) are most likely not oriented parallel to the myofilaments. This has not been experimentally verified, but a theoretical radial force component is expected when the crossbridge binding angle is non-zero (20, 26). The magnitude of this radial component depends on this binding angle, the filament spacing, and the sarcomere length. Lin and Yin (18) showed in an isolated tissue preparation that the myocardium generates significant transverse stresses (greater than 40% of those in the fiber direction). They concluded that fiber dispersion would be insufficient to generate forces of this magnitude, thus implicating an active mechanism of transverse tension generation. Finite element models of the heart have traditionally used uniaxial active stress models (8, 12). However, the discovery of transverse active tension has led to the development of models with improved agreement with experimentally-measured deformations (24).

The crossbridge binding angle provides a mechanism for radial force development at the level of the myofilament. There may be additional factors at other scales which also have an effect on myocardial stress development. For example, dispersion of

myofibers about the mean as measured by Karlon et al. would be one such mechanism (13). Another attractive tissue-scale mechanism is the myocardial laminae, or sheets. Myocardial sheets consist of layers of 4 –8 myocytes which are roughly stacked apex to base (16). A network of extracellular collagen fibers appears to provide tight coupling of myocytes within the sheet and looser coupling between adjacent sheets (2, 16). It has been suggested that a primary role of sheets may be to allow rearrangement of myofiber bundles by sliding along cleavage planes during the cardiac cycle (5, 17). These cleavage planes may have implications for active stress transmission as well. Because sheets are loosely coupled across cleavage planes, there may be less resistance to deformation between sheets than within. Based on this assumption, we might approximate an individual sheet as existing in a state of plane stress (7), unconstrained to thickening/thinning. Moreover, myocardial sheets are known to exhibit significant dispersion at the microscopic level, to a greater extent than fibers. Though not widely reported, this is evident in images of sheets in sheep (3) and pigs (11).

In order to test the hypothesis that myocardial sheets play a role in transverse stress development and that individual sheets behave as plane stress objects, we developed a biophysically-detailed model coupling active stress development at the cellular and tissue scales. This was integrated into a three-dimensional finite element model, and coupled to a 3-element Windkessel afterload model. The finite model includes detailed anatomical measurements of sheets from one dog. Simulation results were compared with experimentally-measured deformations from the same dog in order to determine the validity of the hypothesized sheet connections.

5.3. Methods

Animal Studies

Animal studies were performed according to the National Institutes of Health *Guide for the Care and Use of Laboratory Animals*. All protocols were approved by the Animal Subjects Committee of the University of California, San Diego, which is accredited by the American Association for Accreditation of Laboratory Animal Care.

The experimental protocol is described in detail in Chapter 2. In brief, three columns of radiopaque beads were inserted into the anterior wall of a canine heart and imaged with biplane cineradiography to determine the transmural deformation. Following the surgical procedure, the heart was fixed *in situ* with 2.5% gluteraldehyde and stored in 10% formalin. The heart was then sectioned for fiber and sheet angles as described in Chapter 2. However, rather than measuring only the mean sheet angle, several measurements were taken at each wall depth using the method or Karlon et al. (13). At each depth, approximately ten 8-10 μm sections were analyzed for a total of 500-700 measurements of the sheet angle, β, per depth. These angles were later incorporated into the biophysical model.

Computational Studies

Ventricular mechanics during active contraction where simulated with a non-linear finite element model. The chosen model includes realistic geometry, passive material properties, biophysically-based tension generation, realistic boundary conditions and an afterload model (15, 19, 23). It is a 120 node, 48 element, tri-cubic Hermite mesh of a dog heart (Fig 5.1) which is synchronously activated and contracts against a 3-

element Windkessel afterload model. This model has been used before (14) and will not be fully described here.

Myocardial stresses are determined at each integration point within the finite element mesh by a summation of passive stress (due to distension) and active stress (due to crossbridge cycling). The passive stress model described by Guccione et al. (9) is used as is. The active stresses are determined by the model described in the next section. The integration of these local stresses forms the basis of ventricular pressure generation in the model.

Active Stress Coupling model

At each integration point, the axial tension of a myocyte is calculated from the Guccione cellular model (8) as a function of several parameters, such as sarcomere length and activation history. This tension is then turned into a three-dimensional stress tensor by the active stress coupling model. This section describes the derivation of the coupling model.

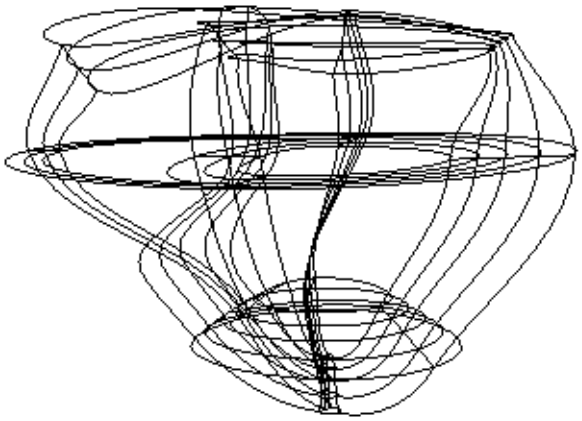

Figure 5.1: Wireframe Image of the Finite Element Mesh
The finite element mesh consists of 48 elements and represents both ventricles. The left ventricle is on the right side of the image. This mesh contains four elements in the transmural direction of the left ventricular wall, to provide adequate resolution of transmural deformation gradients. The region of interest is on the left ventricular wall near the equator.

1. Suppose the axial stress calculated from the cellular model output is T_{ff}. Further suppose that, due to some crossbridge binding angle, there is a radially-directed stress that is a fraction, k, of the axial stress. Therefore, the radial stress is equal to k times T_{ff}. This describes the stresses at the myocyte level.

2. Now suppose that this myocyte is part of a sheet. If we further assume that the sheet behaves as a plane stress element due to weak sheet-sheet coupling, then there can be no stress acting in the direction of the thickness of the sheet (sometimes referred to as the sheet-normal direction). Therefore, the active stress in a single sheet can be represented by:

$$\mathbf{T} = \begin{bmatrix} T_{ff} & 0 & 0 \\ 0 & k \cdot T_{ff} & 0 \\ 0 & 0 & 0 \end{bmatrix} \quad with\ respect\ to: \{\mathbf{e}_f, \mathbf{e}_s, \mathbf{e}_n\} \tag{5.1}$$

where $\mathbf{e}_f$ represents the fiber direction, $\mathbf{e}_s$ represents the within-sheet direction, and $\mathbf{e}_n$ represents the cross-sheet direction associated with this individual sheet.

3. Generally speaking, the myofibers which make up the sheet may have their axes oriented at some angle ϕ to the mean fiber direction (i.e. angle about the sheet-normal direction). This angle lies in the fiber-sheet plane (See figure 5.2). Taking into account this distribution, the stresses in this single sheet can be expressed in terms of an integral:

$$\mathbf{T}_{sheet} = \int_{-\pi/2}^{\pi/2} \mathbf{R}_{\phi} \cdot \mathbf{T} \cdot \mathbf{R}_{\phi}^{T} \cdot f(\phi) \cdot d\phi \tag{5.2}$$

$$\mathbf{R}_{\phi} = \begin{bmatrix} \cos(\phi) & \sin(\phi) & 0 \\ -\sin(\phi) & \cos(\phi) & 0 \\ 0 & 0 & 1 \end{bmatrix} \quad with\ respect\ to: \{\mathbf{e}_{f'}, \mathbf{e}_{s}, \mathbf{e}_{n}\}$$

where f(ϕ) represents the distribution of ϕ. $\mathbf{T}_{\text{sheet}}$ is still a plane stress object, but it is no longer a diagonal tensor in general. In other words, there may be a shear stress component due to the dispersion of ϕ within the sheet.

4. In the finite element formulation, stresses are integrated at the tissue scale. At this scale, there are many sheets. Each sheet has an orientation associated with it, which can be described as a function of two angles: β, which is the histologically measured sheet angle(5), and theta, which is the angle relative to the mean fiber direction (about the sheet direction). For an illustration of these angles, see figure 5.2. Now the stress at the tissue level can be integrated:

$$\mathbf{T}_{tissue} = \iint \mathbf{R}_{\theta} \mathbf{R}_{\beta} \mathbf{T}_{sheet} \mathbf{R}_{\beta}^{T} \mathbf{R}_{\theta}^{T} f(\theta) f(\beta) d\theta d\beta \tag{5.3}$$

$$\mathbf{R}_{\beta} = \begin{bmatrix} 1 & 0 & 0 \\ 0 & \sin(\beta) & \cos(\beta) \\ 0 & -\cos(\beta) & \sin(\beta) \end{bmatrix} \qquad \mathbf{R}_{\theta} = \begin{bmatrix} \cos(\theta) & 0 & \sin(\theta) \\ 0 & 1 & 0 \\ -\sin(\theta) & 0 & \cos(\theta) \end{bmatrix}$$

$$with\ respect\ to: \{\mathbf{e}_{f}, \mathbf{e}_{c}, \mathbf{e}_{r}\}$$

where $\mathbf{e}_{\text{f}}$ represents the fiber direction, $\mathbf{e}_{\text{r}}$ represents the radial direction, and $\mathbf{e}_{\text{c}}$ represents the crossfiber direction ($\mathbf{e}_{\text{c}} = \mathbf{e}_{\text{r}} \times \mathbf{e}_{\text{f}}$) associated with the bulk tissue;

f(θ) and f(β) represent the distributions of θ and β, respectively. Note that the different format of R_β is consistent with Costa's definition (5).

5. The angles ϕ, θ, and β change through time as the heart deforms. In other words, they are functions of Lagrangian strain (**E**), as shown by figure 5.10 in Appendix A. Because these quantities vary through time, the integration has to be performed at each time step of the finite element solver. This is computationally intensive, and yields an impractical problem to attempt to solve. In order to simplify the problem, the equations can be linearized using a first-order Taylor series expansion. For example, the sheet angle can be linearized as follows:

$$\mathrm{f}(\beta) \approx \mathrm{f}^*(\beta_0, \mathbf{E}) = \mathrm{f}(\beta_0, \mathbf{E}=0) + \left.\frac{df}{d\beta}\right|_{E=0} \delta\mathbf{E} \tag{5.4}$$

where f* represents the linearized function. More details are given in Appendix A. The resulting linearized equations now depend on ϕ_0, θ_0, and β_0, the distributions of angles in the reference configuration. Therefore, all integrations are dependent on geometric quantities in the reference configuration and can be pre-computed before attempting to solve the finite element problem.

6. Finally, Equation (5.3) can be expanded in terms of the distributions of the angles in the reference configuration. The equations for all six independent terms of the stress tensor look similar, and are of the following form:

$$\begin{aligned}
&\mathbf{T}_{tissue}(1,1) = Tff \cdot [g_0 + E_{ff} \cdot g_1 + E_{cc} \cdot g_2 + \ldots + E_{cr}^4 \cdot g_{114}] \\
&g_0 = \iiint h_0(k, \phi_0, \beta_0, \theta_0) d\phi_0 d\beta_0 d\theta_0 \\
&g_1 = \iiint h_1(k, \phi_0, \beta_0, \theta_0) d\phi_0 d\beta_0 d\theta_0 \\
&g_2 = \iiint h_2(k, \phi_0, \beta_0, \theta_0) d\phi_0 d\beta d\theta_0 \\
&g_{114} = \iiint h_{114}(k, \phi_0, \beta_0, \theta_0) d\phi_0 d\beta_0 d\theta_0
\end{aligned} \tag{5.5}$$

where g_0, g_1, …, g_{114} are pre-computable functions of the initial angle distributions, which are then multiplied by components of Lagrangian strain (less than or equal to Order($\mathbf{E}^4$). This reduces the theoretical maximum number of components from 115 to 61 (i.e. there are $6^4/4! = 54$ components of Order(E^4)). Since there are six independent components of stress, there could be as many as 115*6 = 690 different functions of the measured angle distributions in a given location.

Simplifying Assumptions

In addition to the assumptions inherent to the construction of the model, a few additional simplifying assumptions were made. Because we have no detailed measurements of the angles ϕ and θ, these angles were replaced with a normal distribution centered about the mean axes. This simplifies the resulting model due to the symmetry of these normal distributions. In addition, the effect of shear strain terms on the changes in the angular distribution was neglected. While these terms may in fact be significant, their behavior appears to be quite non-linear and the Taylor series expansion approach was not successful. This is a shortcoming of the model which might be addressed, for instance, with higher order Taylor series expansion or other linearization methods.

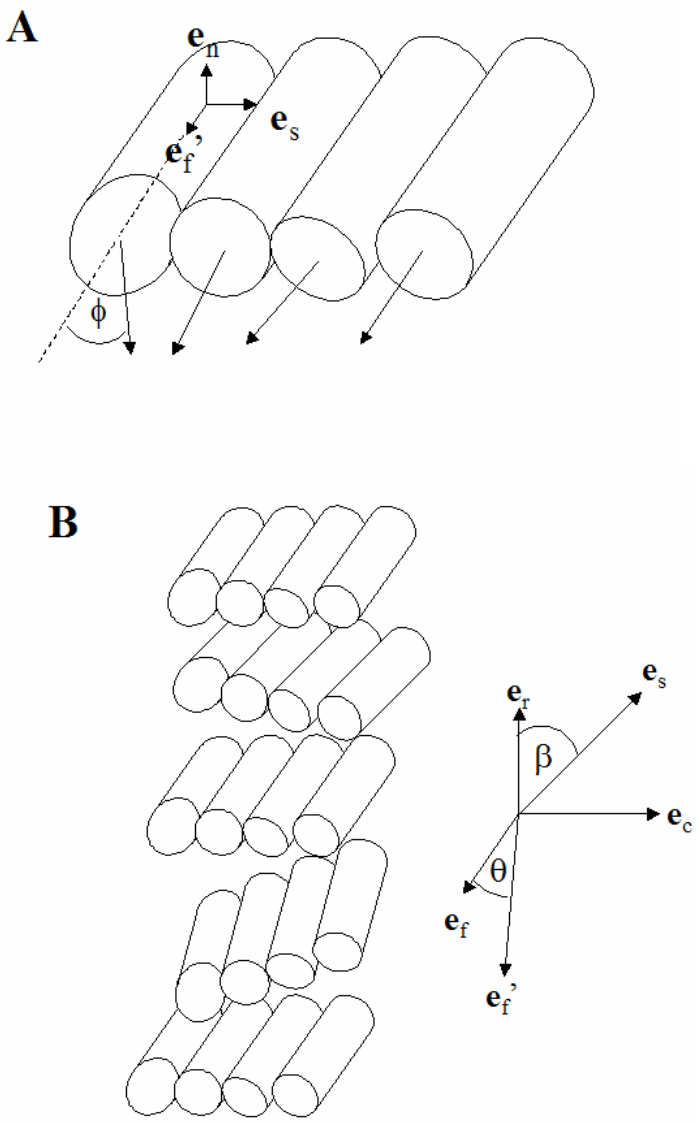

Figure 5.2: Description of Angles in Model
A: Schematic representation of a single sheet. $\mathbf{e}_f$' represents the sheet mean fiber axis, $\mathbf{e}_s$ represents the direction transverse to the fiber direction but within the sheet, and $\mathbf{e}_n$ represent the sheet normal direction (across the thickness of the sheet). ϕ represents the deviation in a single myocytes fiber axis relative to the mean fiber axis. ϕ is measured in the ($\mathbf{e}_f$', $\mathbf{e}_s$) plane.
B: Schematic representation of several sheets. $\mathbf{e}_f$ represents the tissue mean fiber axis, $\mathbf{e}_r$ represents the radial direction, and $\mathbf{e}_c$ is perpendicular to both ($\mathbf{e}_c = \mathbf{e}_r \times \mathbf{e}_f$). Each sheet has a sheet mean fiber axis at an the angle θ to the tissue mean fiber axis, in the ($\mathbf{e}_f$, $\mathbf{e}_r$) plane. Each sheet also has an angle β, which is in the ($\mathbf{e}_c$, $\mathbf{e}_r$) plane.

Implementation

The model was derived analytically with Python code utilizing a Swiginac library (Appendix B). The Swiginac library allows for MATLAB-style manipulation of linear algebra. The resulting code was then implemented into the laboratory's custom finite element modeling environment (Continuity 6.3, www.continuity.ucsd.edu). All simulations were run using 8 nodes of a computing cluster (granite.ucsd.edu). Computational time was approximately 1hr per simulation (end diastole to end systole).

The finite element mesh is 4 elements thick (5 nodes) at the location of the sheet measurements. These nodes were considered to be at 0, 25, 50, 75, and 100% depth through the wall. Sheet distributions from the nearest measurement location to each of these depths were used to compute the geometric parameters required as input to the active stress coupling model. Values at the integration points were found by linearly interpolating the nodal values.

Simulations

A total of 24 simulations were run. $f(\phi_0)$ and $f(\theta_0)$ were each represented by a standard deviation of either 0º or 12º about a mean angle of 0º. For $f(\beta_0)$, either the measured distributions or the mean angles were used. Values of 0, 0.3, or 0.5 were used for k. The results of these 24 simulations were compared to a previous implementation of a biaxial stress which did not include measured sheet orientations. This baseline model has active stress generated in the crossfiber and radial direction which is 30% of the stress along the fiber direction.

Table 5.1: Simulation Parameters

simulation	σ_ϕ	σ_θ	β	**k**
1	0º	0º	mean	0
2	0º	12º	mean	0
3	12º	0º	mean	0
4	12º	12º	mean	0
5	0º	0º	mean	0.3
6	0º	12º	mean	0.3
7	12º	0º	mean	0.3
8	12º	12º	mean	0.3
9	0º	0º	mean	0.5
10	0º	12º	mean	0.5
11	12º	0º	mean	0.5
12	12º	12º	mean	0.5
13	0º	0º	distribution	0
14	0º	12º	distribution	0
15	12º	0º	distribution	0
16	12º	12º	distribution	0
17	0º	0º	distribution	0.3
18	0º	12º	distribution	0.3
19	12º	0º	distribution	0.3
20	12º	12º	distribution	0.3
21	0º	0º	distribution	0.5
22	0º	12º	distribution	0.5
23	12º	0º	distribution	0.5
24	12º	12º	distribution	0.5

5.4. Results

Experiments

The end systolic strains are summarized at 25, 50, and 75% depth from the epicardium in Table 5.1. They correspond to an end-systolic pressure of 88 mmHg. The results are somewhat atypical. For instance, the transmural gradient of fiber shortening (E_{ff}) is usually much more uniform. The transmural gradient of radial thickening (E_{rr}) is typical but the magnitudes are uncharacteristically small. Table 5.2 provides a comparison to average data for 11 animals; these animals have been previously published in two separate groups by Ashikaga (1) and Coppola (4). Because the model geometry is not taken from the same animal as the sheet architecture measurements, it is important to intrepret the model results relative to both the specific animal as well as the general trends. This is especially important because several parameters of the finite element model are based on average data. Experiments in the laboratory are currently ongoing to try to create a more animal-specific model, where as many measurements are made from one animal as possible.

Automated measurements of sheet angle were performed on 5-10 μm sections at every 1 mm depth through the ventricular wall. These sections are cut perpendicular to the mean fiber direction so that the sheet angle β can be visualized directly. Figure 5.3 shows an example of one section, as well as the results of the automated processing scheme, which was performed as described by Karlon et al. (13). Results from the subendocardial and subepicardial regions are shown in figure 5.4. Note that there is

substantial dispersion about the mean sheet angle ($\sigma > 10^{o}$), particularly deeper in the wall. In addition, there is a second population of sheets deeper in the wall, oriented at approximately 90º to each other.

Table 5.2: End Systolic Strains
Strain at end-systole relative to end diastole, at three depths through the wall. % Depth is measured from the epicardium. Eff = fiber strain, Ecc = crossfiber strain, Err = radial strain, Efc = fiber-crossfiber shear, Ecr = crossfiber-radial shear, Efr = fiber-radial shear.

% Depth	25	50	75
E_{ff}	-0.025	-0.053	-0.092
E_{cc}	-0.02	-0.055	-0.095
E_{rr}	0.04	0.12	0.205
E_{fc}	0.016	0.011	0.012
E_{cr}	0.016	-0.01	-0.054
E_{fr}	0.029	0.044	0.053

Table 5.3: Average End Systolic Strains
Average strains at end systole relative to end diastole from a set of four animals. Data are mean ± SD. Abbreviations as in Table 5.1.

% Depth	25	50	75
E_{ff}	-0.093±0.037	-0.116±0.041	-0.118±0.050
E_{cc}	-0.0134±0.022	-0.061±0.027	-0.14±0.061
E_{rr}	0.109±0.050	0.206±0.049	0.317±0.079
E_{fc}	0.010±0.023	0.042±0.025	0.051±0.035
E_{cr}	0.036±0.031	0.033±0.036	0.000±0.062
E_{fr}	0.042±0.031	0.069±0.030	0.097±0.052

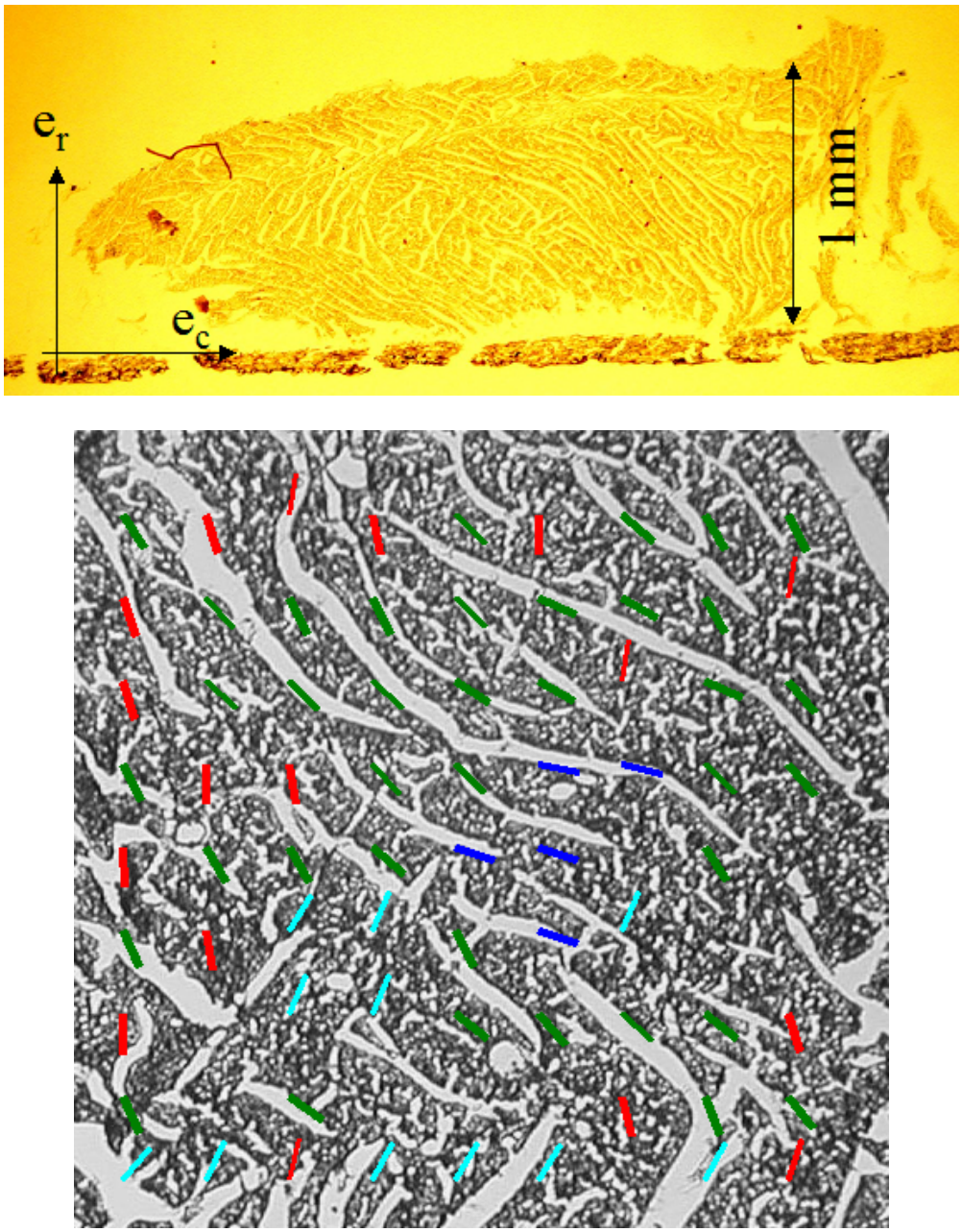

Figure 5.3: Automated Measurements of the Sheet Angle β
Top: 5 μm section of myocardium cut perpendicular to fiber angles. Gaps in tissue represent cleavage planes between myocardial sheets, which have opened up as tissue was allowed to desiccate for 10 mins. In this image, two distinct populations of sheets are present.
Bottom: Enlarged view of tissue section showing automated measurements of sheet angle. The region of interest for each measurement was 76 μm^2.

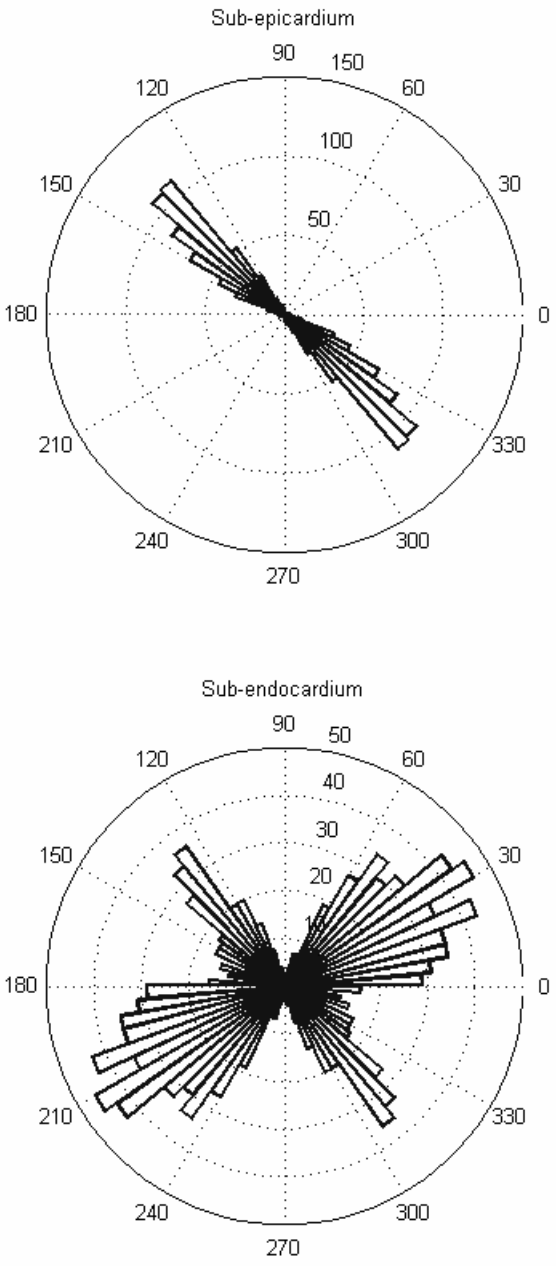

Figure 5.4: Experimental Distributions of the Sheet Angle β
Rose plots (circular histograms) showing the distribution of the sheet angle β in the sub-epicardium (top) and sub-endocardium (bottom). 0º/180º indicates that the sheet lie along the radial direction. It is clear that this animal has a second population of sheet angles in the sub-endocardium.

Model

The final form of the active stress coupling model has 76 pre-computable terms based on the three angular distributions $f(\phi_0)$, $f(\beta_0)$, $f(\theta_0)$, and k, the transverse active stress generated at the cellular level. All 24 simulations were run to an end systolic state with a left ventricular pressure of approximately 76 mmHg.

The uniaxial simulation (Simulation 1) had unanticipated behavior. It is compared with the baseline simulation (biaxial model) and with the experimental data in figures 5.5. It is also compared with the average experimental data in figure 5.6. In both comparisons the biaxial model is superior. The uniaxial model does poorly in the inner half, where the transverse shear (fiber-radial component) is large and negative. The biaxial model predicts this component to be close to zero, which agrees well with all of the experimental data. The uniaxial model has more of a transmural gradient in radial strain, but it is not smooth like the experimental data. The lines representing the simulation data in the figures are linear connections between the values at the 12 transmural integration points (4 elements times 3 integration points/element).

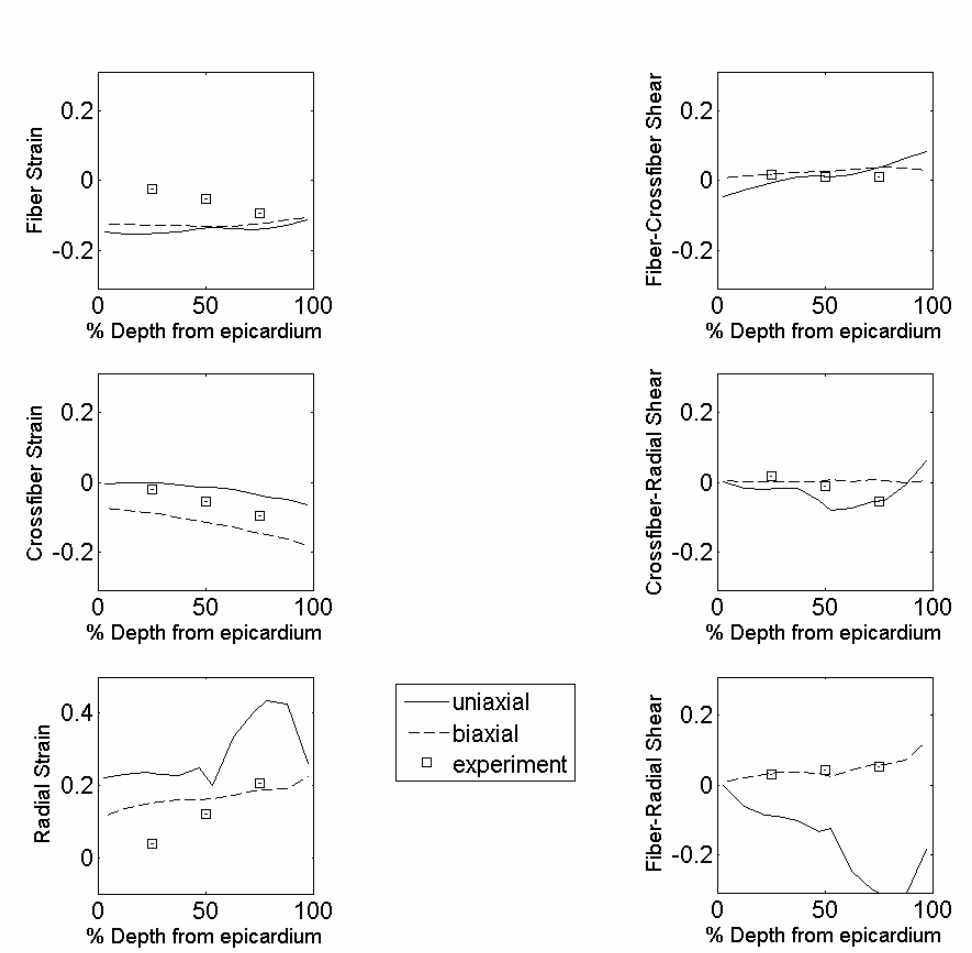

Figure 5.5: Uniaxial and Biaxial Simulations
Removing the transverse component of active stress had the effect of dramatically increasing radial strain on the inner half of the wall. This occurred along with a large negative fiber-radial shear, which was not seen experimentally.

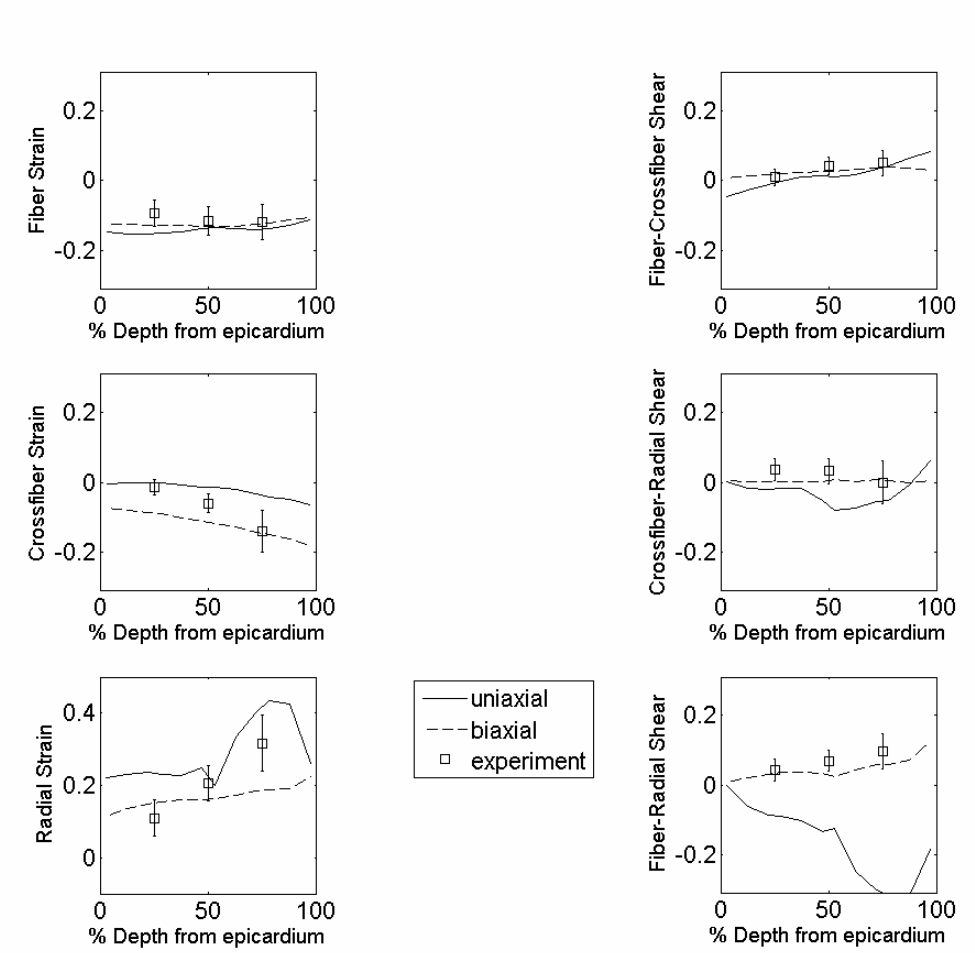

Figure 5.6: Uniaxial and Biaxial Simulations Compared With Average Data
Same as Figure 5.5 except experimental data now reflects the average of 11 animals (mean ± SD). Biaxial model reproduces experimental behavior better than uniaxial model, with significant deviation only in the radial strain component.

Next, we tested the effect of the parameter k, the fraction of fiber stress which is transmitted within the sheet. The results are shown in figure 5.7 for values of k = 0, 0.3, and 0.5, and again compared to the experimental strains (one animal only). The effect of k was most pronounced on the radial strain and the transverse shears (crossfiber-radial and fiber-radial). Small values of k led to unrealistic fiber-radial shear, while intermediate and large values of k led to unrealistic crossfiber-radial shear. Increasing k also decreased the radial strain (wall thickening) in the inner half.

Changes in the distributions of ϕ and θ had very little effect. Figure 5.8 shows that standard deviations of 12º in ϕ, θ, or both were negligible with k fixed at 0.3. Increasing the standard deviation of θ did have the effect of reducing radial strain, and a larger dispersion would likely have increased this effect. Due to the definition of ϕ as the fiber angle change within the sheet, it is unlikely that its standard deviation would be as large as 12º. Even if it was, there is little indication that would have much effect in this simulation.

Lastly, we examined the effect of representing the sheet distribution by its mean angle rather than its measured distribution. Figure 5.9 shows the results when transverse stress fraction k = 0.3. There are differences between the two simulations which are most pronounced in the sub-endocardium. Though neither model is particularly good in terms of radial strain or crossfiber-radial shear, the distribution model is closer to the experimental results.

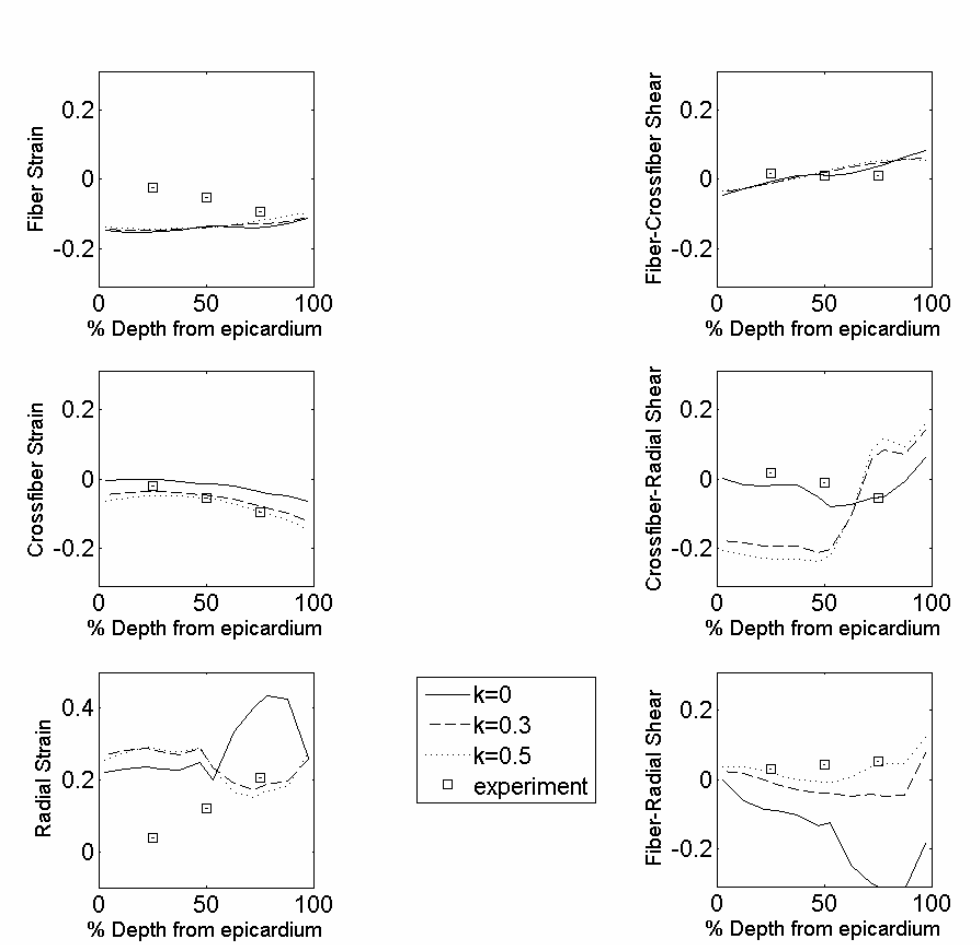

Figure 5.7: Effect of Transverse Stress Fraction k
In a model with no dispersion of ϕ or θ, and with a distribution of β, the transverse active stress parameter was varied from 0 to 0.5. This corresponds to simulation numbers 13,17, and 21.

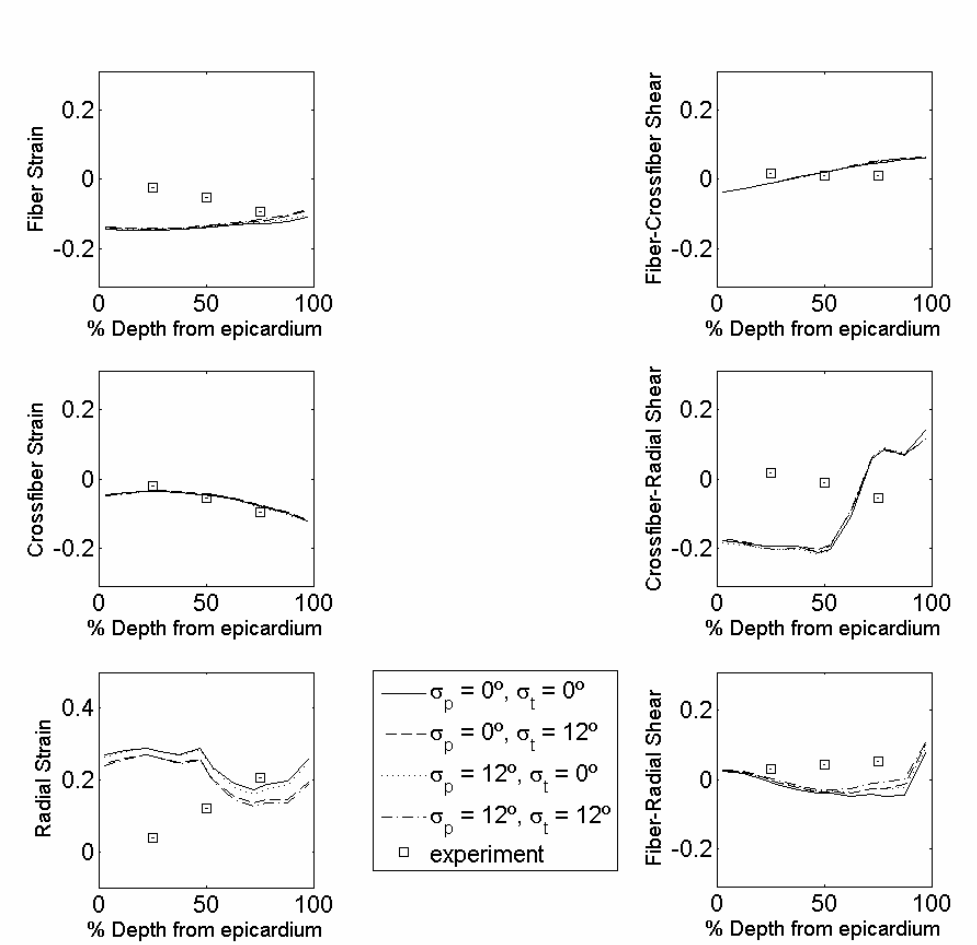

Figure 5.8: Effect of Variations in ϕ and θ
The individual and combined effects of including a normal distribution with standard deviation of 12º for ϕ and θ. All four simulations were performed with a transverse active stress fraction (k) of 0.3 (Simulation numbers 17-20).

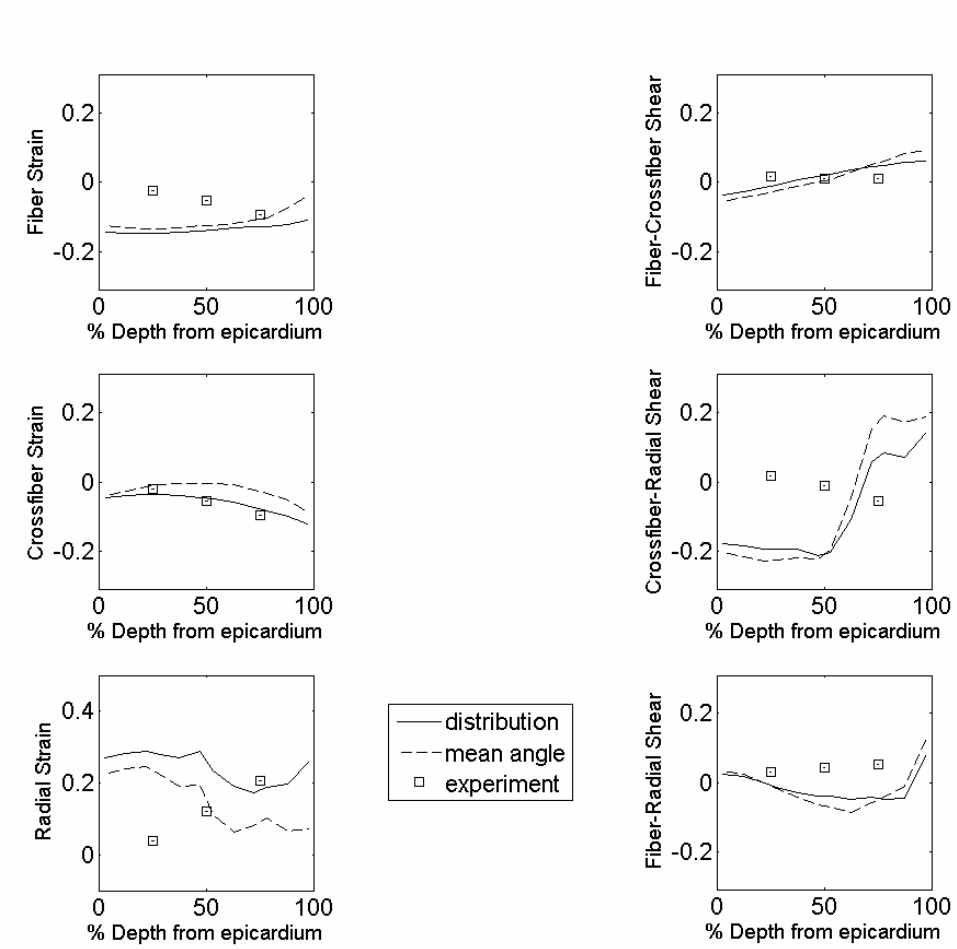

Figure 5.9: Effect of Sheet Angle Distribution Versus Mean Angle
The use of distributions of β rather than the mean angle (Simulations 5,17) had a small but appreciable effect on the strains, which was most notable in the radial strain component.

5.5. Discussion

In this study, we derive a mathematical relationship between active twitch force development at the sub-cellular scale and the resulting transverse force transmission at the tissue scale. The primary assumption behind this relationship is that force is transmitted within, but not between, myocardial sheets. The validity of this relationship is tested by making detailed histological measurements of sheet orientation and implementing the hypothesized sheet connections along with measured anatomic data into a finite element model. The simulated deformation of the finite element model is then compared to the measured experimental deformation. The results suggest that the hypothesis is incorrect, and therefore the mechanism for transverse force transmission differs from our assumption. Specifically, there is a significant component of force which is transmitted between adjacent sheets, reflecting a need for better understanding of the connections between sheets.

Using purely uniaxial force (force generated only along myofiber axis), the finite element simulations yielded physiologically inconsistent results –specifically, abnormally large fiber-radial shear strain. This result is in agreement with the findings of Lin and Yin, who observed biaxial active force generation in a slab of rabbit myocardial tissue (18). Despite this shortcoming of the uniaxial simulation, it predicted deformation that was closer to the experimental data than any of the simulations which included sheets; these simulations all predicted *less* radial strain on the endocardium than the epicardium. This is a surprising result considering that investigators have previously suggested that sheets may provide a mechanism for increased wall thickening(17, 22). In the current

implementation, sheets appear to have a much different effect, reducing wall thickening while increasing the effect of shearing across the wall.

Myocardial sheets have been shown to have unique passive material properties. For instance, they are stiffer within the plane of the sheet than across it (6). Despite this, it has been shown that simulations of systole are insensitive to changes in parameters controlling passive sheet properties (24). Nevertheless, it has been speculated that sheets might also affect the transmission of active stress transverse to the myofibers. Our results suggest that this may not be the case.

Of all the simulations, the baseline biaxial simulation appeared to have the most realistic behavior. In this simulation, active stress was transmitted in the crossfiber and radial directions, and is therefore independent of any sheet orientations. This finding clearly supports the notion of transverse force transmission both within and between myocardial sheets, suggesting that the coupling across sheets is more significant than it appears in confocal (25) or scanning electron microscope (SEM) sections (16). This could be due to a variety of reasons. First, there could be artifacts due to the preparation of the samples. The dehydration associated with this preparation is thought to exaggerate the size of the gaps between sheets. Secondly, dispersion of sheets may vary substantially regionally and transmurally, creating an interconnected web with no preferred direction of transverse force transmission. Further study using confocal imaging of extended volume might be able to clarify this.

There are several limitations to this modeling approach. First, the ventricular geometry used for the simulation was not measured in the same animal as the sheet orientations. Second, because sheet angles were not measured everywhere, one

transmural set of sheet angles had to be applied to the whole heart. There is known to be transventricular variation (5, 17), which likely influences the external load experienced by the tissue in the region of interest (left ventricular free wall). Third, the ventricle was synchronously activated, rather than having a realistic activation sequence. This could also affect tissue loading, although we predict this effect is small due to the near synchronous activation during normal sinus rhythm.

The results of the current study might be improved by obtaining geometry, strains, and microstructural anatomy all from the same animal, which is now possible using diffusion tensor magnetic resonance imaging (DTMRI). DTMRI can be used to determine the mean fiber and sheet orientation in the fixed heart with high resolution. They have been shown to correspond to the first and second eigenvectors of the diffusion tensor (21), and appear to be an effective way of determining the cardiac microstructure in areas of one sheet population (10). When two sheet populations exist, the diffusion tensor becomes transversely isotropic, and the sheet orientations are unknown (i.e. the second and third eigenvalues are of approximately equal value). The DTMRI data can then be registered to anatomic data also obtained with MRI. It may be worthwhile to repeat the simulations described here with a more realistic model to verify our results.

In conclusion, we constructed a mathematical relationship describing a proposed mechanism of force transmission transverse to myofibers that is dependent upon the locally measured sheet microstructure. A transverse component of active stress does appear to be important for normal wall function, however, the orientation of the sheet structure does not bound the direction of transverse force transmission. Interestingly, the ventricular wall appears to have a mechanism that allows it to behave in a relatively

uniform manner transverse to the myofiber direction in the active state, despite the sheet anisotropy in that plane.

5.6. Appendix A: Linearization

In continuum mechanics, deformations of bodies can create changes in angles. For example, consider the two-dimensional example in figure 5.10. Suppose the fibers in this tissue are originally oriented at an angle θ_0. At some time t, after undergoing deformation, this angle is represented by θ. The relationship between θ and θ_0 can be derived from continuum mechanics principles (7), and is given by:

$$\cos\theta = \frac{\lambda_1^2 \cos^2\theta_0 + 2E_{12}\cos\theta_0 \sin\theta_0}{\lambda_1\sqrt{\lambda_1^2\cos^2\theta_0 + \lambda_2^2\sin^2\theta_0}}; \quad \lambda_1^2 = 2E_{11}+1; \quad \lambda_2^2 = 2E_{22}+1 \tag{5.6}$$

For the purposes of the finite element method, this relationship is cumbersome. This is because the calculation of active stress requires the current angle θ, but we have only measured θ_0. Any calculations which depend on the integral of cos(θ) must then be performed at every time step of the finite element solution.

To avoid this, we can use a linearization strategy. By using a first-order Taylor series expansion, Equation (5.6) can be re-written as a product of linear functions. If we linearize about the point $E_{11} = E_{12} = E_{22} = 0$, the resulting equation is:

$$\cos\theta^* = \cos\theta_0 + \left.\frac{d(\cos\theta)}{dE_{11}}\right|_{\mathbf{E=0}} \cdot E11 + \left.\frac{d(\cos\theta)}{dE_{12}}\right|_{\mathbf{E=0}} \cdot E12 + \left.\frac{d(\cos\theta)}{dE_{22}}\right|_{\mathbf{E=0}} \cdot E22 \tag{5.7}$$

Substituting gives:

$$\cos\theta^* = \cos\theta_0 + (-\sin^2\theta_0 \cdot \cos\theta_0)\cdot(E_{22} - E_{11}) + (2\sin\theta_0)\cdot E_{12} \tag{5.8}$$

which can now be integrated to give:

$$\int \cos\theta^* d\theta = \int \cos\theta_0 d\theta_0 + (E_{22} - E_{11})\int(-\sin^2\theta_0 \cdot \cos\theta_0)d\theta_0 \cdot + E_{12}\int(2\sin\theta_0)d\theta_0 \tag{5.9}$$

Notice that the strain terms (E_{11}, E_{12}, E_{22}) are not functions of θ_0 and thus they can be moved outside of the integral. All of the remaining integrands are functions of θ_0, which remains constant throughout the simulation. Therefore, they can be pre-computed and multiplied by the appropriate values of strain at the current time step.

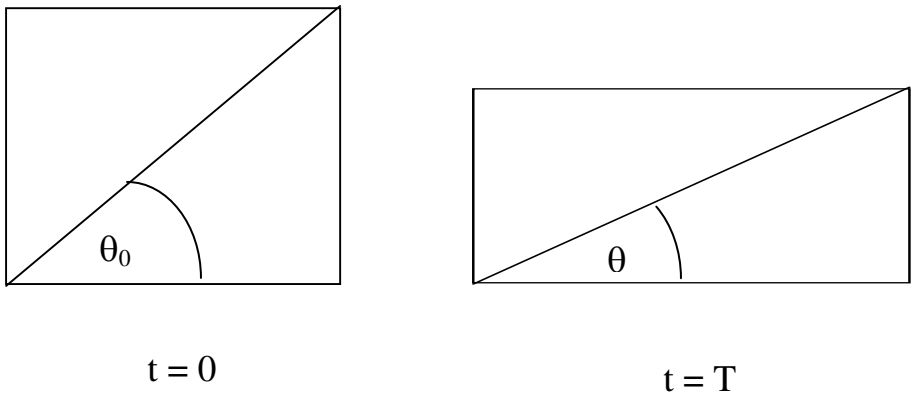

Figure 5.10: Wireframe Image of the Finite Element Mesh
Schematic diagram representing the change in angle θ as a body deforms from time t = 0 to t = T. As a result of horizontal lengthening and vertical shortening, $\theta < \theta_0$. The angle would also be affected by shearing deformation (not shown).

5.7. Appendix B: Python Code to Generate Active Stress Coupling Model

Main function

```
#import swiginac
from swiginac import symbol
from swiginac import transpose
from swiginac import matrix
from swiginac import subs
from swiginac import sqrt
from replace_functions import *


#p stands for phi, the angle within a sheet
#b stand for beta, the Costa-defined sheet direction
#t stands for theta, the angle in the remaining direction

#define some swiginac objects====================
cp = symbol('cp')
sp = symbol('sp')
cb = symbol('cb')
sb = symbol('sb')
ct = symbol('ct')
st = symbol('st')
c0 = symbol('c0')
s0 = symbol('s0')
k = symbol('k')
cp0 = symbol('cp0')
sp0 = symbol('sp0')
ct0 = symbol('ct0')
st0 = symbol('st0')
E11 = symbol('E11')
E22 = symbol('E22')
E12 = symbol('E12')
Efc = symbol('Efc')
Ecc = symbol('Ecc')
Eff = symbol('Eff')
Efr = symbol('Efr')
Ecr = symbol('Ecr')
Err = symbol('Err')
for i in range(6):
    for j in range(6):
        exec("cp%dsp%d = symbol('cp%dsp%d')")%(i,j,i,j)
```

```
for i in range(6):
   for j in range(6):
      exec("ct%dst%d = symbol('ct%dst%d')")%(i,j,i,j)

for i in range(20):
   for j in range(20):
      exec("c%ds%d = symbol('c%ds%d')")%(i,j,i,j)

list = ['Eff', 'Ecc', 'Err', 'Efc', 'Efr', 'Ecr']
strlist = []
#strlist = [0]* 1554
count = 0
#need to define the symbols before reading back into swiginac
for x in list:
   strlist.append("%s"%x)

for x in list:
   for y in list:
      exec("%s%s = symbol('%s%s')")%(x,y,x,y)
      strlist.append("%s%s"%(x,y))

for x in list:
   for y in list:
      for z in list:
         exec("%s%s%s = symbol('%s%s%s')")%(x,y,z,x,y,z)
         strlist.append("%s%s%s"%(x,y,z))

for x in list:
   for y in list:
      for z in list:
         for w in list:
            exec("%s%s%s%s = symbol('%s%s%s%s')")%(x,y,z,w,x,y,z,w)
            #strlist.append("%s%s%s%s"%(x,y,z,w))
# end defining symbols ==================================

Tfiber = matrix([[1, 0, 0],[ 0, k, 0], [0, 0, 0]])
rotation_matrix = matrix([[cp, sp, 0],[-sp, cp, 0],[0, 0, 1]])
Tlocal = rotation_matrix*Tfiber*rotation_matrix.transpose()
print Tlocal
Tsheet = Tlocal

Tsheet = Tsheet.subs(sp**2 == 1-cp**2)
Tsheet = Tsheet.subs(cp**2 == cp0**2 + 2*cp0**2*sp0**2*(E11-E22))
Tsheet = Tsheet.subs(sp==sp0 + (sp0*cp0**2)*(E22-E11) )
Tsheet = Tsheet.subs(cp == cp0 + (-sp0**2*cp0)*(E22-E11) )
```

```
#now substitute the correct strains for E11, E12, E22

#~ Tsheet = Tsheet.subs(E11== Eff)
#~ Tsheet = Tsheet.subs(E22 ==s0**2*Ecc + 2*s0*c0*Ecr + c0**2*Err)
#~ Tsheet = Tsheet.subs(E12==s0*Efc + c0*Efr)
Tsheet=Tsheet.expand()
print Tsheet

lines = [str(Tsheet[0,0]), str(Tsheet[0,1]), str(Tsheet[0,2]), str(Tsheet[1,1]),
str(Tsheet[1,2]), str(Tsheet[2,2])]
cnt = 0
for line in lines:
   line_out = ''
   line = line.replace('-', '+-1*')
   terms = line.split('+')
   for term in terms:
      new_term = MakeReplacements(term.strip(), 'cp0', 'sp0')
      newer_term = MakeSinReplacements(new_term.strip())
      #reassemble terms into a new string
      if term == terms[0]:
         line_out = newer_term
      else:
         line_out = line_out + '+' + newer_term
   if cnt == 0:
      Tsheet[0,0]  =  eval(line_out)
   elif cnt == 1:
      Tsheet[0,1] = eval(line_out)
   elif cnt == 2:
      Tsheet[0,2] = eval(line_out)
   elif cnt == 3:
      Tsheet[1,1] = eval(line_out)
   elif cnt == 4:
      Tsheet[1,2] = eval(line_out)
   elif cnt == 5:
      Tsheet[2,2] = eval(line_out)
   cnt = cnt + 1

#do the replacements for theta
Tsheet[1,0] = Tsheet[0,1]
Tsheet[2,0] = Tsheet[0,2]
Tsheet[2,1] = Tsheet[1,2]
Tsheet = Tsheet.expand()

Rt = matrix([[ct, 0, st],[ 0, 1, 0],[ -st, 0, ct]])
Rb = matrix([[1, 0, 0],[ 0, sb, cb],[ 0, -cb, sb]])
```

```
Tsheet = Rt*Rb*Tsheet*Rb.transpose()*Rt.transpose()
Tsheet[1,0] =0
Tsheet[2,0]=0
Tsheet[2,1] =0
#Tsheet = Rb*Tsheet*Rb.transpose()
print Tsheet

#peform the linearization of theta
Tsheet = Tsheet.expand()
Tsheet = Tsheet.subs(st**2 == 1-ct**2)
Tsheet = Tsheet.subs(ct**2 == ct0**2 + 2*ct0**2*st0**2*(E11-E22))
Tsheet = Tsheet.subs(st==st0 + (st0*ct0**2)*(E22-E11) )
Tsheet = Tsheet.subs(ct == ct0 + (-st0**2*ct0)*(E22-E11) )
Tsheet = Tsheet.subs(E11 == Eff)
Tsheet = Tsheet.subs(E22 == c0**2*Ecc-2*s0*c0*Ecr+s0**2*Err)
Tsheet = Tsheet.subs(E12 == -c0*Efc+s0*Efr)

Tsheet = Tsheet.expand()

lines = [str(Tsheet[0,0]), str(Tsheet[0,1]), str(Tsheet[0,2]), str(Tsheet[1,1]),
str(Tsheet[1,2]), str(Tsheet[2,2])]
cnt = 0
for line in lines:
    line_out = ''
    line = line.replace('-', '+-1*')
    terms = line.split('+')
    for term in terms:
        new_term = MakeReplacements(term.strip(), 'ct0', 'st0')
        newer_term = MakeSinReplacements(new_term.strip())
        #reassemble terms into a new string
        if term == terms[0]:
            line_out = newer_term
        else:
            line_out = line_out + '+' + newer_term
    if cnt == 0:
        Tsheet[0,0]  =  eval(line_out)
    elif cnt == 1:
        Tsheet[0,1] = eval(line_out)
    elif cnt == 2:
        Tsheet[0,2] = eval(line_out)
    elif cnt == 3:
        Tsheet[1,1] = eval(line_out)
    elif cnt == 4:
        Tsheet[1,2] = eval(line_out)
```

```
    elif cnt == 5:
        Tsheet[2,2] = eval(line_out)
    cnt = cnt + 1

Tsheet = Tsheet.expand()
Tsheet = Tsheet.subs(sb**2 == 1-cb**2)
Tsheet = Tsheet.subs(cb**2 == c0**2 + 2*c0**2*s0**2*(E11-E22) )
Tsheet = Tsheet.subs(sb==s0 + (s0*c0**2)*(E22-E11) )
Tsheet = Tsheet.subs(cb == c0 + (-s0**2*c0)*(E22-E11) )

Tsheet = Tsheet.subs(E11 ==s0**2*Ecc + 2*s0*c0*Ecr + c0**2*Err)
Tsheet = Tsheet.subs(E22 == c0**2*Ecc-2*s0*c0*Ecr+s0**2*Err)
Tsheet = Tsheet.subs(E12 == -s0*c0*Ecc + (s0**2-c0**2)*Ecr +s0*c0*Err)
Tsheet = Tsheet.expand()

#Tsheet = Tsheet.subs(sign_b**2 == 1)

cnt = 0
lines = [str(Tsheet[0,0]), str(Tsheet[0,1]), str(Tsheet[0,2]), str(Tsheet[1,1]),
str(Tsheet[1,2]), str(Tsheet[2,2])]
for line in lines:
    line_out = ''
    line = line.replace('-', '+-1*')
    terms = line.split('+')
    for term in terms:
        new_term = MakeReplacements(term.strip(), 'c0', 's0')
        #reassemble terms into a new string
        if term == terms[0]:
            line_out = new_term
        else:
            line_out = line_out + '+' + new_term
    if cnt == 0:
        Tsheet[0,0] = eval(line_out)
    elif cnt == 1:
        Tsheet[0,1] = eval(line_out)
    elif cnt == 2:
        Tsheet[0,2] = eval(line_out)
    elif cnt == 3:
        Tsheet[1,1] = eval(line_out)
    elif cnt == 4:
        Tsheet[1,2] = eval(line_out)
    elif cnt == 5:
        Tsheet[2,2] = eval(line_out)
    cnt = cnt + 1
```

```
Tsheet = Tsheet.expand()
#print Tsheet
f = open('Tsheet_070708_new.txt', 'w')
f.write(str(Tsheet[0,0]))
f.write('\n')
f.write(str(Tsheet[0,1]))
f.write('\n')
f.write(str(Tsheet[0,2]))
f.write('\n')
f.write(str(Tsheet[1,1]))
f.write('\n')
f.write(str(Tsheet[1,2]))
f.write('\n')
f.write(str(Tsheet[2,2]))
f.write('\n')
f.close()
#part 2

#a stands for alpha, t stands for theta
P1 = symbol('P1')
P2 = symbol('P2')
P3 = symbol('P3')
P4 = symbol('P4')
P5 = symbol('P5')
P6 = symbol('P6')
T1 = symbol('T1')
T2 = symbol('T2')
T3 = symbol('T3')
T4 = symbol('T4')
T5 = symbol('T5')
T6 = symbol('T6')
Tsheet = Tsheet.subs(cp1sp0 == P1) #=exp(-1/2.*vpr_p))
Tsheet = Tsheet.subs(ct1st0 == T1) #= exp(-1/2.*var_t))
Tsheet = Tsheet.subs(cp2sp0 == P2) #= 1/2.*(1+exp(-2*var_a)))
Tsheet = Tsheet.subs(ct2st0 == T2) #= 1/2.*(1+ exp(2*var_t)))
Tsheet = Tsheet.subs(cp2sp2 ==P3) #=1/8.*(1 - exp(-8*var_a)))
Tsheet = Tsheet.subs(ct2st2 == T3) #= 1/8.*(1 - exp(-8*var_t)))
Tsheet = Tsheet.subs(cp0sp2 == P4) #= 1/2.*(1 - exp(-2*var_a)))
Tsheet = Tsheet.subs(ct0st2 == T4) #= 1/2.*(1 - exp(-2*var_t)))
Tsheet = Tsheet.subs(cp1sp2 == P5) #= 1/4*(-1+exp(4*var_a))*exp(-9/2*var_a)
Tsheet = Tsheet.subs(ct1st2 == T5) #= 1/4*(-1+exp(4*var_t))*exp(-9/2*var_t)
Tsheet = Tsheet.subs(cp3sp2 == P6) # = -1/16*(1+exp(8*sigma^2)-
2*exp(12*sigma^2))*exp(-25/2*sigma^2)
Tsheet = Tsheet.subs(ct3st2 == T6) # = -1/16*(1+exp(8*sigma^2)-
2*exp(12*sigma^2))*exp(-25/2*sigma^2)
```

```
lines = [str(Tsheet[0,0]), str(Tsheet[0,1]), str(Tsheet[0,2]), str(Tsheet[1,1]), str(Tsheet[1,2]), str(Tsheet[2,2])]
cnt = 0
for line in lines:
    line_out = ''
    line = line.replace('-', '+-1*')
    terms = line.split('+')
    for term in terms:
        new_term = MakeELinear(term.strip())
        print new_term
        newer_term = MakeEReplacements(new_term.strip())
        print newer_term
        if term == terms[0]:
            line_out = newer_term
        else:
            line_out = line_out + '+' + newer_term
    if cnt == 0:
        Tsheet[0,0] = eval(line_out)
    elif cnt == 1:
        Tsheet[0,1] = eval(line_out)
    elif cnt == 2:
        Tsheet[0,2] = eval(line_out)
    elif cnt == 3:
        Tsheet[1,1] = eval(line_out)
    elif cnt == 4:
        Tsheet[1,2] = eval(line_out)
    elif cnt == 5:
        Tsheet[2,2] = eval(line_out)
    cnt = cnt + 1

#part 3

def reformat(el):
    replacements = [['Eff', 'E11'],['Ecc','E22'],['Err','E33'],['Efc','E12'],['Efr','E13'],['Ecr','E23']]
    for replacement in replacements:
        el = el.replace(replacement[0], replacement[1])
    if (len(el) == 3):
        el_out = el
    elif (len(el) == 6):
        el_out = el[0:3]+'*'+el[3:6]
    elif (len(el) == 9):
        el_out = el[0:3]+'*'+el[3:6] + '*' + el[6:9]
```

```
    elif (len(el) == 12):
        el_out = el[0:3]+'*'+el[3:6] + '*' + el[6:9] + '*' + el[9:12]
    else:
        print "Error in reformat"
        return None
    return el_out


T = [0,0,0,0,0,0]
T[0] = Tsheet[0,0]
T[1] = Tsheet[0,1]
T[2] = Tsheet[0,2]
T[3] = Tsheet[1,1]
T[4] = Tsheet[1,2]
T[5] = Tsheet[2,2]

Tout = open('Tsheet_part3_070708_new.txt','w')
CalcBeta = open('Constants.txt','w')
#strlist = [Eff,Ecc,Err,Efc,Ecr,Err]

swig_comp= symbol('swig_check')
component_list = ['active_stress(1,1)', 'active_stress(1,2)',
'active_stress(1,3)','active_stress(2,2)','active_stress(2,3)','active_stress(3,3)']
cnt = 1

for j in range(6):
    constant_term = str(T[j])
    for index in strlist:
        constant_term = constant_term.replace(index, '0')
    swig_constant_term = eval(constant_term)
    if (constant_term.find('k') != -1) :
        swig_constant_term = swig_constant_term.collect(k)
    CalcBeta.write("%s\n"%(str(swig_constant_term)))
    Tout.write("      %s = rPar_stress(%d) + \n"%(component_list[j],cnt))
    cnt = cnt+1
    #now do Eff, Ecc, etc.
    for el in strlist:
        T[j] = T[j].collect(eval(el))
        a = str(T[j])
        #a.rindex('Eff*')
        #~ try:
        if (a.rfind('%s*('%el) != -1):
        #a.rindex('%s*('%el)
        #comp = a[(a.rindex('%s*('%el)+len(el)+2):a.rindex(')')]
            comp = a[(a.rfind('%s*('%el)+len(el)+2):a.rfind(')')]
```

```
            swig_comp = eval(comp)
            swig_comp = swig_comp.collect(k)
            CalcBeta.write("%s\n"%(str(swig_comp)))
            el_out = reformat(el)
            Tout.write("     ' %s*rPar_stress(%d) + \n"%(el_out,cnt))
            cnt = cnt + 1
        T[j] = T[j].expand()
    Tout.write("\n")


Tout.close()
CalcBeta.close()
```

Auxiliary Functions

```
def operandFromPow(pow, name):
        if pow == 0:
            search = None
        elif pow == 1:
            search = name
        else:
            search = "%s^%d"%(name,pow)
        return search

def replaceBoth(operands, cospow, sinpow, cName, sName):
        if (cospow != 0) or (sinpow !=0):
            operands.append("%s%d%s%d"%(cName[:-1],cospow,sName[:-1],sinpow))
        cossearch = operandFromPow(cospow, cName)
        sinsearch = operandFromPow(sinpow, sName)
        if cossearch != None:
            del operands[operands.index(cossearch)]
        if sinsearch != None:
            del operands[operands.index(sinsearch)]

def getScore(chars):
    a = chars[0]
    b = chars[1]
    if (a == 'f' and b=='f'):
        score = 1
    if (a == 'c' and b=='c'):
        score = 2
    if (a == 'r' and b=='r'):
        score = 3
    if (a == 'f' and b=='c'):
```

```
        score = 4
    if (a == 'f' and b=='r'):
        score = 5
    if (a == 'c' and b=='r'):
        score = 6
    return score

def rearrangeLetters(letters, count):
    first_group = letters[1:3]
    first_group_sum = getScore(first_group)
    if count > 1:
        second_group = letters[4:6]
        second_group_sum = getScore(second_group)
        if (second_group_sum <= first_group_sum):
            tmp  = first_group
            tmp_score = first_group_sum
            first_group = second_group
            first_group_sum = second_group_sum
            second_group = tmp
            second_group_sum = tmp_score
    if count > 2:
        third_group = letters[7:9]
        third_group_sum = getScore(third_group)
        if (third_group_sum <= first_group_sum):
            tmp = first_group
            tmp_score = first_group_sum
            first_group = third_group
            first_group_sum = third_group_sum
            third_group = second_group
            third_group_sum = second_group_sum
            second_group_sum = tmp_score
            second_group = tmp
        elif (third_group_sum <= second_group_sum):
            tmp = second_group
            tmp_score = second_group_sum
            second_group = third_group
            second_group_sum = third_group_sum
            third_group = tmp
            third_group_sum = tmp_score
    if count > 3:
        fourth_group = letters[10:12]
        fourth_group_sum = getScore(fourth_group)
        if (fourth_group_sum <= first_group_sum):
            tmp = fourth_group
            fourth_group = third_group
```

```
            third_group = second_group
            second_group = first_group
            first_group = tmp
        elif (fourth_group_sum <= second_group_sum):
            tmp = fourth_group
            fourth_group = third_group
            third_group = second_group
            second_group = tmp
        elif (fourth_group_sum <= third_group_sum):
            tmp = fourth_group
            fourth_group = third_group
            third_group=tmp
    letters = "E" + str(first_group)
    if count > 1:
         letters = letters + "E" + str(second_group)
    if count > 2:
        letters = letters + "E" + str(third_group)
    if count > 3:
        letters = letters + "E" + str(fourth_group)
    return letters

def MakeELinear(term):
    #this is fiercely ghetto code
    term = term.replace("**","^")
    operands = term.split("*")
    for operand in operands:
        if (operand.count('E') >= 1):
            if (operand.count('^')==1):
                letters = get_operand_letters(operand)
                letters = letters[:-2]
                halves = operand.split('^')
                pow = int(halves[1])
                new_term = ''
                for i in range(pow):
                    new_term = new_term + ("%s*")%letters
                new_term = new_term[:-1]
                operands.append(new_term)
                del operands[operands.index("%s^%d"%(letters,pow))]
    for operand in operands:
        if (operand.count('E') >= 1):
            if (operand.count('^')==1):
                letters = get_operand_letters(operand)
                letters = letters[:-2]
                halves = operand.split('^')
                pow = int(halves[1])
```

```
            new_term = ''
            for i in range(pow):
               new_term = new_term + ("%s*")%letters
            new_term = new_term[:-1]
            operands.append(new_term)
            del operands[operands.index("%s^%d"%(letters,pow))]
   term = "*".join(operands)
   term = term.replace("^","**")
   return term

def replaceE(operands, letters, count):
      letters = rearrangeLetters(letters,count)
      operands.append("%s"%(letters))
      for i in range(count):
         a = str(letters[(i*3+1):(i*3+3)])
         #print operands.index("E%s")%a
         del operands[operands.index("E%s"%(a))]

def get_operand_pow(operand):
      #look for carrot
      #if carrot, read numbers after carrot
      pow = 1
      if (operand.count('^')==1):
         halves = operand.split('^')
         pow = int(halves[1])
      return pow

def get_operand_letters(operand):
   if (operand.count('E')==1):
      letters = operand
   return letters

def MakeReplacements(term, cName, sName):
   term = term.replace("**","^")
   operands = term.split("*")
   #print "operands:", operands

   cPow = 0
   sPow = 0
   for operand in operands:
    if cName in operand:
      cPow = get_operand_pow(operand)
    if sName in operand:
      sPow = get_operand_pow(operand)
```

```
    replaceBoth(operands, cPow, sPow, cName, sName)
    term = "*".join(operands)
    term = term.replace("^","**")
    return term

def MakeEReplacements(term):
    term = term.replace("**","^")
    operands = term.split("*")
    #now look for combinations of E's
    letters = ''
    count = 0
    for operand in operands:
        if 'E' in operand:
            letters += get_operand_letters(operand)
            count = count +1
    if (count > 0):
        replaceE(operands, letters, count)
    #look for "E", then look for exponent
    #drop all E^6 or higher???

    term = "*".join(operands)
    term = term.replace("^","**")
    return term

def MakeSinReplacements(term):
    term = term.replace("**","^")
    operands = term.split("*")
    for operand in operands:
        if "st1" in operand:
            term = "0"
            return term
        if "st3" in operand:
            term = "0"
            return term
        if "st5" in operand:
            term = "0"
            return term
        if "sp1" in operand:
            term = "0"
            return term
        if "sp3" in operand:
            term = "0"
            return term
        if "sp5" in operand:
            term = "0"
```

```
            return term
    #get rid of any odd sin terms in alpha and theta, such as c0s1 c1s1 c2s1 c3s1 c4s1 c0s3
c1s3 c2s3 c3s3 c4s3
    term = "*".join(operands)
    term = term.replace("^","**")
    return term
```

5.8. References

1. **Ashikaga H, Omens JH, Ingels NB, Jr., and Covell JW.** Transmural mechanics at left ventricular epicardial pacing site. *Am J Physiol Heart Circ Physiol* 286: H2401-2407, 2004.

2. **Caulfield JB and Borg TK.** The collagen network of the heart. *Lab Invest* 40: 364-372, 1979.

3. **Cheng A, Langer F, Rodriguez F, Criscione JC, Daughters GT, Miller DC, and Ingels NB, Jr.** Transmural sheet strains in the lateral wall of the ovine left ventricle. *Am J Physiol Heart Circ Physiol* 289: H1234-1241, 2005.

4. **Coppola BA, Covell JW, McCulloch AD, and Omens JH.** Asynchrony of ventricular activation affects magnitude and timing of fiber stretch in late-activated regions of the canine heart. *Am J Physiol Heart Circ Physiol*: 01225.02006, 2007.

5. **Costa KD, Takayama Y, McCulloch AD, and Covell JW.** Laminar fiber architecture and three-dimensional systolic mechanics in canine ventricular myocardium. *Am J Physiol* 276: H595-607, 1999.

6. **Dokos S, Smaill BH, Young AA, and LeGrice IJ.** Shear properties of passive ventricular myocardium. *Am J Physiol Heart Circ Physiol* 283: H2650-2659, 2002.

7. **Fung YC.** *A First Course In Continuum Mechanics*: Prentice Hall, 1993.

8. **Guccione JM and McCulloch AD.** Mechanics of Active Contraction in Cardiac Muscle: Part I---Constitutive Relations for Fiber Stress That Describe Deactivation. *J Biomech Eng* 115: 72-81, 1993.

9. **Guccione JM, McCulloch AD, and Waldman LK.** Passive material properties of intact ventricular myocardium determined from a cylindrical model. *J Biomech Eng* 113: 42-55, 1991.

10. **Helm PA, Tseng HJ, Younes L, McVeigh ER, and Winslow RL.** Ex vivo 3D diffusion tensor imaging and quantification of cardiac laminar structure. *Magn Reson Med* 54: 850-859, 2005.

11. **Hooks DA, Trew ML, Caldwell BJ, Sands GB, LeGrice IJ, and Smaill BH.** Laminar Arrangement of Ventricular Myocytes Influences Electrical Behavior of the Heart. *Circ Res* 101: e103-112, 2007.

12. **Hunter PJ, McCulloch AD, and ter Keurs HE.** Modelling the mechanical properties of cardiac muscle. *Prog Biophys Mol Biol* 69: 289-331, 1998.

13. **Karlon W, Covell J, McCulloch A, Hunter J, and Omens J.** Automated Measurement of Myofiber Disarray in Transgenic Mice With Ventricular Expression of ras. *The Anatomical Record* 252: 612-625, 1998.

14. **Kerckhoffs RC, Neal ML, Gu Q, Bassingthwaighte JB, Omens JH, and McCulloch AD.** Coupling of a 3D Finite Element Model of Cardiac Ventricular Mechanics to Lumped Systems Models of the Systemic and Pulmonic Circulation. *Ann Biomed Eng* 35: 1-18, 2007.

15. **Kerckhoffs RCP, Healy SN, Usyk TP, and McCulloch AD.** Computational Methods for Cardiac Electromechanics. *Proceedings of the IEEE* 94: 769-783, 2006.

16. **LeGrice IJ, Smaill BH, Chai LZ, Edgar SG, Gavin JB, and Hunter PJ.** Laminar structure of the heart: ventricular myocyte arrangement and connective tissue architecture in the dog. *Am J Physiol* 269: H571-582, 1995.

17. **LeGrice IJ, Takayama Y, and Covell JW.** Transverse shear along myocardial cleavage planes provides a mechanism for normal systolic wall thickening. *Circ Res* 77: 182-193, 1995.

18. **Lin DH and Yin FC.** A multiaxial constitutive law for mammalian left ventricular myocardium in steady-state barium contracture or tetanus. *J Biomech Eng* 120: 504-517, 1998.

19. **Nielsen PM, Le Grice IJ, Smaill BH, and Hunter PJ.** Mathematical model of geometry and fibrous structure of the heart. *Am J Physiol* 260: H1365-1378, 1991.

20. **Schoenberg M.** Geometrical factors influencing muscle force development. II. Radial forces. *Biophys J* 30: 69-77, 1980.

21. **Scollan D, Holmes A, Zhang J, and Winslow R.** Reconstruction of Cardiac Ventricular Geometry and Fiber Orientation Using Magnetic Resonance Imaging. *Annals of Biomedical Engineering* 28: 934-944, 2000.

22. **Takayama Y, Costa KD, and Covell JW.** Contribution of laminar myofiber architecture to load-dependent changes in mechanics of LV myocardium. *Am J Physiol Heart Circ Physiol* 282: H1510-1520, 2002.

23. **Usyk T, LeGrice I, and McCulloch A.** Computational model of three-dimensional cardiac electromechanics. *Computing and Visualization in Science* 4: 249-257, 2002.

24. **Usyk TP, Mazhari R, and McCulloch AD.** Effect of Laminar Orthotropic Myofiber Architecture on Regional Stress and Strain in the Canine Left Ventricle. *Journal of Elasticity* V61: 143-164, 2000.

25. **Young, Legrice, and Smaill.** Extended confocal microscopy of myocardial laminae and collagen network. *Journal of Microscopy* 192: 139-150, 1998.

26. **Zahalak GI.** Non-axial Muscle Stress and Stiffness. *Journal of Theoretical Biology* 182: 59-84, 1996.

6. Conclusions

The work presented in this dissertation was guided by two goals, the first dealing with the mechanics of asynchronous activation, especially in the late activated, "prestretched" region and the second with the role of the heart's fiber-sheet structure and its potential relationship to large myocardial wall thickening. In this chapter, conclusions from the work in each of these areas are briefly reviewed.

6.1. Asynchronous Activation

Asynchronous activation is characterized by shortening in the early activated regions concurrent with prestretch , or early lengthening, in the late activated regions. In late activated tissue the majority of prestretch was found to occur during isovolumic systole, after the time of electrical activation. The deformation was determined to be different from that which occurs during passive inflation. Both of these results suggest that the prestretch phenomenon is an active lengthening process which is at least in part mediated through direct tissue tethering between early and late activated regions. The deformation patterns also suggest that the transmural activation sequence in the late activated region is from the endocardium to the epicardium, regardless of the initial site of activation. This likely reflects the faster conduction in endocardial cells, or possibly Purkinje fibers, though the overall activation times did not support the latter explanation.

At short A-V delays, relative muscle fiber length in prestretched areas was unchanged compared to atrial activation, and fiber length in early activated areas was reduced. Although ejection shortening in late activated areas was increased compared to atrial activation likely due to a decrease in afterload, overall ejection shortening (as

reflected by stroke volume) was reduced due presumably to dyskinesis and to an overall reduction in initial muscle length in our preparation.

6.2. Laminar Architecture and Wall Thickening

The heart undergoes a paradoxically large change in thickness as it contracts, converting a 15% change in fiber length into a 40% or greater change in wall thickness. An incompressible cylinder model predicts cellular thickening of only 8%. This five-fold difference has brought attention to cleavage planes between myocardial laminar sheets, which are thought to offer little resistance to sliding due to the loose collagen tethers connecting adjacent sheets.

In the experimental studies of Chapter 4, we show that the myocardial wall deforms radially in a similar pattern with respect to the underlying sheet architecture regardless of whether it is thickening or thinning, at the apex or base, at different depths, different loads, or with different activation patterns. We also show this radial strain to be well correlated with myocardial wall thickening as it is thought of in the traditional sense, despite theoretical differences between the two quantities. Therefore, we conclude that myocardial sheets have a fixed behavior relative to wall motion that cannot be changed acutely.

In Chapter 5, we construct a mathematical relationship describing the transmission of force within, but not between, myocardial sheets. This relationship is dependent upon the locally measured fiber-sheet microstructure of the tissue. The results suggest that a transverse component of active stress is important for normal wall function. However, the orientation of the sheet structure does not bound the direction of this

transverse force, as was expected. is an insufficient explanation for this transverse force. Rather, closer agreement with experimental data was obtained when transverse force was transmitted both within and between myocardial sheets. In other words, the tissue appears to behave uniformly in directions transverse to the myofibers, despite its sheet anisotropy.

The consistency of the relative contributions of sheet deformation to radial strain does not imply a mechanistic understanding of the structure-function relationship. In Chapter 5 we attempt to elucidate the mechanism by which these sheets contribute to radial strain, by hypothesizing that sheets provide preferred planes for force transmission perpendicular to myofibers. In this computational analysis, distributions of sheet orientations were included in a finite element model, based on measurements in one transmural block of ventricular tissue. This approach also has limitations. First, the geometry of the finite element model was based on a different dog heart than the experimental data, and geometry is well known to have significant effects on cardiac mechanics. Second, detailed distributions of myocardial sheets were not measured throughout the heart. Though simulation results were only analyzed within the region of interest (defined by the location of the bead array in the animal experiment), there could be an effect of relative loading between different areas of the heart which depends on the specific anatomic structure.

In combination, the findings of chapters 4 and 5 suggest that myocardial sheets have a fixed behavior relative to the radial deformation of the wall, but the orientation of myocardial sheets (i.e. the angle β) is not the dominant feature determining active stress transmission perpendicular to myofibers. There may be other factors related to the

laminar architecture that differentiates the deformation patterns in different areas of the left ventricular wall. For example, the strength or concentration of collagen tethers between sheets may be more important to function than the orientation of the sheets themselves. Further work needs to be done in this area, for example to look for changes in the fiber-sheet structure of animals in heart failure.